



Recent developments in synthesis, properties, and applications of 2D Janus MoS_xSe_(1-x) and MoSe_xS_(1-x) alloys



Seetha Lakshmy ^a, Brinti Mondal ^b, Nandakumar Kalarikkal ^{a,c,d}, Chandra Sekhar Rout ^{e,f,*}, Brahmananda Chakraborty ^{g,h,**}

^a International and Inter-University Centre for Nanoscience and Nanotechnology, Mahatma Gandhi University, Kottayam, 686560, India

^b Department of Energy Science and Engineering, Indian Institute of Technology, Bombay, 400076, India

^c School of Pure and Applied Physics, Mahatma Gandhi University, Kottayam, 686560, India

^d School of Nanoscience and Nanotechnology, Mahatma Gandhi University, Kottayam, 686560, India

^e Centre for Nano and Material Sciences, Jain (Deemed-to-be University), Jain Global Campus, Kanakapura Road, Bangalore, 562112, India

^f Department of Chemical Engineering, Chungbuk National University, Cheongju, 28644, Republic of Korea

^g High Pressure and Synchrotron Radiation Physics Division, Bhabha Atomic Research Centre, Trombay, 400085, India

^h Homi Bhabha National Institute, Mumbai, 400094, India

ARTICLE INFO

Keywords:

MoS_xSe_(1-x)
2D material
TMDs
Janus structure
Alloying
Sensing
Optoelectronics

ABSTRACT

The Janus MoS_xSe_(1-x) and alloy MoS_xSe_(1-x), belonging to the family of two-dimensional (2D) transition metal dichalcogenides (TMDs), have gained significant attention for their potential applications in nanotechnology. The unique asymmetric structure of Janus MoS_xSe_(1-x) provides intriguing possibilities for tailored applications. The alloy MoS_xSe_(1-x) offers a tunable composition, allowing for the fine-tuning of the properties to meet specific requirements. These materials exhibit remarkable mechanical, electrical, and optical properties, including a tunable band gap, high absorption coefficient, and photoconductivity. The vibrational and magnetic properties also make it a promising candidate for nanoscale sensing and magnetic storage applications. Properties of these materials can be precisely controlled through different approaches such as size-dependent properties, phase engineering, doping, alloying, defect and vacancy engineering, intercalation, morphology, and heterojunction or hybridisation. Various synthesis methods for 2D Janus MoS_xSe_(1-x) and alloy MoS_xSe_(1-x) are discussed, including hydro/solvo-thermal, chemical vapour transport, chemical vapour deposition, physical vapour deposition, and other approaches. The review also presents the latest advancements in Janus and alloy MoS_xSe_(1-x)-based applications, such as chemical and gas sensors, surface-enhanced Raman spectroscopy, field emission, and energy storage. Moreover, the review highlights the challenges and future directions in the research of these materials, including the need for improved synthesis methods, understanding of their stability, and exploration of new applications. Despite the early stages of research, both the MoS_xSe_(1-x)-based materials have shown significant potential in various fields, and this review provides valuable insights for researchers and engineers interested in exploring its potential.

1. Introduction

Over the last few decades, two-dimensional (2D) materials have emerged as a vibrant research field in materials science and condensed matter physics. These materials, composed of a single or a few layers of atoms, exhibit unique electronic, optical, magnetic, and mechanical properties that differ markedly from their bulk counterparts. Among various 2D materials, transition metal dichalcogenides (TMDs) have gained tremendous research interest over the past years due to their

fascinating properties and several advantages such as tunable and direct bandgap, excellent spin transport, valleytronic and enhanced catalytic properties, etc. [1–4]. Further modification of physical and chemical properties of these TMDs (MX₂; M = Mo, W, V, etc. and X = S, Se, Te) materials family by different approaches such as doping, alloying, defect engineering, heterojunction, and size engineering, etc. have been investigated in recent years [5–8]. MoS₂ and MoSe₂ are the most studied TMDs among all the 2D materials due to their versatile properties, such as indirect to direct bandgap transition for its monolayer and ease of

* Corresponding author.

** Corresponding author. Centre for Nano and Material Sciences, Jain (Deemed-to-be University), Jain Global Campus, Kanakapura Road, Bangalore, 562112, India.

E-mail addresses: r.chandrasekhar@jainuniversity.ac.in (C.S. Rout), brahma@barc.gov.in (B. Chakraborty).

preparation. 2D MoS₂ consists of two layers of S atoms and a Mo sandwiched in between, whereas Se is replaced by S for MoSe₂. For MoS₂ and MoSe₂, the direct band gaps are reported to be 1.87 and 1.55 eV, respectively [9]. Considering the similarities in the atomic structures of these two TMDs, it is possible to tune their bandgap by controlling the sulfur and selenium composition. In this regard, two approaches are being employed for this purpose, which include: (i) alloying, by which MoS₂Se_{2(1-x)} is achieved, and (ii) replacing the "S" layer of one side with "Se" to achieve 2D MoSSe Janus crystals [Fig. 1]. The breakdown of the inversion symmetry of MoS₂ by these two approaches provides excellent opportunities for its applications in optoelectronic devices due to the tuneable bandgap [10].

The unique properties of MoSSe can be attributed to its unique crystal structure, which is similar to other 2D TMDs. It consists of a hexagonal lattice of transition metal atoms (Mo) sandwiched between two hexagonal layers of chalcogen atoms (S and Se), with weak van der Waals

forces holding the layers together. This layered structure gives rise to the possibility of exfoliating the material down to a single layer, making it an ideal candidate for use in electronic devices with high integration density [10].

The Janus type of 2D MoSSe crystals named after the two-faced Roman god is of significant scientific interest due to the broken crystal symmetry and large electronegativity difference across the unit cell [11, 12]. Unlike other conventional TMDs, the Janus MoSSe showcase inherent electrostatic dipole moment oriented perpendicular to its plane, and this stems from the disruption of the out-of-plane structural symmetry of MoS₂, resulting in a specific dipole orientation. This dipole moment significantly influences various properties and functionalities. This unique structure has drawn considerable attention in materials science due to its potential applications in various fields, including electronics, catalysis, energy storage, and biomedical engineering. One of the main advantages of the Janus structure is its ability to provide

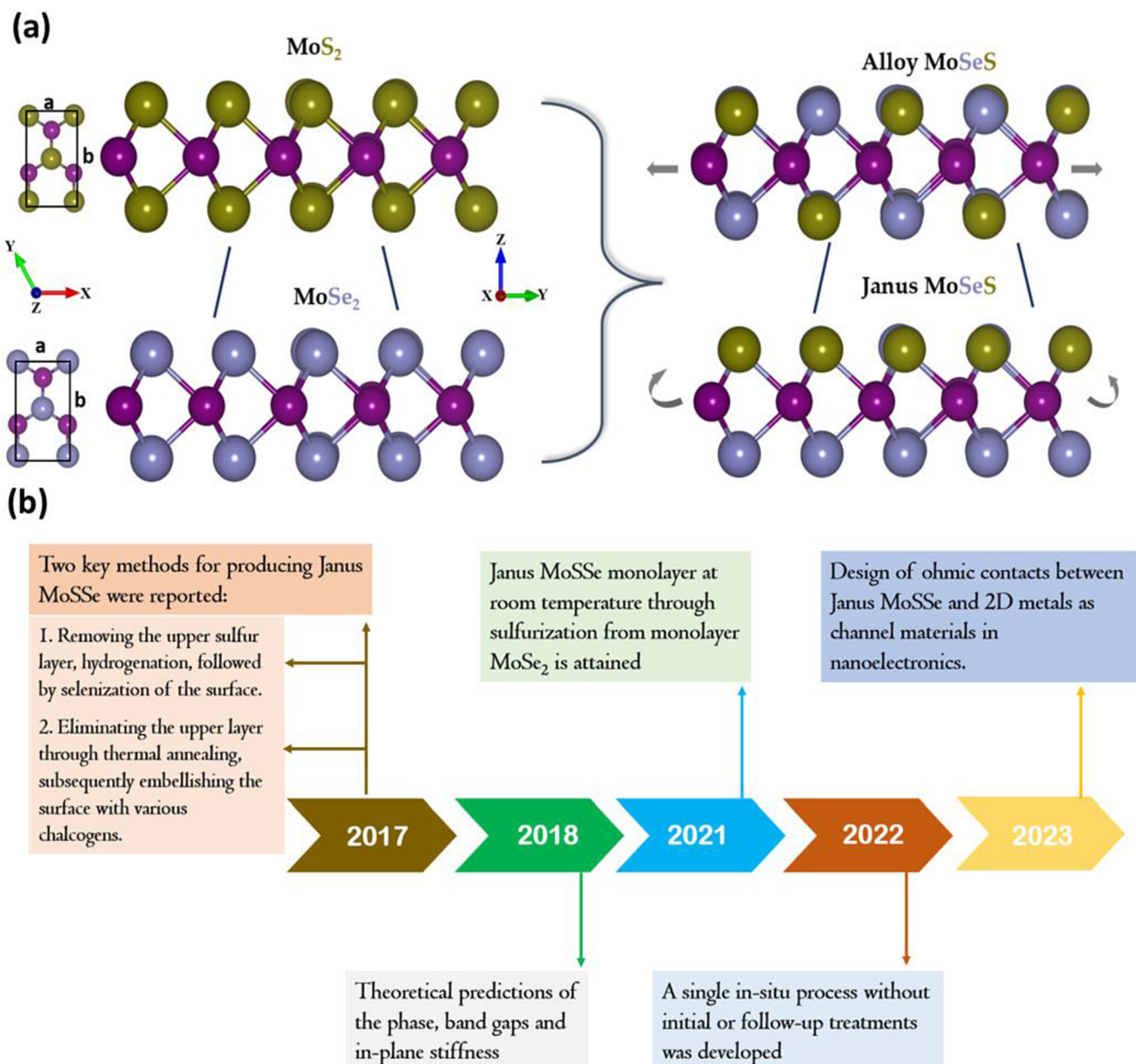


Fig. 1. (a) Schematic illustration of the side view of the crystal structure and arrangement of Mo and chalcogen atoms of alloy and Janus-type crystals of Molybdenum sulfo-selenides; (b) Timeline of 2D Janus MoSSe.

selective interactions between different surfaces or environments. For example, the two distinct faces of a Janus particle can interact differently with polar and nonpolar solvents, allowing for selective adsorption or separation of specific molecules. Similarly, these structures can create materials with different surface functionalities in catalysis, enabling selective reactions with specific substrates. These materials have shown promise in electronics for creating efficient transistors and sensors due to their unique electronic properties, such as bandgap engineering and carrier mobility. The Janus structure has also been explored for energy storage applications, where the distinct faces can be used to create asymmetric electrodes for improved charge storage and transport. 2D Janus MoSSe is reported to show high curie temperature (T_c) ferromagnetic order, skyrmion formation, giant Rashba splitting, unique excitonic properties, electric field-driven catalysis, and spintronic responses etc. [11,13–18].

Alloying is a promising approach for tuning the bandgap as well as the electrical and optical properties of MoS₂ [19]. As the composition of the S and Se changes, the electronic properties, especially the bandgap of the material MoSSe, can be significantly varied over a wide spectrum range [20]. For example, the bandgap can be tuned from 1.87 eV to 1.55 eV and electron mobilities from 0.1 to 0.4 cm²V⁻¹s⁻¹ by tuning the composition [21,22]. In addition to electronic properties, the S and Se composition changes can also alter the structural and optical properties of the material [23].

The purpose of this article is to provide a comprehensive overview of the unique properties, synthesis methods, and emerging applications of two closely related molybdenum sulfo-selenide materials: MoS₂Se_{2(1-x)} alloys and MoSSe Janus crystals, which to our knowledge has not been published till date. The importance of these materials and their enhanced applicability in versatile fields has made us take this decision, as it will be helpful for researchers in both academia and industries.

The first section of the article focuses on the preparation methods of the Janus MoSSe and MoS₂Se_{2(1-x)} alloys. Following this, we delve into the general properties of these materials, including the structural, electronic, optical, magnetic, vibrational properties, etc., examining their band structure, synthesis techniques, and a range of potential applications, including electrocatalysts, energy storage and conversion materials, sensors, photodetectors, field-effect transistors, and more. Finally, we discuss the future prospects and potential challenges associated with using these materials in device applications. By the end of this article, readers will gain a comprehensive understanding of the unique properties and potential applications of alloy MoS₂Se_{2(1-x)} and Janus MoSSe, as well as the potential challenges that may arise during the development of practical devices utilizing these materials.

2. Preparation methods

The synthesis of monolayer MoS_xSe_(1-x) alloys has been a subject of extensive exploration, with various methods demonstrated in previous studies. These methods include mechanical exfoliation of bulk material [24], gentle sputtering [25], physical vapour deposition (PVD) [25], and chemical vapour deposition (CVD) [26]. Among these techniques, CVD stands out as a promising avenue for the controlled synthesis of MoS_xSe_(1-x) flakes, particularly in the creation of monolayer structures. Wang et al. [27] recently discussed about CVD-grown TMDs onto suitable substrates for electrochemical applications is also addressed, emphasising methods to maintain crystal quality and interface compatibility.

Interestingly, while numerous methods have been investigated for the synthesis of monolayer MoS_xSe_(1-x) alloys, the methodology for synthesising for 2D Janus MoSSe has not been firmly established as of now. Within the literature, only the CVD method has been reported for the determination of 2D Janus TMDCs, highlighting the need for further exploration and development in this intriguing field.

2.1. Preparation of Janus MoSSe

A reproducible synthesis of monolayer Janus MoSSe flakes was first reported by Zhang et al. [18] through a controlled sulfurisation process applied to initially grown monolayer MoSe₂ flakes via the CVD method. MoSe₂ synthesis involved heating MoO₃ and Sulfur powder, resulting in flakes on a SiO₂/Si substrate. Sulfurisation of the top layer Se was achieved through a controlled substitutional reaction with vaporised S in a CVD setup. The sulfurisation process involved heating the monolayer MoSe₂ sample to 800 °C while vaporised S, released from heated S powder, reacted in a controlled substitutional manner for 30 min, forming Janus MoSSe. The atmospheric pressure maintained during the reaction enlarged the stable temperature window for top layer substitution, ensuring reproducibility. Sulfurisation time did not affect bottom layer Se substitution, highlighting the role of temperature and pressure in this selective process. The quality of the as-synthesised Janus MoSSe was verified using high-resolution transmission electron microscopy (HRTEM) and electron diffraction analyses, which revealed no lattice distortion, and the material maintained its 2H structure, as shown in Fig. 2. The XPS spectra of the Mo 3d, Se 3d, and S 2p core level peaks for the Janus SMoSe monolayer are also indicated in Fig. 2 [18].

An alternative method for the synthesis of Janus MoSSe involves utilizing plasma to eliminate the top atomic layer initially, followed by the process of selenization. A synthetic approach was employed by Lu et al. [12] to produce Janus MoSSe monolayers disrupting the out-of-plane structural symmetry. The procedure involves the fabrication of single-crystalline triangular MoS₂ monolayers on c-plane sapphire substrates using CVD. The top-layer S atoms are then removed and replaced with hydrogen atoms using a remote hydrogen plasma. Subsequent thermal selenization, without breaking the vacuum, enables Se to replace the H atoms, resulting in a structurally stable Janus MoSSe monolayer. This Janus structure features covalent bonds between the Mo atoms, underlying S, and top-layer Se atoms. Selenization temperature control is critical, with substrate temperatures between 350 °C and 450 °C ensuring Mo–Se bond formation without destabilising the 2D structure. At temperatures above 600 °C, randomised MoSSe alloy structures form. The key to the synthetic strategy for Janus MoSSe lies in controlling the reaction kinetics rather than relying on thermodynamics, preventing the disorderly mixing of Se and S and achieving the desired Janus structure. Fig. 3 (a) and (b) show the synthesis procedure and TEM image.

In the previously mentioned approaches, Janus MoSSe was synthesised by selectively replacing S or Se atoms on the surface of a MoS₂ or MoSe₂ layer with Se or S atoms. These methods, however, involve additional post-treatments following the initial CVD of 2D MoS₂ or MoSe₂ TMDs, leading to increased complexity and cost. To address these challenges, Jang et al. [28] introduced a novel approach, streamlining the process by employing a single NaCl-assisted step in a CVD apparatus. This method employs a three-step *in situ* process to activate Mo and S sequentially for the growth of MoS₂, create S vacancies in the top MoS₂ layer, and activate Se to fill the vacancies by adjusting the temperature (T) without the need for additional means like H₂ plasma. In the CVD apparatus shown in Fig. 4 a, Janus MoSSe is grown in a two-zone system: low-T (zone 1) and high-T (zone 2). Se and S powders are placed in one boat in zone 1, while MoO₃ + NaCl powder and a SiO₂/Si substrate are placed in the other boat in zone 2. In the first step, a MoS₂ flake is synthesised on the substrate, activating Mo and S at 750 °C and 150 °C, respectively. In the second step, S vacancies are created in the MoS₂ flake at 580 °C for 10 min. The third step involves filling these vacancies with Se atoms activated at 300 °C, resulting in the formation of Janus MoSSe. Fig. 4 b illustrates the growth mechanism. The growth conditions for Janus MoSSe layers were fine-tuned by adjusting key deposition parameters like the distance between the boats and the Ar flow rate which

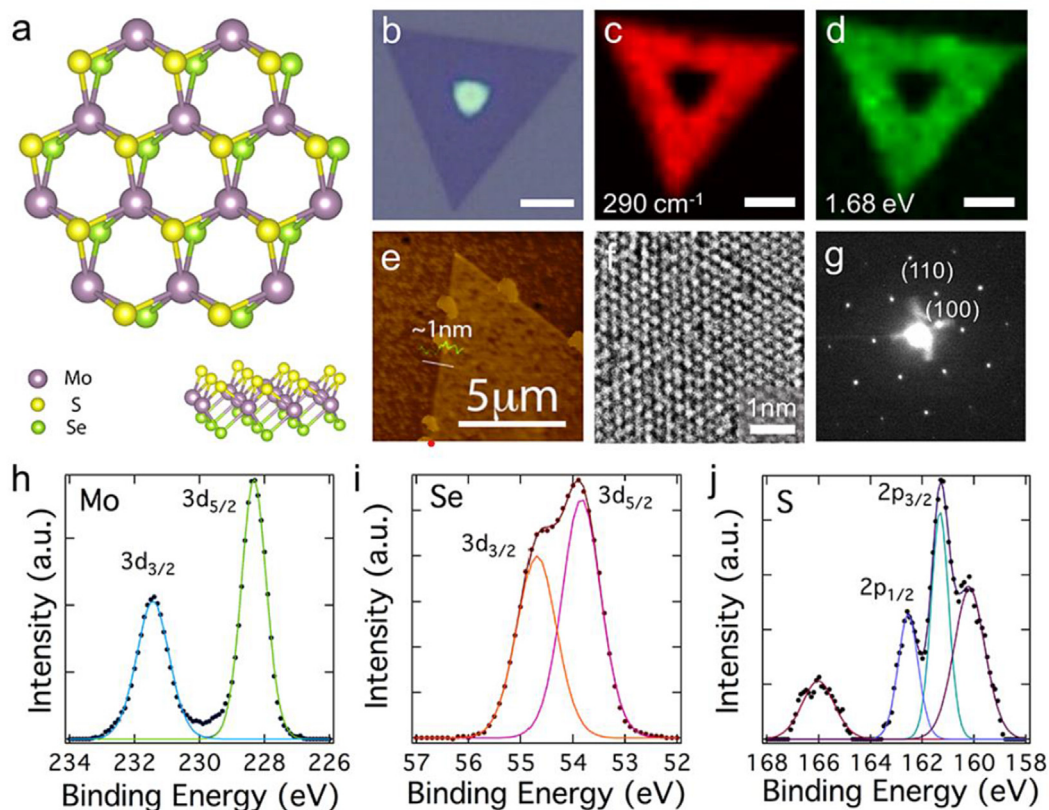


Fig. 2. Monolayer Janus SMoSe characterisations: (a) Off-angle top view and side view of an eight-unit-cell Janus SMoSe monolayer. The purple, yellow, and green spheres represent molybdenum, sulfur, and selenium atoms, respectively; (b) Optical image of a Janus SMoSe triangle. The purple and the central island with high contrast are the monolayer and bulk crystal regions, respectively; (c, d) Raman and PL peak intensity mappings of the Janus SMoSe triangle in (b). The mapping shows a uniform distribution of the identical Raman peak at 290 cm^{-1} and PL peak at 1.68 eV ; (e) AFM topography image of the Janus SMoSe triangle. The profile shows that the thickness of the flake is $< 1\text{ nm}$; (f) HRTEM image of the Janus SMoSe lattice. The atom arrangement indicates the 2H structure of the monolayer; (g) Corresponding selected area electron diffraction pattern of the monolayer; (h–j) XPS spectra of the Mo 3d, Se 3d, and S 2p core level peaks for the Janus SMoSe monolayer [18].

significantly impact the shape, size, and uniformity of the resulting Janus MoSSe layers.

Meanwhile, Qin et al. presented a novel approach for synthesising 2D Janus monolayers at ambient temperature, which incorporates in situ optical spectroscopy to monitor and actively optimise the growth process [24]. Converting them from their original classical layers, they aimed to produce Janus materials with superior quantum quality, featuring exceptionally narrow exciton line widths and minimised defects. The process, applicable to CVD or exfoliated monolayers across a range of TMDs, is conducted within a custom glass chamber with a large-diameter optical window. The chamber is connected to Raman and PL spectrometers for real-time data collection, supported by a three-axis micromanipulator stage for precise measurements.

In the initial stage of the process, the top surface of the exfoliated or CVD-grown MoSe₂ is converted to sulfur using the Selective Epitaxial Atomic Replacement (SEAR) method to yield the monolayer Janus MoSSe (Fig. 3 c). The chamber pressure is finely tuned to favour the etching of only the top Se layer, and the energy of hydrogen and sulfur radicals is adjusted to remove Se atoms while preserving the S surface selectively. Removing the top chalcogen layer enhances the bond energy of the metal and lower chalcogen layer, preventing further stripping. Maintaining a balance in plasma radical energy is crucial, as higher energy levels degrade the quality of the end product, introducing defects and vacancy formation during sulfur atom creation and replacement.

Very recently, monolayer Janus MoSSe flakes were synthesised by Sino et al. [29] through a top-down method, a controlled vertical plasma-assisted selenization process (PASP) emphasising high yield and

wafer-scale production. The synthesis procedure involves the initial production of monolayer MoS₂ flakes through conventional CVD. Subsequently, a custom-made vertical plasma-coupled furnace is employed for the transformation of monolayer MoS₂ into Janus MoSSe. This process occurs on a 4-inch diameter circular platform suitable for multiple samples or wafer-scale production. The atomic-layer substitution process utilises low-power plasma, resembling PASP, with a reaction mechanism involving the formation of H and Se radicals. The adsorption of H radicals onto the monolayer MoS₂ surface initiates the process, substituting top S atoms with Se atoms and ultimately creating Janus MoSSe. Careful control of kinetic parameters, including temperature, plasma power, and plasma time, is crucial for achieving the desired outcome. The TEM results of MoS₂ and MoSSe flakes, synthesised at different temperatures, are shown in Fig. 5.

In addition to CVD, mechanical exfoliation was also used for the preparation of Janus monolayers. For instance, Meng and his coworkers successfully produced a few layers of Janus MoSSe by mechanically exfoliating bulk MoSSe [30]. The atomic force microscope (AFM) clearly revealed the topography of 2D MoSSe, as depicted in Fig. 3 d. This accomplishment holds the potential to explore novel avenues for the growth of Janus TMDs in future applications.

Another method reported was the growth through an intercalation method. The synthesis process of Janus MoSSe monolayer through graphene-assisted bottom-face substitution was described by Bian et al. [31]. The process begins with the growth of a classical MoS₂ monolayer at the graphene/SiO₂ interface through intercalation growth. Subsequently, a substitution reagent is selectively introduced to the MoS₂/SiO₂

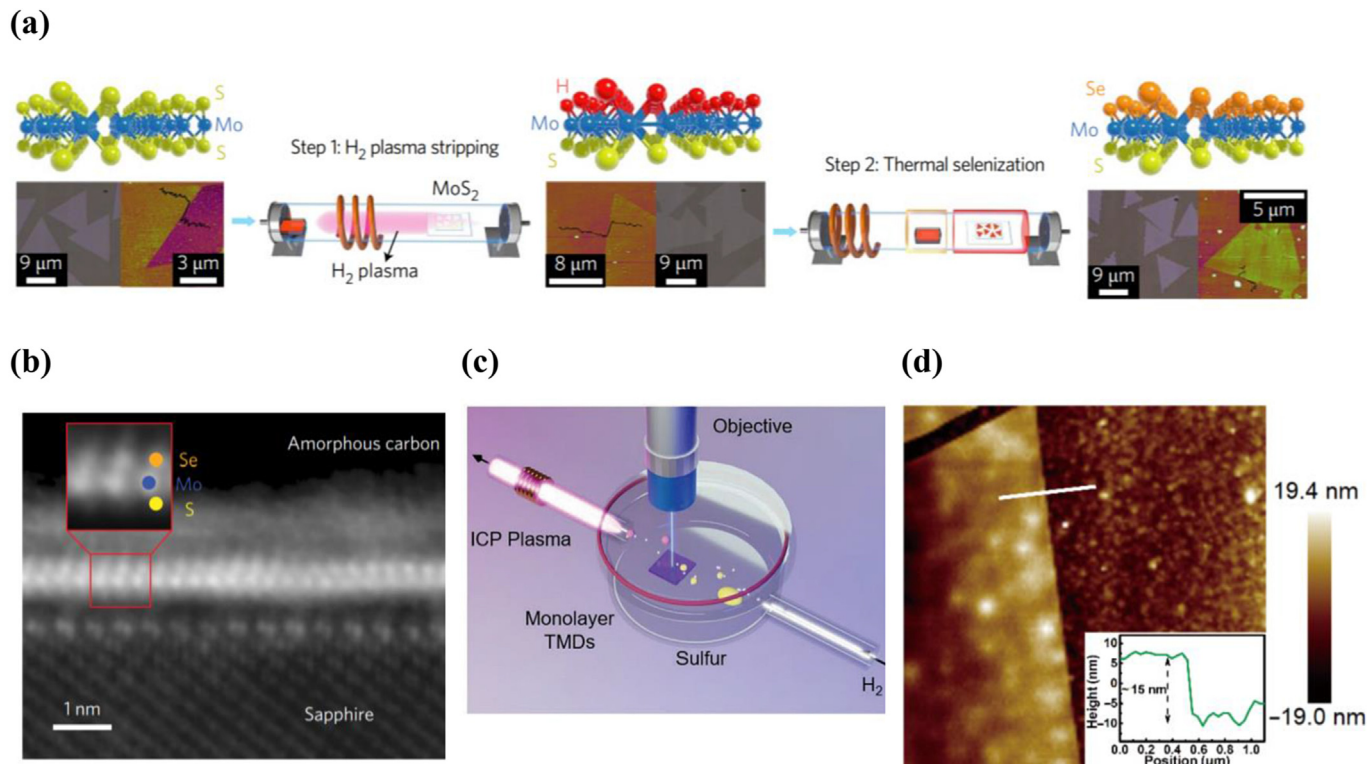


Fig. 3. (a) MoS₂ monolayer grown by chemical vapour deposition was exposed to H₂ plasma to strip the top-layer S. The plasma was then switched off, and a quartz boat loaded with Se powder was moved next to the sample without breaking the vacuum. Se powders were then thermally vaporised to achieve selenization and complete the synthesis of Janus MoSSe monolayers; (b) Annular dark-field scanning transmission electron microscopy image of the sample cross-section, showing the asymmetric MoSSe monolayer structure with Se (orange) on top and S (yellow) at the bottom of the Mo atoms (blue) [12]; (c) Schematic diagram of our custom-designed plasma chamber enabling *in-situ* optical measurement of the SEAR process. ICP labels the inductively coupled plasma ignited downstream of the chamber setup [28]; (d) Topography image of mechanically exfoliated 2D MoSSe characterised by AFM (inset: the extracted height profile of MoSSe) [24].

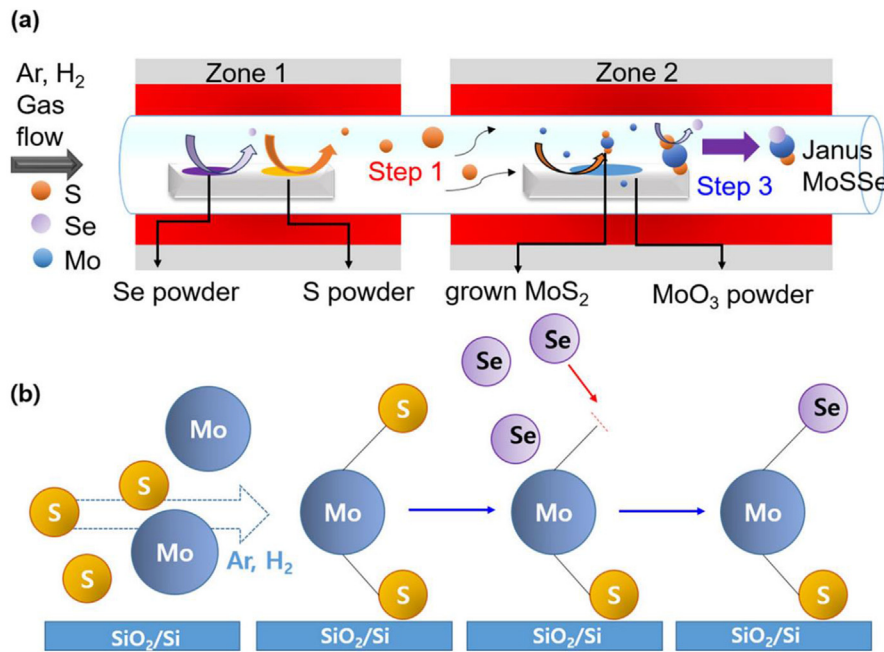


Fig. 4. Growth of Janus MoSSe. (a) CVD apparatus for Janus MoSSe. The CVD system is divided into two zones. One boat for the Se and S powders is located in Zone 1, while the other boat for the MoO₃ + NaCl powder and the SiO₂/Si substrate is located in Zone 2. The Se and S powders are separated within the boat; (b) Schematic diagram detailing the growth mechanism. The *in-situ* single growth process for MoSSe consists of three steps: synthesis of MoS₂ flakes, formation of S vacancies on the top-surface MoS₂ layer, and growth of Janus MoSSe [28].

interface, leading to S/Se substitution localised at the bottom face of the MoS₂ monolayer. The resulting Janus MoSSe monolayer exhibits a unique asymmetric structure with S and Se atoms on opposite faces. This synthesised material is then utilised for second harmonic generation

measurements, providing insights into its distinct optical properties and paving the way for potential applications in nonlinear optics and electronic devices.

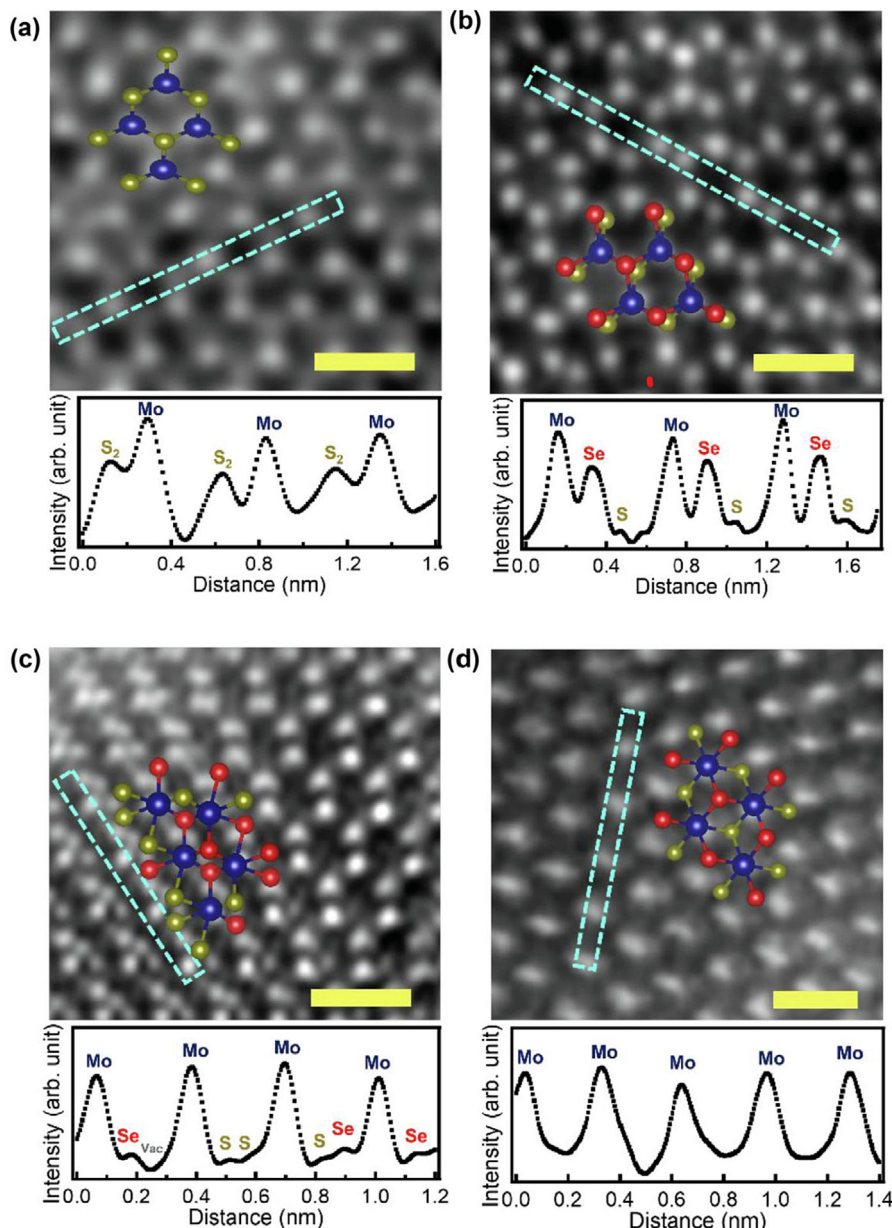


Fig. 5. TEM results of MoS₂ and MoSSe flakes. An ADF-STEM image of (a) ML MoS₂, (b) 200 °C -synthesised, (c) 400 °C -synthesised and (d) 600 °C-synthesised MoSSe. With the corresponding intensity profile. The corresponding Mo, Se, and S atoms are schematically shown in blue, red, and yellow, respectively. Scale bar, 0.5 nm. Both the 200 °C -synthesised and 400 °C -synthesised MoSSe samples are titled as indicated by the overlaid crystal structures [29].

2.2. Preparation of MoS_{2(1-x)}Se_x alloys

The 2D alloys are prepared to fine-tune the band gap of the 2D MoS₂ or MoSe₂ TMDs. In a study by Ma et al. [25], the fabrication of single-layer MoS_{2(1-x)}Se_{2x} alloys is accomplished through a carefully designed procedure, commencing with gentle Ar⁺-sputtering to remove top-layer S atoms from the CVD-grown MoS₂ films on SiO₂/Si substrates, resulting in S vacancies within the film. Subsequent exposure to an organic Se source, followed by annealing at temperatures as low as 600 K, facilitates the removal of organic moieties and the insertion of Se atoms into S vacancy sites. The entire procedure takes place within an ultrahigh vacuum (UHV) apparatus, ensuring controlled conditions for sputtering, X-ray photoelectron spectroscopy (XPS), and photoluminescence (PL) measurements.

Zhang et al. [32] utilised a home-built CVD to synthesise the monolayer MoS_{2(1-x)}Se_{2x}, where MoO₃, S, and Se powder in a quartz tube with a dual-zone horizontal tubular furnace for a controlled supply of

chalcogenide and metal sources. The growth substrate, a Si substrate with a 285 nm SiO₂ layer, was placed between quartz boats containing S and MoO₃ powder. After evacuating the tube to eliminate contaminants, ultra-high-quality argon gas was introduced. The two heating zones were then individually heated to specific temperatures (680 °C for MoO₃ and 280 °C for S) for about 15 min each, followed by natural cooling. The Ar flow rate was maintained at a constant 25 sccm throughout the process.

While Umarao et al. [33] employed a custom low-pressure two-heating zone CVD system using a 1-inch diameter quartz tube within a 30-inch horizontal tube furnace (Fig. 6 a) to achieve the monolayer MoS_{2(1-x)}Se_{2x}. It was directly grown on SiO₂/Si substrates using MoO₃, S, and Se powder. The growth conditions, including evaporation temperature and partial pressure of S/Se and MoO₃, were carefully controlled to produce large-area crystalline monolayers and multilayers of MoS_{2(1-x)}Se_{2x} in diverse shapes on SiO₂/Si substrates. A carrier gas mixture of Ar and 10 % hydrogen served both as the carrier gas and a reducing atmosphere during deposition, with hydrogen crucial for Se

vapour transport. Observations through TEM images in Fig. 6 b and Fig. 6 c distinctly indicate the crystalline nature of the synthesised monolayer $\text{MoS}_{2(1-x)}\text{Se}_{2x}$ alloy with a hexagonal structure.

A metal-organic CVD (MOCVD) method is adopted by Lin et al. [34] to synthesise monolayer MoS_2 on a 4-inch Si wafer with a 298 nm-thick thermal SiO_2 using and subsequently, the monolayer is thermally selected it to form $\text{MoS}_{2(1-x)}\text{Se}_{2x}$ in a three-zone quartz tube furnace with a 4.5-inch diameter. Se powder, acting as the CVD precursor, was heated in a quartz boat upstream to 300 °C under an H_2/N_2 (1:9) mixture at a pressure of 400 Torr, transforming into volatile selenium vapors. These vapors, carried downstream with N_2/H_2 gases, reacted with the as-grown MoS_2 on the SiO_2/Si sample during selenization at 600–800 °C for 15–60 min. The Se concentration in $\text{MoS}_{2(1-x)}\text{Se}_{2x}$ ($x = 0.12, 0.18, 0.23, 0.26$, and 1) was controlled by varying selenization temperatures and times (600, 650, 700, and 750 °C for 15 min and 800 °C for 60 min). The furnace naturally cooled down to room temperature after the synthesis.

Like CVD, PVD has also been considered a viable technique for producing TMDC films with intrinsic qualities. The only difference between the two is the phase of precursors. The precursors of PVD are in solid form, whereas in the CVD method, they are in gaseous form. The synthesis of large-area 2D semiconductor alloys $\text{MoS}_{2(1-x)}\text{Se}_{2x}$ monolayers with x ranging from 0 to 0.40 was reported by Feng et al. [35] in 2014. The synthesis involved evaporating MoSe_2 and MoS_2 powders at temperatures exceeding 940 °C in the first and second heating zones., SiO_2/Si substrates were placed in the third zone without heating for $\text{MoS}_{2(1-x)}\text{Se}_{2x}$ growth, and the growth zone operated at temperatures of 600–700 °C with a temperature gradient of approximately 50 °C/cm. The carrier gases used were Ar (2 sccm) and H_2 (0.5 sccm), and the growth system maintained a pressure of approximately 8 Pa. The growth duration typically lasted 10 min, successfully synthesising $\text{MoS}_{2(1-x)}\text{Se}_{2x}$ monolayers on SiO_2/Si substrates. In this direct PVD growth of $\text{MoS}_{2(1-x)}\text{Se}_{2x}$ monolayer alloys with Se content limited to $x = 0$ –0.40, challenges arise due to the decomposition of MoSe_2 at high temperatures. Overcoming this limitation, they introduced Se vapour during PVD in another study [36], successfully obtaining $\text{MoS}_{2(1-x)}\text{Se}_{2x}$ monolayer

alloys with a broader Se content range ($x = 0.41$ to 1.00). Additionally, by adjusting deposition parameters such as temperature gradient and deposition temperature, the study achieved monolayers with large domain sizes and distinct edge orientations, including Mo-zigzag and S/Se-zigzag edge orientations (Fig. 7 a-f).

Tan and his coworkers synthesised micrometre-sized layered bulk crystals of ternary $\text{MoS}_{2x}\text{Se}_{2(1-x)}$ using the CVT reaction technique [67], followed by electrochemical Li intercalation and exfoliation method to obtain the monolayers. Stoichiometric amounts of Mo, S, and Se were sealed in a quartz ampoule with an internal pressure of 10^{-5} to 10^{-6} torr and 40 mg of iodine as a transport agent. The sealed tube underwent a two-zone horizontal tube furnace process, initially at 800 °C for the source zone and 950 °C for the growth zone for 48 h. Subsequently, the temperature of the source zone increased to 1030 °C at a rate of 10 °C/min, with the growth zone maintained at 950 °C for an additional 120 h (Fig. 8 a-d). Single-layer ternary $\text{MoS}_{2x}\text{Se}_{2(1-x)}$ nanosheets of thickness 1.1–1.2 nm were obtained from the as-prepared bulk crystals with a high concentration of metallic 1T phase through the electrochemical Li-intercalation and exfoliation method (Fig. 8 e). The layered $\text{MoS}_{2x}\text{Se}_{2(1-x)}$ crystal powder was mixed with acetylene black and PVDF binder in NMP, coated onto a copper foil disc and dried. The resulting electrode underwent lithium intercalation in a test cell, using Li foil as the anode and 1 M LiPF_6 as the electrolyte. After discharge, the electrode was washed and sonicated to collect single-layer ternary $\text{MoS}_{2x}\text{Se}_{2(1-x)}$ nanosheets.

A simple hydrothermal method was reported by Mukherjee et al. to attain a ternary $\text{MoS}_{2x}\text{Se}_{2(1-x)}$ nanosheets followed by ultrasonication [37]. In this process, $\text{Na}_2\text{MoO}_4 \cdot 2\text{H}_2\text{O}$, S, and Se serve as precursors, while NaBH_4 acts as a reducing agent. The procedure involves dissolving $\text{Na}_2\text{MoO}_4 \cdot 2\text{H}_2\text{O}$ in DI water, adding stoichiometric amounts of S and Se, homogenising the mixture with continuous magnetic stirring, and dropwise addition of aqueous NaBH_4 . The resulting brown solution is transferred to a teflon-lined stainless autoclave, heated at 200 °C for 24 h, and naturally cooled. The obtained black powder is collected, washed, and centrifuged with DI water and IPA. The dried powder is dispersed in IPA, bath sonicated, and centrifuged to obtain nanosheets. Through this

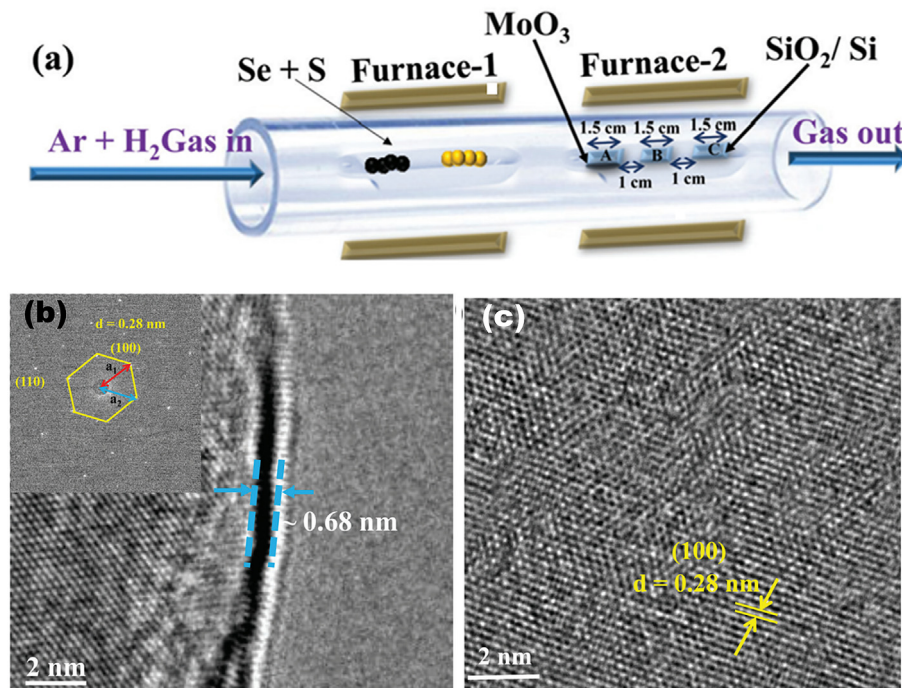


Fig. 6. (a) Illustration of the two-heating-zone furnace setup used for $\text{MoS}_{2(1-x)}\text{Se}_{2x}$ alloy growth; (b) High-resolution TEM images of the synthesised monolayer $\text{MoS}_{2(1-x)}\text{Se}_{2x}$ alloy and corresponding FFT-selected area electron diffraction patterns (insets); (c) The hexagonal crystal structure of $\text{MoS}_{2(1-x)}\text{Se}_{2x}$ (the Mo atoms and Se atoms have much higher contrast than the S atoms because of their atomic mass) [33].

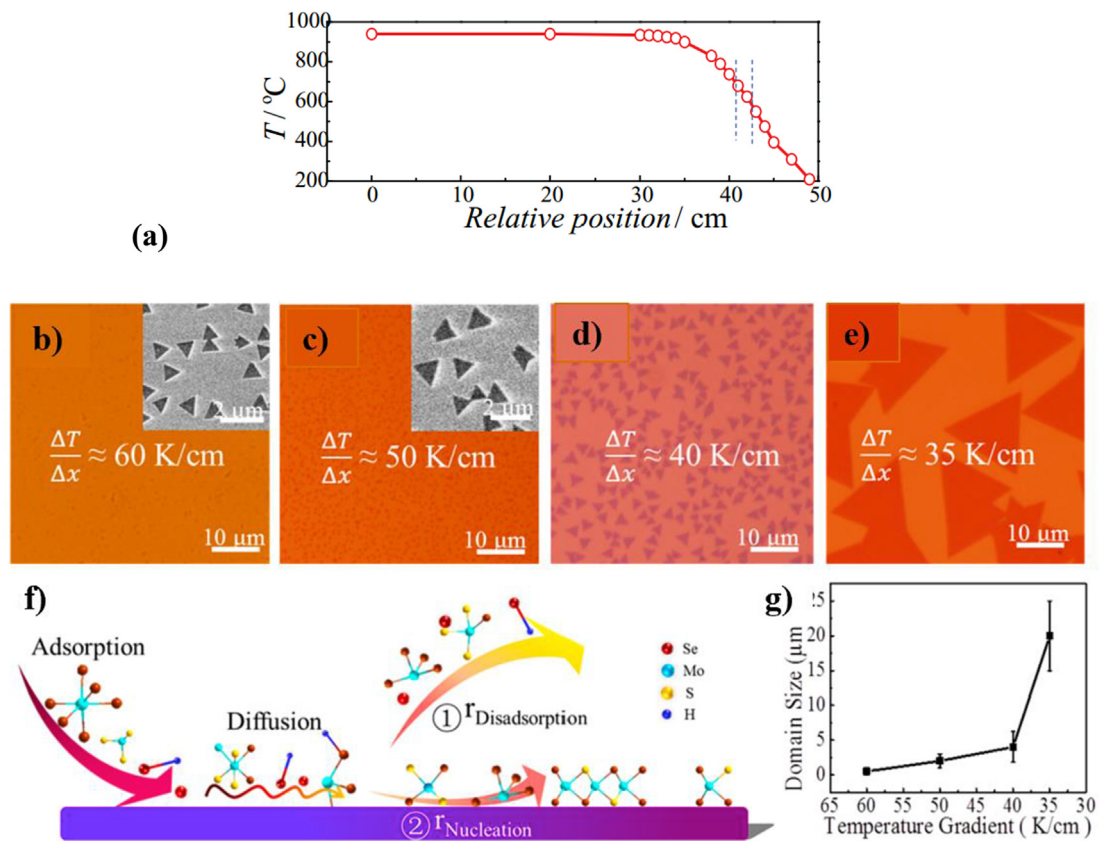


Fig. 7. (a) Tuning domain size of $\text{MoS}_{2(1-x)}\text{Se}_{2x}$ monolayers by changing the temperature gradient in the deposition zone; (b–e) Morphologies of $\text{MoS}_{0.78}\text{Se}_{1.22}$ triangles obtained at temperature gradient of (b) 60, (c) 50, (d) 40, and (e) 35 °C /cm; (f) Schematic illustration of the growth process; (g) The domain size of as-synthesised $\text{MoS}_{0.78}\text{Se}_{1.22}$ monolayer domains against the temperature gradient in the deposition zone [36].

study, the potential for synthesising these ultrathin TMDs via a chemical approach has paved the way for practical opportunities to create hybrid multifunctional devices. The HR-TEM images, along with the XRD characteristics, of the prepared ternary $\text{MoS}_{2x}\text{Se}_{2(1-x)}$ nanosheets are compared with the MoS_2 and MoSe_2 nanosheets in Fig. 9.

The successful utilisation of the synthesised 2D Janus MoSSe or alloy in particular applications hinges on both efficiency and stability. Enhancing the efficiency of these materials for applications like gas sensing, catalysis, etc., involves employing different methodologies such as surface functionalisation, doping, etc., which will be detailed in the upcoming sections. Careful management of surface chemistry is crucial for achieving optimal performance. Likewise, the engineering of band gaps assumes critical importance for their viability in optoelectronic applications. Another factor that should be kept in mind during their preparation is stability. The thermal stability of the material defines the crystallinity and attainment of defect-free materials. Similarly, the chemical stability determines its longevity and usage. Moreover, the choice of substrate can influence the overall stability characteristics.

3. General Properties

Janus MoSSe and alloy $\text{MoS}_x\text{Se}_{(1-x)}$ materials have emerged as a fascinating class of 2D layered materials with unique properties. Janus structures exhibit an inherent asymmetry, featuring two sides with different chemical compositions or properties. This asymmetry grants Janus materials versatility, allowing for tunable electronic, optical, and chemical behaviours. On the other hand, alloy $\text{MoS}_x\text{Se}_{(1-x)}$ materials, with their tunable composition, offer a remarkable degree of control over their electronic properties, including a tunable bandgap. Both material classes possess layered structures, contributing to their mechanical

strength and flexibility. This section explains some of the important properties of these materials, highlighting the unique attributes that make them promising candidates for applications ranging from catalysis and electronics to energy storage.

In this section, we will discuss each of these properties in detail.

3.1. Unique physical and chemical properties

The 2D Janus MoSSe inherits a combined crystal structure from both MoS_2 and MoSe_2 , each of which contributes distinct characteristics to its composition. This material exhibits asymmetry, with two sides featuring different chemical compositions or properties. For instance, Janus MoSSe is formed by replacing S atoms with Se atoms in MoS_2 or Se atoms with S atoms in MoSe_2 . This replacement disrupts mirror symmetry, causing a shift in the point group from D_{3h} in TMD monolayers to C_{3v} in Janus. The resulting difference in electronegativity between the top and bottom layers induces an uneven dipole distribution, creating a “colossal vertical electric field” and intrinsic strain within the Janus monolayer structure. Notably, the asymmetry leads to anisotropic behaviour in conductivity, thermal conductivity, and other physical properties in different directions [43,44]. These properties make Janus MoSSe versatile for various applications.

The electronic properties, especially the band gap of these Janus MoSSe, are reported to be an average of the band gaps of MoS_2 and MoSe_2 . The Janus SMoSe exhibits characteristics of a direct band gap semiconductor, with both the conduction band minimum and valence band maximum positioned at the K point in reciprocal space. The direct band gap energy (1.478 eV) is slightly smaller than its indirect band gap energy (1.571 eV) (Fig. 10a). Experimental photoluminescence (PL) spectra of pure MoSe_2 and Janus SMoSe in Fig. 10b samples align well

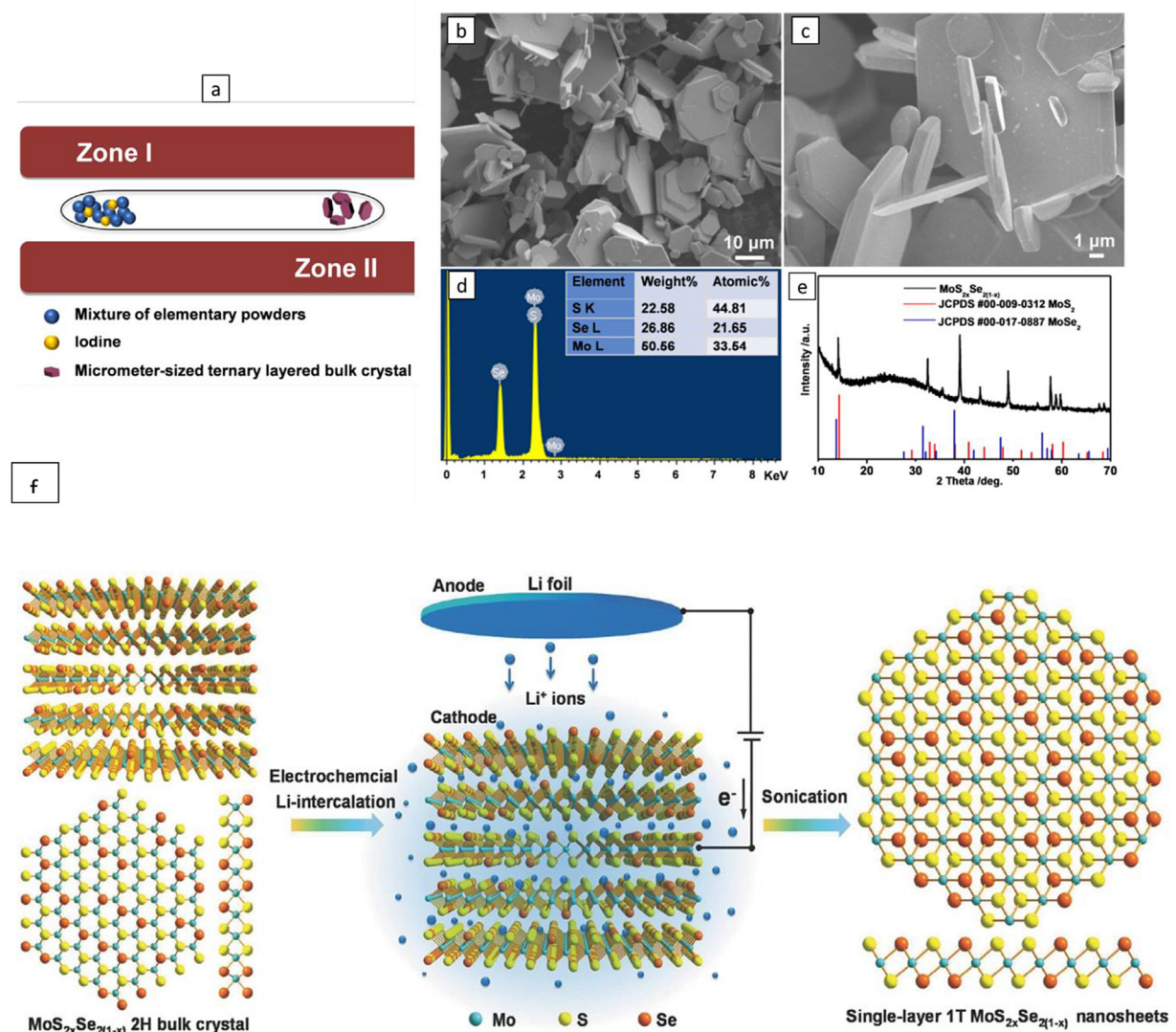


Fig. 8. (a) Schematic of the CVT synthesis of $\text{MoS}_{2x}\text{Se}_{2(1-x)}$; (b–e) SEM (b), SEM (c), EDX (d), and EDS (e) of $\text{MoS}_{2x}\text{Se}_{2(1-x)}$ bulk crystals [38]; (f) Transformation of 2H– $\text{MoS}_{2x}\text{Se}_{2(1-x)}$ bulk structure to single layer 1T– $\text{MoS}_{2x}\text{Se}_{2(1-x)}$ [38].

with theoretical predictions, with the latter showing a blue-shifted peak position, indicative of a larger bandgap compared to pure MoSe_2 [18].

The distinctive mechanical characteristics of Janus MoSSe also stem from its asymmetrical structure, which combines features of both MoS_2 and MoSe_2 . The mechanical properties of this material were determined by Shi et al. [45] using the first principles method. Concerning in-plane stiffness, Janus MoSSe exhibits a value of 106 N m^{-1} , setting it apart from other monolayer materials MoS_2 (100 N m^{-1}) and MoSe_2 (93 N m^{-1}). Crucially, all elastic constants for Janus MoSSe meet the mechanical stability criteria for 2D hexagonal crystals, confirming its robustness. The Poisson's ratio for Janus MoSSe is determined to be 0.24, slightly smaller than that of MoS_2 (0.25), indicating a tendency towards brittleness. The distinctive combination of in-plane stiffness and Poisson's ratio in Janus MoSSe hints at its potential for tailored mechanical properties, rendering it valuable for specific applications with essential characteristics.

Janus MoSSe is a material with a clear division between MoS_2 and MoSe_2 on its two sides. At the same time, $\text{MoS}_x\text{Se}_{(1-x)}$ alloy represents a continuous transition between MoS_2 and MoSe_2 across the alloy, depending on the value of x . The parameter " x " represents the fraction of S in the alloy, ranging from 0 to 1. As x increases from 0 to 1, the alloy gradually transforms from pure MoSe_2 to pure MoS_2 . These alloys exhibit a mixed chalcogenide composition combining the properties of both MoS_2 and MoSe_2 . The properties can vary by varying the composition (x)

and the synthesis method. Adjusting the amount of reactants used for the preparation can alter the composition. Fig. 10c depicts the Raman spectra trends for $\text{MoS}_{2(1-x)}\text{Se}_{2x}$ films developed by Lin et al. by the thermal selenization of the MoS_2 monolayer as a function of Se composition [34]. The Raman data distinctly reflects a trend associated with the transition from pure MoS_2 to alloyed MoSSe and, subsequently, to pure MoSe_2 as the Se composition increases.

The primary objective of alloying is to adjust the band gap of MoS_2 or MoSe_2 materials. This manipulation of electronic properties can be effectively achieved by modifying the Se/S ratio during crystal growth. For instance, Umara et al. demonstrated the ability to achieve a band gap of 1.69 eV in the synthesised $\text{MoS}_{2(1-x)}\text{Se}_{2x}$ alloy with a low Se doping percentage, which is lower than the band gap of pure MoS_2 (1.77 eV) as shown in the Tau plot in Fig. 10 d [33]. Beyond compositional variations, the band gap is also influenced by the distribution of phases and atomic arrangements of S and Se within the layered alloys. MoSSe alloys, derived through various synthesis methods, exhibit a range of morphological features, spanning from submonolayer islands to multilayer films. The alloying process can induce a structural phase transition from the 2H phase to the 1T phase, causing a shift in electronic properties from semiconducting to metallic. The introduction of Se atoms into pristine MoS_2 not only alters the overall structure of the alloy but also induces local strains, further refining the electronic structure [34].

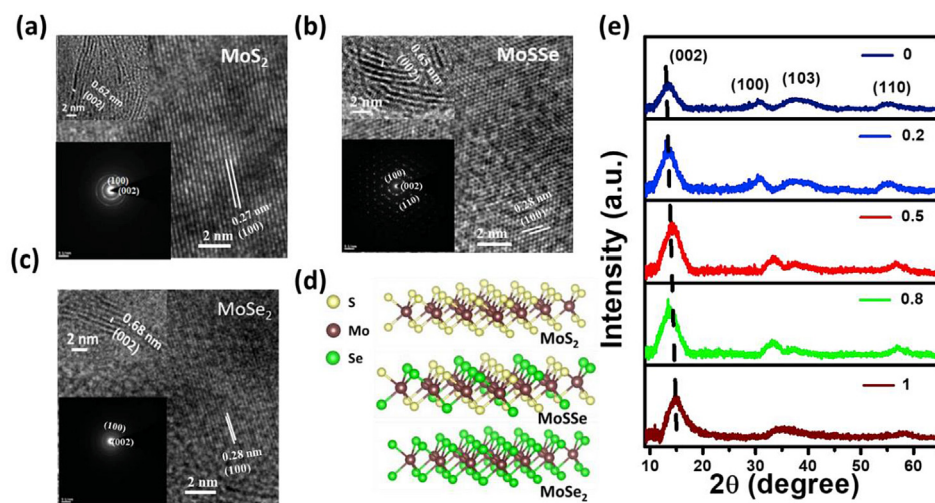


Fig. 9. Microstructural characteristics of $\text{MoS}_{2x}\text{Se}_{2(1-x)}$ alloys. (a-c) High-resolution TEM images of MoS_2 (a), MoSSe (b), and MoSe_2 (c) nanosheets with a corresponding interlayer spacing of (002) plane (top Inset) and SAED patterns (bottom Inset); (d) Schematic structures of monolayer MoS_2 , MoSSe and MoSe_2 nanosheets; (e) XRD patterns of different composites of $\text{MoS}_{2x}\text{Se}_{2(1-x)}$ alloys with varying x [37].

3.2. Structural properties

Molybdenum disulfide selenide (MoSSe) is a layered material with a crystal structure that can be described as a combination of molybdenum disulfide (MoS_2) and molybdenum diselenide (MoSe_2) structures [20]. The Janus MoSSe sheet is a two-dimensional hexagonal structure with primitive cell vectors a_h and b_h , containing three vertically displaced atoms in different atomic layers. The sheet consists of Mo, S, and Se atoms, with Mo atoms having six-fold coordination and S/Se atoms having three-fold coordination. An orthogonal supercell defined by a_o and b_o vectors allows for direct quantification of charge-carrier mobility along the zigzag and armchair directions. The optimized structural parameters for the periodic MoSSe sheet are $a_h = b_h = 3.21 \text{ \AA}$, with a Mo-S bond length of about 2.41 \AA and a Mo-Se bond length of about 2.52 \AA [46] (see Table 1).

The structural detail of a few MoSSe configurations is listed in Table 2.

The MoSSe sheet has an asymmetric structure that induces novel emerging properties in low-dimensional materials [48]. It can be patterned into armchairs and zigzag nanoribbons, with the nanoribbon width defined by the number of repeating units along the non-periodic in-plane direction. The Mo-S and Mo-Se bonds at the edges of the nanoribbon are larger than those at the innermost part. The Janus MoSSe sheet is a direct-gap semiconductor with a band gap of about 1.66 eV and has an intrinsic dipole of about 0.037 e \AA perpendicular to the sheet's plane. The hole carrier mobility is about $157.2 \text{ cm}^2 \text{ V}^{-1} \text{ s}^{-1}$, which is larger than the electron carrier mobility of about $73.8 \text{ cm}^2 \text{ V}^{-1} \text{ s}^{-1}$ due to the smaller deformation potential of the valence band [46].

Janus TMDs have multiple isomers, including the $1T'$ phase and the $2H$ phase for monolayer structures. The $2H$ phase of MoSSe refers to a hexagonal crystal structure in which the molybdenum and sulfur atoms are arranged in a layered structure with selenium atoms filling the gaps between the layers. The $2H$ phase has a centrosymmetric crystal structure and is the most stable phase of MoSSe [50]. The $1T$ phase of MoSSe refers to a distorted octahedral crystal structure in which the molybdenum atoms are coordinated by six sulfur and/or selenium atoms. This phase is non-centrosymmetric and has a lower symmetry than the $2H$ phase. The $1T'$ phase of MoSSe refers to a distorted tetrahedral crystal structure in which the molybdenum atoms are coordinated by four sulfur and/or selenium atoms. This phase is also non-centrosymmetric and has a lower symmetry than the $2H$ phase. The $1T$ and $1T'$ phases of MoSSe are metastable. They can be induced by chemical or physical treatments,

such as doping, strain, or exfoliation, and can exhibit interesting electronic and optical properties that are different from those of the $2H$ phase (Fig. 11d and e) [50].

The most common multilayer structures are AA, AB, and AC (or AA'), in Fig. 11f illustrating their lattice structures [51]. Because of the greater mass of Se atoms, the bandgap and energy splitting at the K high-symmetry sites of the MoSSe monolayer are bigger than those of MoS_2 and MoSe_2 . All MoSSe bulks have indirect bandgaps and valence band edges that are moved to the points. Because of the interaction between van der Waals interlayer contacts and spin-orbit coupling (SOC) effects, the valence band SOC splitting (Rashba splitting) energies at the Dirac points are lower than those of the monolayer. At the VBM and CBM at the K point, the d orbital of Mo atoms and the p orbital of S atoms contribute primarily to the highest energy level. Still, at the Gamma point, the highest energy level is composed of a p orbital of S atom and Mo atom.

Zhang et al. [52] further classified the stacking of multilayers into 3 different categories.

- Type 1: the orientation of the dipole moment is identical in both the MLs
- Type 2: the orientation of the dipole moment is opposite in both the MLs
- Type 3: the orientation of the dipole moment is back facing in both the MLs

When these 3 categories are introduced in the previous classification, a total of 9 types of structural variation are generated, as shown by Zhang et al. [52]. All these different types of MoSSe structures are classified in Fig. 12.

Wei et al. [51] compared the band structure of MoSSe monolayers (ML) with MoSe_2 and MoS_2 , and they also compared the difference in the band structure with different stacking orders of AA, AB, and AC. The conduction band minimum (CBM) and valence band maximum (VBM) for all three monolayers are found at the K high-symmetry sites, with direct bandgaps of 1.36 eV (MoSe_2), 1.49 eV (MoS_2), and 1.78 eV (MoSSe). When the spin-orbit coupling is examined, the valence band edge exhibits considerable energy splitting at the K high-symmetry sites for all three monolayers. Because of the greater mass of Se atoms, the splitting for MoSSe is somewhat bigger [51,53].

In the bulk structures, the band structures are drastically changed by interlayer coupling, similar to MoS_2 [54]. All MoSSe bulks exhibit

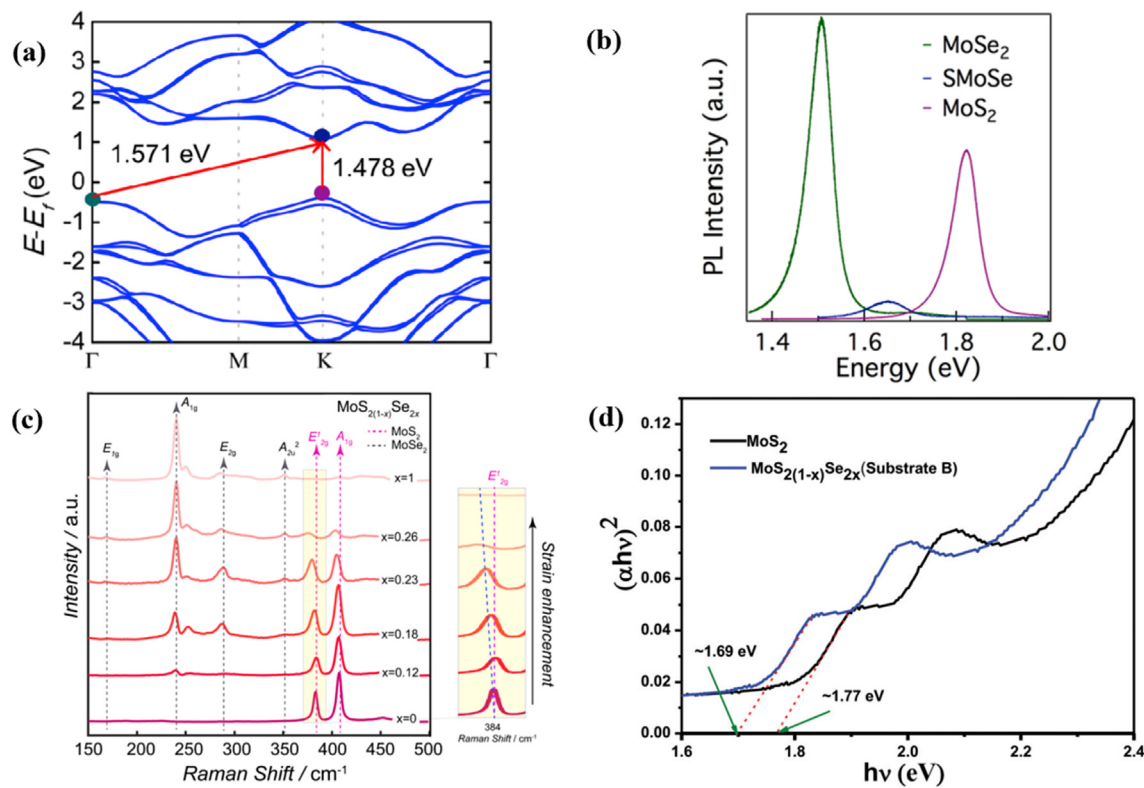


Fig. 10. (a) Predicted band diagram of monolayer Janus SMoSe. The direct and indirect bandgaps at K and Γ points are calculated to be 1.478 and 1.571 eV, respectively; (b) PL (under 532 nm diode laser excitation) spectra of MoSe₂, Janus SMoSe, and MoS₂ [18]; (c) Raman spectroscopy was utilised to examine the formation of $\text{MoS}_{2(1-x)}\text{Se}_{2x}$ compounds. It shows an evolution of structure and chemical composition from MoS₂ to MoSSe and eventually MoSe₂ [34]; (d) Tauc's plot for band gap calculation of the $\text{MoS}_{2(1-x)}\text{Se}_{2x}$ alloy [33].

indirect bandgaps, with valence band edges shifted from the Dirac points to the G points [51]. The indirect bandgaps have energies of the values 0.792 eV (AC), 0.808 eV (AB) and 1.48 eV (AA). In comparison, the direct bandgaps are still at the Dirac points with energies of values 1.54 eV (AA), 1.43 eV (AB) and 1.46 eV (AC) (see Fig. 13). The valence band SOC splitting energies at the Dirac points are about 60 meV for AA stacked and nearly vanished for the other two types of bulk due to competitive van der Waals interaction and Spin-orbit coupling [51,55]. Zhang et al. [52] reported that the distance between adjacent Mo atomic planes in the bilayers is determined by the size and electronegativity of the atoms in the adjacent layers, with AA stacking having the largest distance due to the nature of the arrangement of S and Se [52]. The band gap of each configuration is also different and varies from 1.58 to 2.19 eV. Type-1 configurations have the smallest band gaps, while type-3 has the largest. The charge distribution of the band structures reveals that type-1 configurations and 2-AB and 3-AB have a type-II band alignment, making them favourable for the formation of interlayer excitons [52].

Guan et al. [20] discussed 5 high symmetry stacking patterns, which are the smallest MoSSe multilayer systems stacked by van der Waals (vdW) interactions. The A'B configuration is found to be the most stable structure, with the smallest interlayer vertical distance, d , and binding energy, E_b . The electronic properties of bilayer MoSSe are found to be related to the stacking orders. The A'B configuration is an indirect semiconductor with a gap of 1.47 eV, while AA' and AA-SSe have direct band gaps of 1.39 and 1.22 eV, respectively [20]. The other two configurations, AA-SeSe and AA-SS, have different band alignments, with the valence band maximum (VBM) located at the K point for AA-SeSe and at the midpoint along the K- Γ symmetry lines for AA-SS. The bilayer MoSSe's DFT-D2 calculated band alignment is compared with the water redox potential to explore its potential applications in photoelectrochemical water splitting [20].

Both these work has been summarised in Table S1.

3.3. Optical properties

The study of how electromagnetic radiation interacts with the MoSSe monolayer can reveal insights into the optical properties of the material, which can be portrayed through a vital term called dielectric function ($\epsilon(\omega)$). The real and imaginary parts of $\epsilon(\omega)$ determine the important optical parameters like optical absorption coefficient ($\alpha(\omega)$), extinction coefficient ($k(\omega)$), refractive index ($n(\omega)$), energy loss function, etc. The imaginary part of the dielectric constant calculated with combined HSE06 + GOW0+BSE methods to consider the strong excitonic effects in MoSSe is shown in Fig. 14a. The first peak occurs at an energy of 2.15 eV, approximately equal to the bandgap of the monolayer, which implies that the photoexcited electrons can easily move from the VBM to the CBM. A pronounced absorption is viable in the visible energy range (1.63 eV–3.12 eV); therefore, the MoSSe monolayer can be utilised for devising energy harvesting electronics [20].

The Janus MoSSe monolayer strongly absorbs electromagnetic radiation in the Infrared and visible energy regime (Fig. 14 c). Fig. 14 c shows the optical $\alpha(\omega)$ spectra of both in-plane and out-of-plane polarisation vectors, which are anisotropic below 11 eV and show isotropic nature in the high energy range. The largest peak, around 10.2 eV, is because of the strong excitonic effects in the unusual higher energy [18, 56]. The spectra of reflectivity ($R(\omega)$), another optical parameter, of the Janus MoSSe in the photon energy range of 0–20 eV are displayed in Fig. 14 b. A noticeable reflectivity was observed in the moderate Visible-UV region (0–7.5 eV) as well as in the UV light region (9.5–14.5 eV). The $R(\omega)$ spectra of Janus MoSSe in the UV and vacuum-UV energy range affirms its similarity with that of the MoS₂ monolayer [18, 56].

The optical properties can be tailored by either replacing the Se or S atom with anions or creating Vander wall heterostructures. Doping by rare earth metals like La and Ce has effectively modulated the optical

Table 1

Advantageous and disadvantageous of different synthesis methods.

Synthesis techniques	Advantageous	Disadvantageous	Ref.
Janus MoSSe			
1. Mechanical exfoliation	<ul style="list-style-type: none"> • Direct fabrication without additional complex synthesis techniques. 	<ul style="list-style-type: none"> • It is not suitable for large-scale production due to its low throughput. 	[39]
2. Selective Epitaxial Replacement (SEAR)	<ul style="list-style-type: none"> • Allows the synthesis of Janus MoSSe or their heterostructures at room temperature 	<ul style="list-style-type: none"> • Necessitates precise control over radical species, plasma properties, and metal-chalcogen bonds 	[39]
3. CVD	<ul style="list-style-type: none"> • Controlled substitution offers flexibility in adjusting the chemical composition. • No need for an activated atom supply. • Simple and cost-effective. 	<ul style="list-style-type: none"> • Complex and costly since it depends on the follow-up treatments. • It requires additional plasma or elevated temperature treatments. • A comprehensive overview of various aspects of 2D Janus MoSSe and $\text{MoSe}_x\text{S}_{(1-x)}$ alloy, a transition metal dichalcogenide, including the material properties such as strong light-matter interaction and piezoelectricity, alongside synthesis methods like CVD. It covers structural forms, modification techniques (doping, strain engineering), and applications in energy and electronics while noting scalability and toxicity as limitations. Achieving large and uniformly structured Janus crystals with minimal defect density necessitates meticulous optimization of the preparation conditions, posing a significant challenge. 	[40, 41] [28]
4. Intercalation method	<ul style="list-style-type: none"> • Enables controlled synthesis and manipulation of the chemical composition. • Offer scalability for large-scale production. 	<ul style="list-style-type: none"> • Complex process • Require additional processing steps for intercalation and subsequent removal of intercalated species. 	[31]
Alloy MoSSe			
1. CVD	<ul style="list-style-type: none"> • Fewer surface contaminants • Easy to produce large, scalable crystal domains and continuous films of 2D alloys on various substrates 	<ul style="list-style-type: none"> • Only a few alloys can be prepared by this method. • During alloying selenization, high-temperature chalcogen ion exchange may introduce defects, becoming sites for water or oxygen adsorption from the surroundings. 	[34]
2. PVD	<ul style="list-style-type: none"> • Precise control over film thickness. • Allows for layer-by-layer growth. • Less contamination 	<ul style="list-style-type: none"> • Limited scalability for large-area growth. • It may require high vacuum conditions, leading to equipment complexity. 	[42]
3. Sono-hydrothermal	<ul style="list-style-type: none"> • Green synthesis • Cost-effective • Mild reaction conditions 	<ul style="list-style-type: none"> • Limited scalability • Requires careful consideration to ensure 	[37]

Table 1 (continued)

Synthesis techniques	Advantageous	Disadvantageous	Ref.
	<ul style="list-style-type: none"> • Facile Control over Alloy Properties 	<ul style="list-style-type: none"> proper control over alloy formation. • Sonication-Induced Structural Modifications 	

Table 2

Geometrical details of various configurations of MoSSe [20,46,47].

Configuration	Lattice constants (Å)		Bond length (Å)	
	a	b	Mo-S	Mo-Se
MoSSe sheet	3.21	5.57	2.41	2.52
MoSSe armchair	–	5.55	2.42	2.57
MoSSe zig-zag	3.20	–	2.38	2.53
MoSSe 1T	3.22	–	2.41	2.57
MoSSe 2H	3.25	–	2.42	2.53

properties of MoSSe. The imaginary part of the $\epsilon(\omega)$ of the doped systems is depicted in Fig.S14d and 14e. The dominant adsorption peaks are in the visible region and some others in the UV region. Compared to the pristine case, it is found that the La and Ce doping caused a shift in the adsorption peaks towards the longer wavelength region (redshift) [57].

The optical properties in the MoSSe alloys can be tuned by varying the Se or S compositions. For instance, the optical band gap of the $\text{MoS}_{2x}\text{Se}_{2(1-x)}$ alloys is observed in the red part of the visible spectrum (1.65–2 eV) [58]. Similarly, the optical band gap in the $\text{MoS}_{2(1-x)}\text{Se}_{2x}$ synthesised through CVD is found to be broadened from 1.55 eV in MoSe2 to 1.97 eV by controlling the compositions in the precursor [32].

3.4. Vibrational properties

Raman spectroscopy is an important spectroscopic technique used to obtain the vibrational modes of a molecule, and it is typically used to provide a structural fingerprint from which the molecules can be recognised. For the 2D TMDs like MoS_2 and MoSe_2 , there exist two active vibrational modes in the Raman spectra: A_{1g} at frequencies 396.3 cm^{-1} and 234.9 cm^{-1} , and E_{2g}^1 modes at frequencies 373.1 cm^{-1} and 276.9 cm^{-1} respectively for MoS_2 and MoSe_2 monolayers. But for the Janus MoSSe monolayer, as per the DFT study, it is predicted that in addition to the A_{1g} and E_{2g}^1 modes at 283.1 cm^{-1} and 343.5 cm^{-1} respectively, there exists an additional mode B_{2g}^1 at frequency 427.8 cm^{-1} . Experimentally, this peak is obtained around the frequency of 436.4 cm^{-1} , confirming its existence. The theoretically predicted spectra of Janus MoSSe are shown in Fig. 15. The broken symmetry along the out-of-plane direction enables the third mode to be active for the MoSSe monolayer [18].

Petric et al. [59] collected the Raman spectra of Janus TMD monolayers obtained from crystals grown via room temperature selective epitaxy atomic replacement method (SEAR) with a laser excitation wavelength of 633 nm and 532 nm at room temperature and cryogenic temperatures, respectively. The frequencies of Raman modes at different excitation wavelengths at room temperature and 10K are tabulated. From Fig. 15b, it is evident that the Raman spectra are strongly influenced by the exciton wavelength.

Oreshonkov et al. [60] very recently simulated the Raman spectrum of 1H MoSSe monolayer and predicted the Raman spectra of 1T, 1T', and 1H' polymorph modifications of MoSSe. The spectral profile of the honeycomb modifications of MoSSe, i.e., 1H and 1T were similar (Fig. 15c and d) [60]. The non-degenerate A_1 modes represent an out-of-plane movement of atoms, whereas the doubly degenerate E modes denote in-plane vibrations (Fig. 15e). But the spectra of 1T' and 1H' phases were dissimilar and are easily distinguishable in terms of the number of intense bands and the spectral range. For the 1T' phase, the range of the spectrum starts at 100 cm^{-1} , while it begins at 50 cm^{-1} for

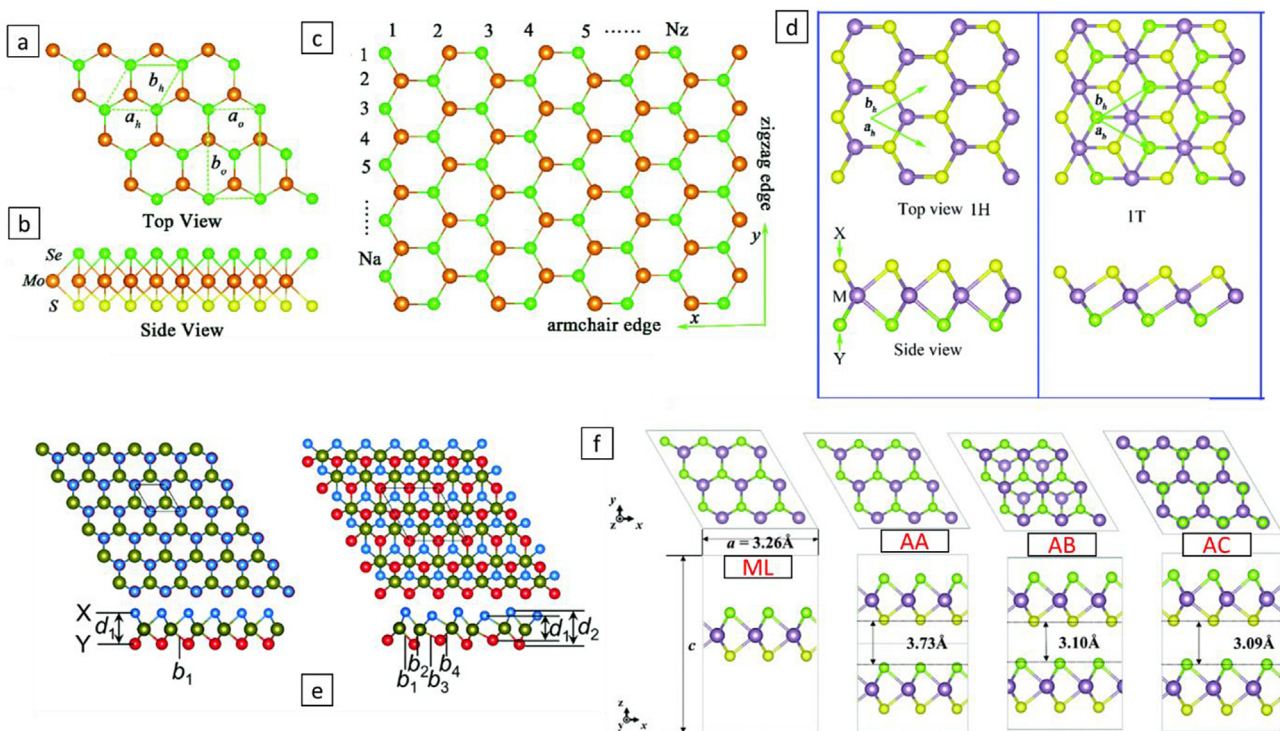


Fig. 11. (a–c) Structure of MoSSe from different angles [46]; (d) Crystal arrangement of 1H and 1T MoSSe structure [49]; (e) 2H (left) and 1T' (right) arrangement of MoSSe ML [50]; (f) Stacking sequence of bilayer MoSSe (AA, AB, AC) [51].

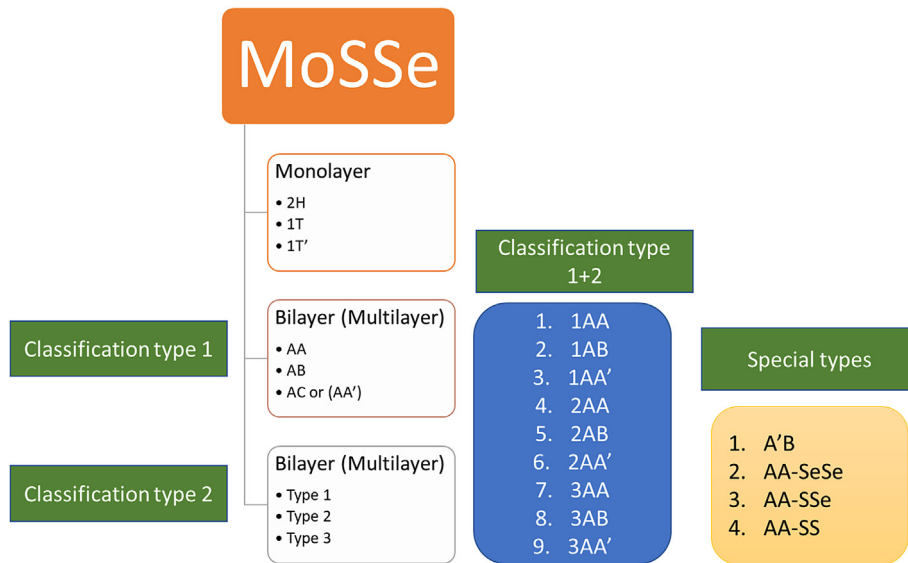


Fig. 12. Types of MoSSe stacking.

the 1H' phase, and this difference is attributed to the difference in their structural phases.

3.5. Magnetic properties

Generally, the Janus TMDCs are intrinsically non-magnetic in nature. To extend the application of these materials for spintronic applications, an emerging technology that exploits the spin degree of freedom, the introduction of magnetism in the material is a must. Various approaches like transition metal (TM) doping, defect engineering, chirality,

adsorption of surface atoms, etc., are the common methodologies adopted to introduce the same.

First principle calculations by Guan et al. [61] suggested that the substitutional doping of TMs like Fe, Co, Mn, Cr, and V have induced magnetism in the MoSSe monolayer. The TMs replaced a Mo atom in the MoSSe monolayer, and the obtained magnetic moment was 0 μB , 1.00 μB , 2.00 μB , 3.00 μB , and 4.00 μB , respectively, for Cr-, Mn-, Fe-, Co- and Ni-doped systems. The doped TM atoms completely contribute to these magnetic effects in MoSSe. The spin-resolved Total density of states (DOS) plot for TM-doped MoSSe is shown in Fig. 15f and the asymmetric

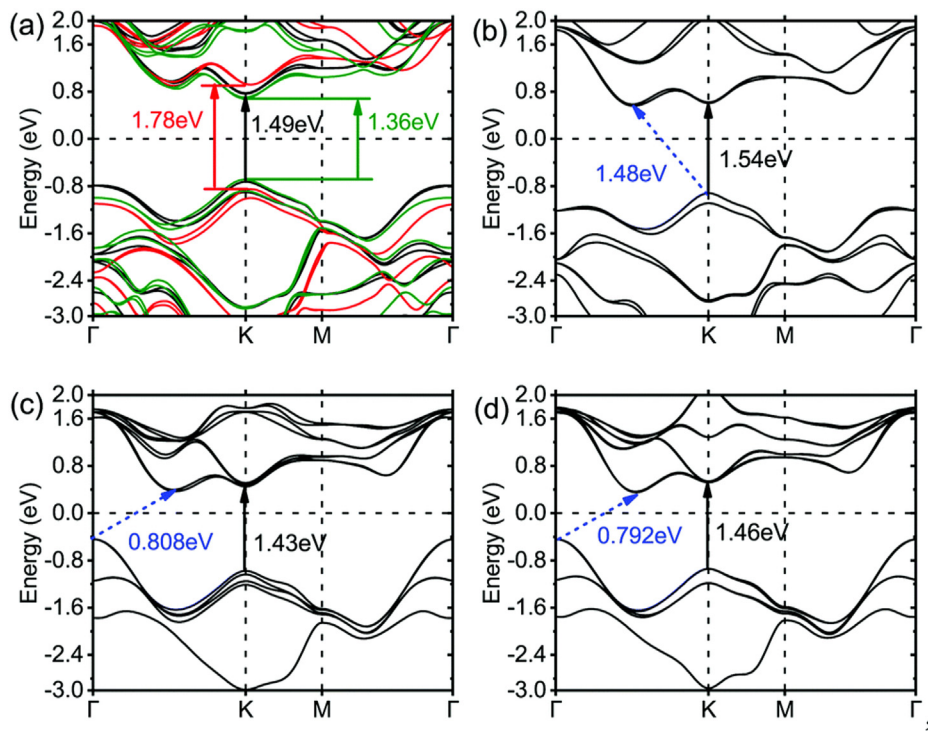


Fig. 13. Band structures of (a) MoSSe monolayer, (b) AA stacking, (c) AB stacking, and (d) AC stacking [51].

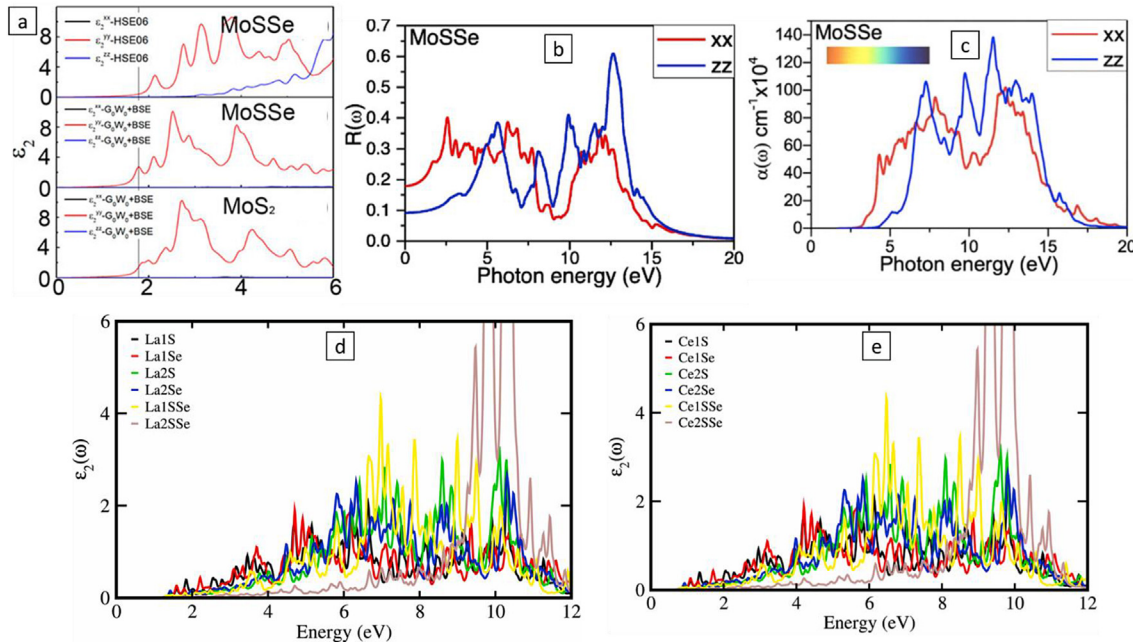


Fig. 14. (a) The imaginary part of the $\epsilon(\omega)$ for pristine MoS₂ and MoSSe [20]; (b) Reflectivity of MoSSe [56]; (c) Optical absorption coefficient of MoSSe [56]; (d) The imaginary part of the $\epsilon(\omega)$ in La-doped MoSSe [57]; (e) The imaginary part of the $\epsilon(\omega)$ in Ce doped MoSSe [57].

spin states around the Fermi level (at 0 eV) are an indication of the induced magnetic moments in the system [61].

The effect of antisite and complex defects on the magnetic structure of the Janus 1T' MoSSe monolayer was examined by Li et al. [62]. The antisite defects are formed by replacing the Mo atom with Se or S atoms and vice versa. Due to the presence of two non-equivalent S/Se labelled by A and B in 1T' MoSSe, eight antisite defects can be formed. But only two of them, namely Mo-Se(A) and Mo-S(A) defects, generated a spin splitting in the total DOS, and the determined local magnetic moments

were 0.89 μB and 1.04 μB , respectively. These magnetic moments originate primarily from the d orbitals of the antisite Mo atom and partially from the Se/S p orbitals. In the complex defect formation, one Mo atom, three S atoms and three Se atoms are removed (MoAS3Se3 and MoBS3Se3). Both induced spin polarisation in the system, with a local magnetic moment of 1.94 and 1.56 μB , for MoAS3Se3 and MoBS3Se3, respectively. The two Mo atoms close to the vacancy render these magnetic moments.

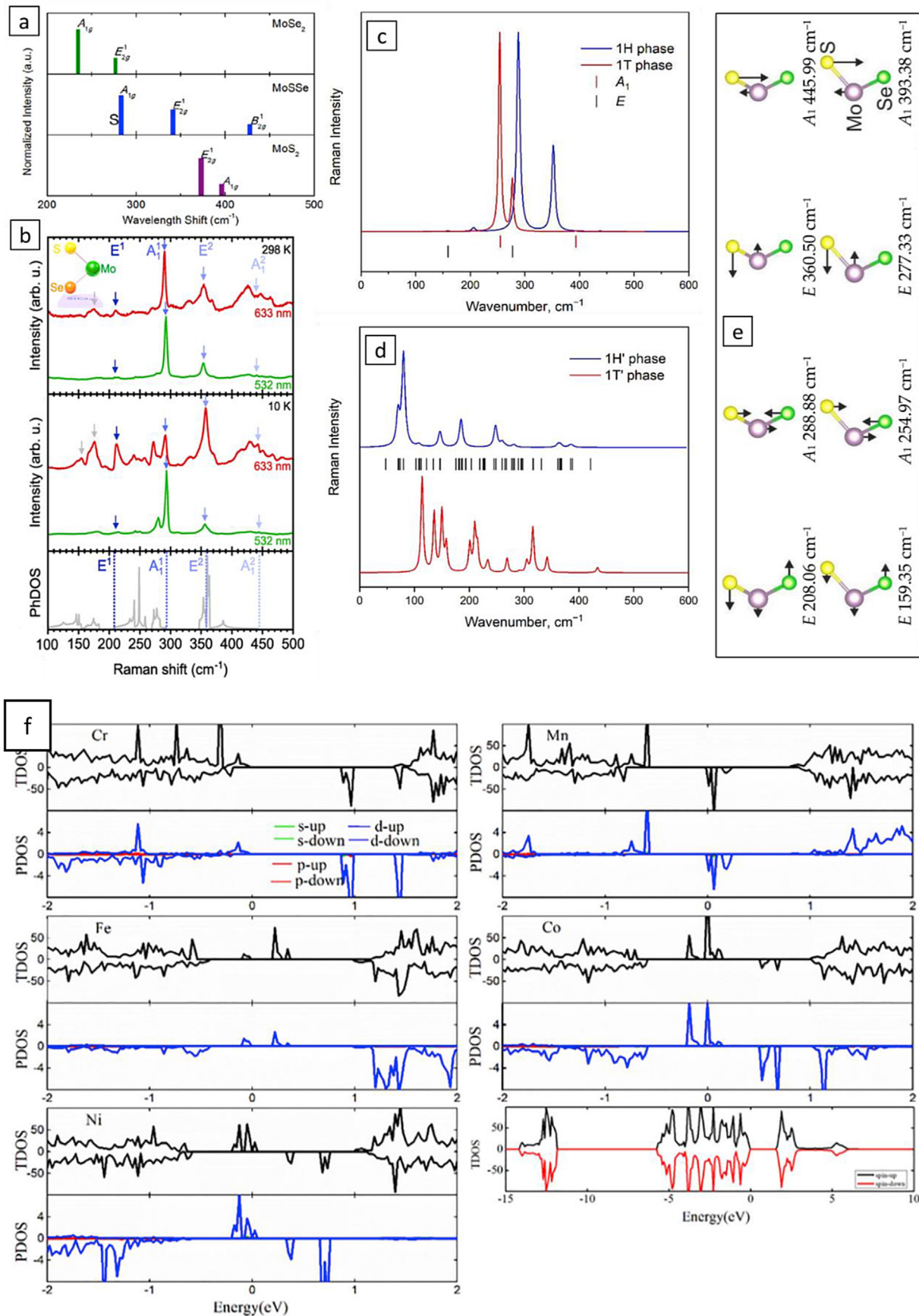


Fig. 15. (a) Predicted Raman spectra of MoSSe in comparison with MoS₂ and MoSe₂ [18]; (b) Raman spectra of MoSSe and computed first order phonon modes [59]; (c) 1H and 1T Raman spectra of MoSSe [60]; (d) 1H' and 1T' Raman spectra of MoSSe [60]; (e) Modes of vibration presented [60]; (f) DOS of transition metal doped MoSSe [61].

3.6. Catalytic properties

Among different 2D materials exploited so far, 2D TMDCs are often used as a possible catalyst for HER and OER owing to their unique features. But the basal plane of the 2H phase of TMDCs like MoS₂ is catalytically inert, and the activity emerges from the active edge sites. As a result, many initiatives have been taken to enhance the catalytic activity of the edge sites by doping or defect induction etc. The basal planes of 2D TMDCs are activated by applying large-scale tensile strength along with vacancy defects.

The mirror asymmetry structure produces an inherent strain and electric field (EF), which in turn offers an exemptional catalytic property to the Janus MoSSe monolayer compared to the pure TMDCs. However, the basal plane of the Janus MoSSe monolayer is catalytically inactive. The DFT studies have proven that the catalytic activity of the basal plane of Janus monolayers can be improved without the application of large-scale tensile strains or a substantial density of vacancies. Generally, defects like point defects (PDs), line defects (LDs) and grain boundaries (GBs) can promote the catalytic performance of the 2D monolayers. Shi et al. [63] theoretically examined how inherent defects like PDs and GBs affect the catalytic performance of Janus MoSSe for HER reactions. Nine types of GBs and 12 types of PDs were considered for the investigation. For the adsorption of H on the pristine MoSSe, the Gibbs free energy (ΔG) was +1.99eV, implying that its basal plane was catalytically inactive for the application of HER. The ΔG diagrams for the H adsorption in defective MoSSe are in Fig. 16a and b. Those defects with large -ve ΔG can break the bond for the formation and release of H_2 . The study also showed the difference in the charge distribution between the Se and S in the system, with S vacancies allowing the internal EF to remain in the system. This internal EF endows the same impact for triggering the catalytic performance shown by the externally applied strain in the MoS_2 monolayer. Therefore, defecting the Janus MoSSe monolayer is the best way to significantly instigate catalytic activity for HER.

Another method predicted to improve the OER, and HER catalytic performance is the single metal atom anchoring on the Janus MoSSe monolayer surface. Wang et al. [64] modified the MoSSe surface with the TMs like Fe, Co, Ni, Ru, Pd, Ag, Ir, Pt and Au to explore the same. In terms of catalytic performance, Ni@MoSSe and Fe@MoSSe were the best for OER and HER, respectively with lower overpotential (Fig. 16 d), and near zero ΔG values (Fig. 16 c). When the TMs are attached, the TM and the Mo atom lose their charge to the S and Se atoms. The S atoms gain a more significant amount of charge than the Se atoms, thereby redistributing the overall charge of the system. In addition to the charge redistribution, the modest energy level of the d-band centre of the TM also adds to the amplification of the catalytic activity. They have also investigated the impact of applied strain on the Fe and Ni@MoSSe on the catalytic performance and suggested that the catalytic activity can be enhanced by appropriately regulating the values of the externally applied strain [64]. Similarly, Li et al. [65] embedded the TMs like Sc, Mn, V, Fe, Co, Nb, Mo, Cu, Zn, Y Ru, Rh, Pd, Ag and Cu by creating single S or Se vacancies in the Janus MoSSe monolayer for the N₂ reduction to NH₃. Among the metals embedded, the -ve value of ΔG for N₂ adsorption is observed only in V, Fe, Co, Nb, and Mo embedded systems (Fig. 16 e). But the Mo embedded system has the highest catalytic activity and NH₃ desorption barrier. In addition to the NRR, they have also analysed the feasibility of Mo@MoSSe as the HER catalyst, but it is found that a lower value of ΔG (N₂) suggests that the NRR selectivity of Mo-embedded MoSSe is much higher than that of the HER [65]. Besides the 2H phase, the catalytic performance of the square phase (1S) of the Janus MoSSe monolayer is also exploited. Similar to their 2H phase, the basal plane of 1S is catalytically inactive. The induction of vacancy defects can activate the catalytic activity for HER in the 1S phase [66]. Lai et al. [66] also investigated the effect of strain on the catalytic activity of 1S–MoSSe, and it was found that tensile strain increases the ΔG value, whereas the compressive strain has the opposite effect, and both do not alter the structural stability of the material. 1S–MoSSe associated with Se vacancy

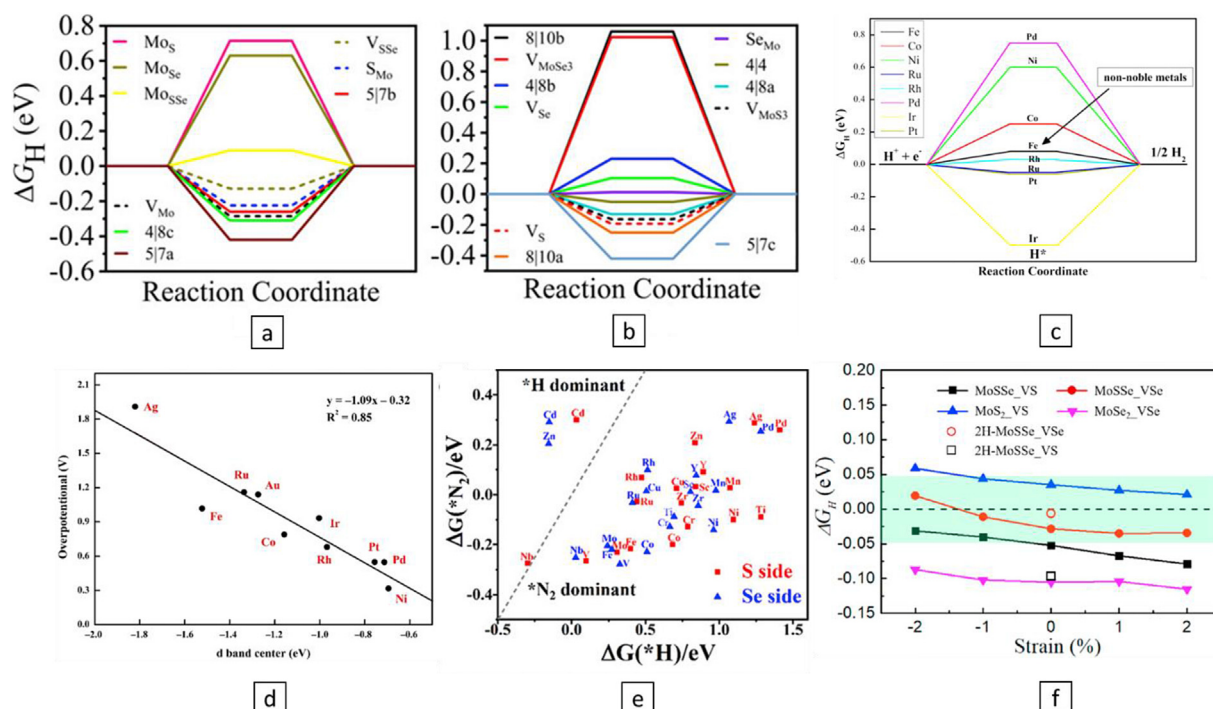


Fig. 16. (a) ΔG diagrams for the H adsorption on Mo atoms [63]; (b) ΔG diagrams for the H adsorption on S/Se atoms [63]; (c) ΔG diagrams for the H adsorption on TM@MoS₂ [64]; (d) Overpotential values for different TM@MoS₂ [64]; (e) The energy required for the formation of ${}^*\text{N}_2$ and ${}^*\text{H}$ was calculated on both S and Se sides without any applied potential. The dashed line represents where the energy required for both is the same. The region where ${}^*\text{N}_2$ is dominant below this line means that forming ${}^*\text{N}_2$ requires less energy than forming ${}^*\text{H}$, which is shown by $\Delta G({}^*\text{N}_2)$ being less than $\Delta G({}^*\text{H})$ [65]; (f) ΔG diagram for 1S-MoS₂ with different vacancies, as a function of strain [66].

performs well in the catalytic region under $-2\%-2\%$ strain, as indicated in Fig. 16 f.

From an application point of view, the use of MoSSe as a catalyst has been described in detail in Section 5.

3.7. Some other unique properties

3.7.1. Out of plane Piezoelectricity

The piezoelectric effect is a phenomenon where electric polarisations and strains interact linearly in insulators and semiconductors that lack inversion symmetry [12,39,67]. This effect has been observed in 2D transition metal dichalcogenides (TMDs) with in-plane piezoelectricity, making them useful in electronic devices, sensors, and energy applications. However, monolayer and multilayer Janus 2D TMDs exhibit out-of-plane piezoelectricity due to their vertical dipole moment, which can be improved through uniaxial or biaxial strain. The vertical piezoelectric coefficient, e_{33} (d_{33}), is found to be larger when the radius difference between the two chalcogenide elements is greater. Piezoresponse force microscopy (PFM, Fig. 17a) has been used to experimentally verify the intrinsic vertical piezoelectricity in a Janus MoSSe monolayer. However, the total vertical piezoelectricity of bilayers is suppressed due to the opposite polarity in two layers [12].

Surface quality and electrical back contacts are improved by directly manufacturing Janus MoSSe on atomically flat conductive substrates. The piezoelectric contrast between the Janus MoSSe monolayer and the substrate is visible, and the signal-to-background ratio is adjusted to reduce electrostatic effects. The contrast is not attributable to topographic, mechanical, or electrochemical artefacts, because a randomised alloy monolayer exhibits no observable contrast under the identical experimental circumstances. (Fig. 17 b-g). The bilayer region exhibits suppressed total piezoelectricity due to the opposite polarity in each layer, highlighting the ‘more is less’ effect (Fig. 17 f) [12]. The piezoresponse force microscopy contrast is caused by piezoelectricity with a structural symmetry origin, and the associated piezoelectric coefficient is around 0.1 p.m. V $^{-1}$, which might be improved by enhancing the dipolar contrast of the chemical bonds. The effective piezoelectricity of semiconducting MoSSe, on the other hand, can be sensitive to fluctuations in electrical characteristics, and the cross-section indicates some non-uniformity of the piezoresponse within the monolayer area [19].

Nevertheless, multilayer Janus 2D TMDs exhibit strong total vertical piezoelectric polarisation under vertical strain, regardless of the stacking

sequence. The out-of-plane piezoelectricity in Janus 2D TMDs provides an additional degree of freedom to design and control their practical applications in nanoelectromechanical devices, energy harvesting, sensors, and more.

3.7.2. Out-of-plane optical dipole transition

Janus MoSSe shows an imbalance of the electronic wavefunction over the S and Se atoms due to asymmetry in chemical bonding within monolayers, resulting in an out-of-plane optical dipole transition. The researchers measured the intrinsic dipole contribution using angle-resolved polarisation-selective second harmonic generation (SHG) measurements and the ratio of the p -polarised SHG signal to the s -polarised SHG signal [12].

The results reveal that the SHG of the Janus sample is greatly affected by the incidence angle, but the SHG of the alloy sample is practically unchanged, proving the presence of an out-of-plane dipole in the MoSSe monolayers (Fig. 18). An angle-dependent SHG model was used to extract the second-order susceptibility associated with the out-of-plane dipole, and the findings demonstrated that the second-order susceptibilities play a role and imply a magnitude ratio of 10:1 at 1080 nm pumping [12]. The study also confirmed the vertical dipole SHG response by measuring multiple samples, and the results showed that the out-of-plane dipole generates observable second-order susceptibilities for all asymmetric samples, whereas the out-of-plane dipole response is almost one order of magnitude smaller and within measurement limits for all randomised samples.

4. Methods to tune the fundamental properties

One of the most intriguing features of MoSSe is its tunability, meaning that its physical properties can be modified by changing its chemical composition, layer thickness, and external stimuli. This tunability enables the tailoring of MoSSe properties for specific applications, such as transistors, photodetectors, and sensors. Researchers have explored various approaches to tune the properties of MoSSe, including chemical doping, defect engineering, strain engineering, and external gating. Understanding the mechanisms and effects of these tunability methods is crucial for further advancing the development of MoSSe-based electronic devices. In this section, we will discuss a few important tuning procedures for MoSSe. In Fig. 19, the importance of tunability is shown using a schematic of a puzzle, where the solved face of the puzzle signifies the

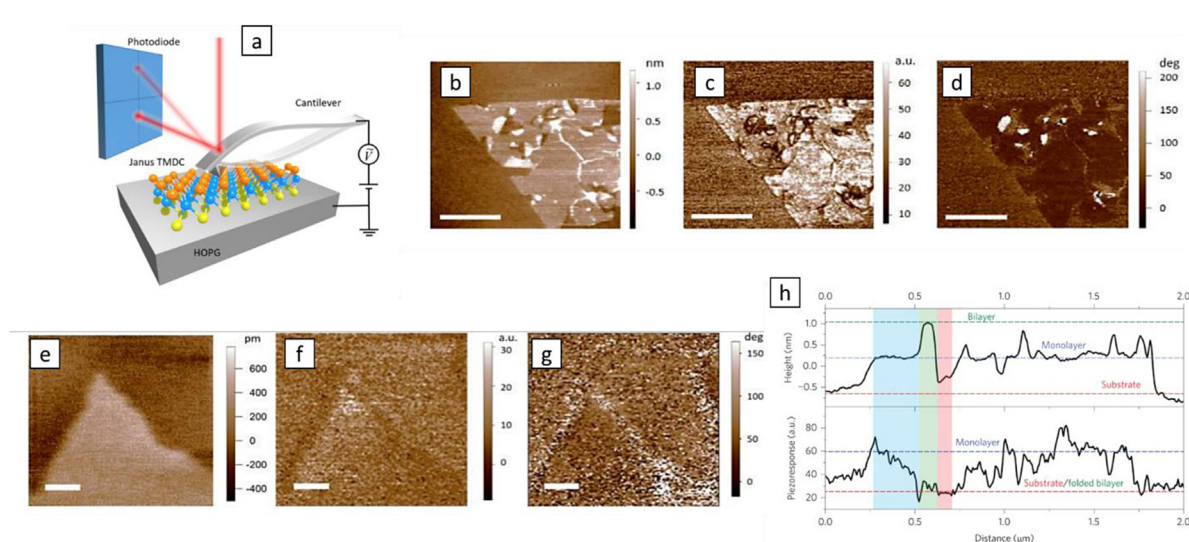


Fig. 17. (a) Schematic of PFM measurement; (b) Topography with PFM for Janus MoSSe; (c) Amplitude with PFM for Janus MoSSe; (d) Phase with PFM for Janus MoSSe; (e) Topography with PFM for randomised MoSSe; (f) Amplitude with PFM for randomised MoSSe; (g) Phase with PFM for randomised MoSSe; (h) PFM response variation with height and different layers [12].

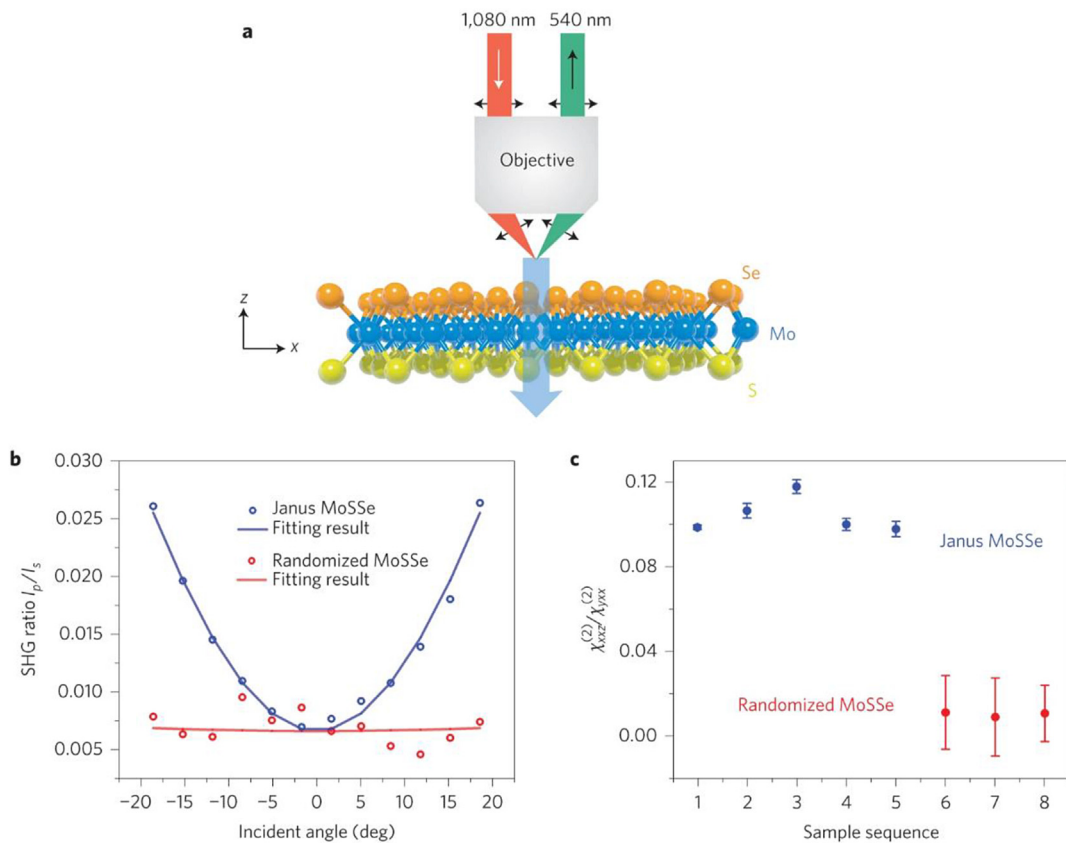


Fig. 18. (a) Schematic of SGH (Red incident beam generates an oscillating vertical electrical field that drives the out-of-plane dipole for SHG. The resulting (green beam) SHG is collected by the same objective and analysed by a polariser; (b) The SHG intensity ratio between p and s polarisation is measured in Janus MoSSe and randomised alloy samples, with different incident angles; (c) The statistics of the second-order susceptibility ratio in Janus MoSSe and MoSSe alloy samples [12].

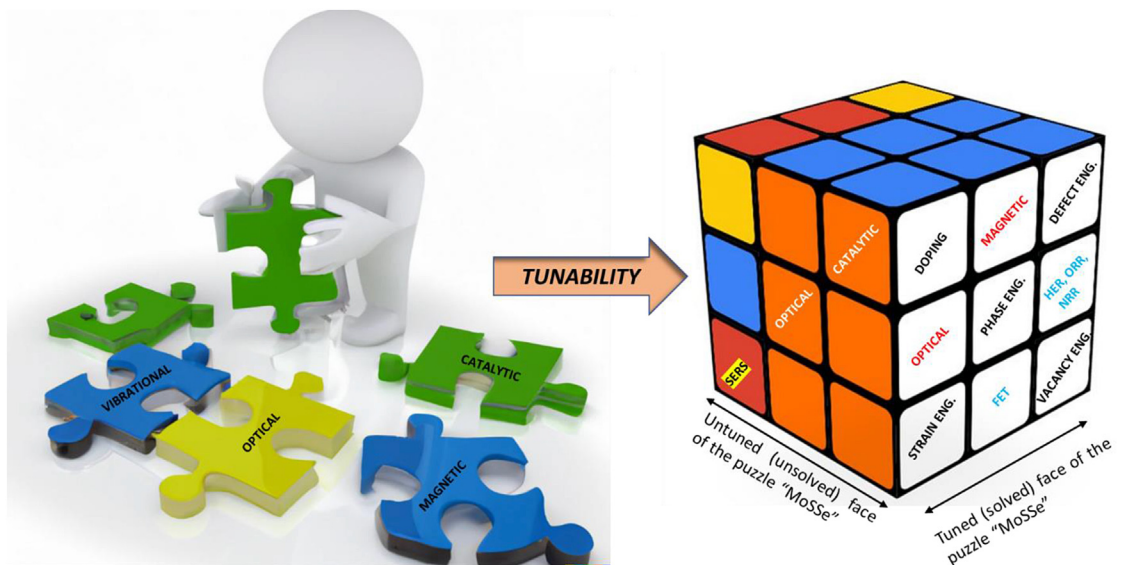


Fig. 19. Tunable properties and tunability methods of MoSSe.

importance of tunability to certain properties that help in obtaining the amplified (or more efficient) results in respective fields of applications.

4.1. Composition modification and phase engineering

The 2D Janus MoSSe and alloys can be modulated by varying their

composition. Since the Janus MoSSe monolayer consists of two distinct phases, adjusting the ratio of S or Se concentration could alter the electronic property or electrical conductivity of the material. In the case of $\text{MoS}(1-x)\text{Sex}$ alloys, property modulation is attainable through stoichiometric alterations, directly influencing their electronic and optical traits. The band gap of $\text{MoS}(1-x)\text{Sex}$ exhibits a nearly linear variation

with composition, facilitating tunable electronic features suitable for applications in electronics and photonics [68]. For example, a $\text{MoS}_{1.5}\text{Se}_{0.5}$ alloy has a fundamental band gap of 2.35 eV and an optical band gap that varies with the temperature, being 1.86 eV at 77K and 1.80 eV at room temperature [69].

Generally, the inherent physical and chemical properties of the 2D TMDCs depend mainly on their phase structure. For practical applications, the phase structure of the materials needs to be regulated. Phase engineering is one of the practical approaches for boosting the electrochemical properties of 2D TMDCs. Phase controlling can enhance conductivity, ion diffusion kinetics, promote electrical conductivity, etc. The phase conversion from 2H to 1T' is broadly investigated in TMDC monolayers to trigger their electronic, catalytic and other material properties. Phase engineering can be achieved by using numerous methodologies like *n*-butyl Li treatment, Alkali metal ion intercalation, hot electron injection, high-temperature calcination and electron beam irradiation. The other methods, like the substitutional method, for example, Mo in MoS_2 is replaced with Re atom and is also used for the phase transition from 2H to 1T'.

Tan et al. [70] proposed a high-yield ultra-sized single layer 1T phase MoSSe nanodots from the 2H phase of the MoSSe monolayer via a combined ball milling and Li intercalation method. The effect of alloying between the S and Se atoms in 1T MoSSe permits an improvement in the catalytic activity for HER reaction in the basal plane compared to that in the 1T MoS_2 . The over-potential obtained was very low, i.e., -140 mV at a current density of 10 mA cm^{-2} and a Tafel slope of 40 mV dec^{-1} . It also demonstrated excellent long-time durability [70]. Wang et al. [50] adopted the electron doping method via a DFT study to induce a transition from the 2H to 1T' of the MoSSe Janus monolayer. The electrons

were introduced into the system with an electron concentration between 0.00 and 1.0e formula unit⁻¹. The electron doping decreased the bandgap of the Janus monolayer from 1.55eV in 2H to 0.15eV in 1T', implying that the conductivity has increased abundantly with the phase transformation. The study suggests that the 1T' phase can supply effective hole injection to 2H MoS_2 for usage in nanoelectronic devices. Yuan et al. [71] investigated the 1T and 2H phases of MoSSe for HER reaction and depicted that in the case of the 1T phase, the higher charge separation leads to better adsorption of hydrogen. T-MoSSe also has a lower Gibbs free energy than the H-MoSSe monolayer, indicating that the former has superior catalytic activity.

4.2. Strain engineering

The impact of biaxial strain on electronic properties is intriguing. The band structure of strained Janus MoSSe is presented in Fig. 20. The bandgap of the direct gap semiconductor Janus MoSSe monolayer can be altered by external factors such as strain engineering or electric field [72]. Biaxial strain ϵ_b significantly changes the band structure of the Janus MoSSe monolayer, transforming it into an indirect gap semiconductor. The bandgap of Janus MoSSe decreases rapidly as the biaxial strain increases, and the monolayer experiences a semiconductor-metal phase transition at a biaxial strain of 12 % [73]. The coupling strengths of orbitals and bond lengths and angles are also altered by biaxial strains (Fig. 20 c). Several theoretical works have reported that the Mo-d, S-p, and Se-p orbitals of the chalcogen atoms play an important role in modulating the band gaps [74]. The tensile strain increases the bond lengths, reducing the $S\text{-M}\text{-Se}$ angle, weakening the coupling between Mo-d_z², Se-p, and S-p orbitals, and strengthening the coupling

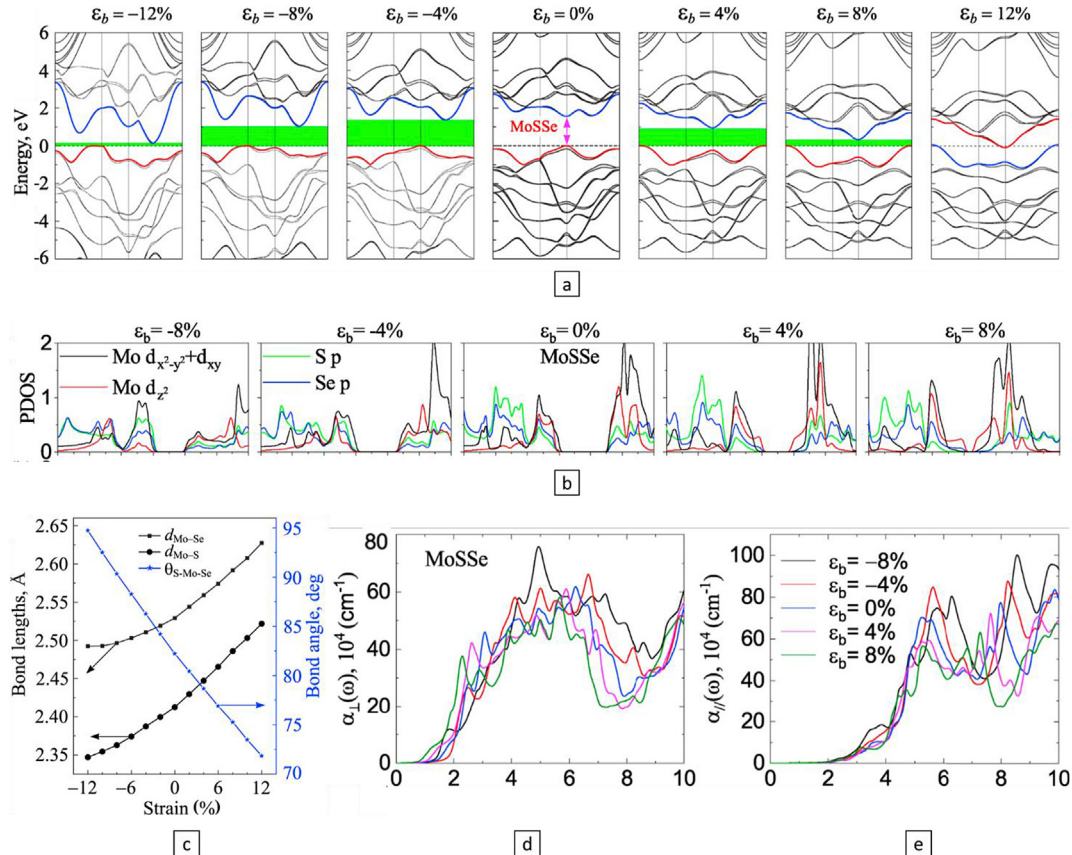


Fig. 20. (a) Band diagrams of MoSSe under variable strain [73]; (b) PDOS structures of MoSSe under variable strain [73]; (c) Variation of bond length and bond angle of MoSSe under variable strain [73]; (d) Variation of the absorption coefficient for perpendicular polarised light of MoSSe under variable strain [73]; (e) Variation of the absorption coefficient for parallel polarised light of MoSSe under variable strain [73].

between the in-plane orbitals, Se-p, and S-p orbitals. In contrast, compressive strain reduces the bond lengths, increasing the S-M-Se bond angle, which strengthens the coupling between Mo-d₂², Se-p, and S-p orbitals and weakens the coupling between the in-plane orbitals, Se-p, and S-p orbitals (Fig. 20 b).

The Janus MoSSe monolayer bandgap and semiconductor-metal phase transition depend on biaxial strain ϵ_b . Apart from the dependence of band gap and metal-semiconductor ratio, The effective masses increase with biaxial compressive strains and decrease slightly with biaxial tensile strains at the K-valley. In the valence band, the effective masses decrease rapidly with increasing tensile strain at the Γ -valley, while the K- Γ -valley masses remain constant [73]. Fluctuations in the effective masses of holes are caused by direct to indirect bandgap transitions under biaxial strains. The strong dependence of electronic properties on applied strain in Janus MoSSe monolayers is similar to TMDs monolayers. Hence, we can say that the Janus MoSSe monolayers exhibit strong electronic properties dependence on the applied strain, which is similar to TMDs monolayers. As a result of all these property alternations, the effect is observed in the optical properties of MoSSe (Fig. 20 d and e). It has been observed the compressive strain improves the absorption coefficient of Janus MoSSe monolayers, but the tensile strain marginally decreases the absorption coefficient [73].

Apart from band structure and optical properties, multiple electronic properties like the Seebeck coefficient, electrical conductivity, and power factor are also sensitive to applied strain on the Janus structure (Fig. 21) [75]. The Seebeck coefficient is a measure of how much voltage is generated by a temperature difference, and it depends on the effective mass of the carriers and the number of band valleys. For the n-type Janus monolayer, the Seebeck coefficient increases under tensile strain and decreases under compressive strain, while the opposite is observed for the p-type monolayer. The electrical conductivity also varies under strain, increasing under compressive strain for n-type monolayer and decreasing under tensile strain for p-type monolayer. The power factor is calculated as the product of the Seebeck coefficient and electrical

conductivity and is found to be maximised under tensile strain for n-type Janus monolayer, while no enhancement in power factor is observed under strain for p-type Janus monolayer. These findings are important in order to tune the electronic properties of the MoSSe for application in various fields [75]. Tang et al. [76] also tuned the MoSSe structure with strain and reported the effect of D-band centring with applied strain that ultimately enhances the catalytic activity of MoSSe for nitrogen fixation (discussed in detail in Section 5).

4.3. Defects and vacancy engineering

The defects and vacancy engineering can alter the local physical properties of the MoSSe material and can have beneficial or adverse effects; it all depends on the intended applications [77]. The defects that can happen naturally during the experimental synthesis include point defects, line defects, grain boundaries, etc. To examine the effect of these defects on the properties, Wen et al. [78] explored the structural and electronic properties of the Janus MoSSe monolayer with point and linear vacancies via the DFT method. The study suggested that the tendency to form the Se vacancy is higher in MoSSe because the interaction between the S and Mo atoms in MoSSe is much stronger than between the Se and Mo. As the number of Se vacancies increases, the band gap of the MoSSe monolayer diminishes significantly, but the semiconducting nature persists, and the observed band gaps are indirect [78]. The values are indicated in Table 3, and the configurations are shown in Fig. 22.

Another DFT study by Shi et al. [63] predicted that inherent defects, such as PDs and GBs, could be easily formed on the Janus MoSSe, showing an enhanced H adsorption for HERs than its pristine counterparts. Similarly, Zhao et al. [81] showed that the S or Se vacancies produce the defect states in the monolayer, which can expand the sunlight absorption limit of Janus MoSSe to 1.3–1.5eV [63]. Additionally, the S vacancy increments the adsorption coefficient by filling valleys in the absorption spectra. The energy range of the enhanced absorption coefficient lies between 1.5eV and 3eV, which is the higher-powered sunlight

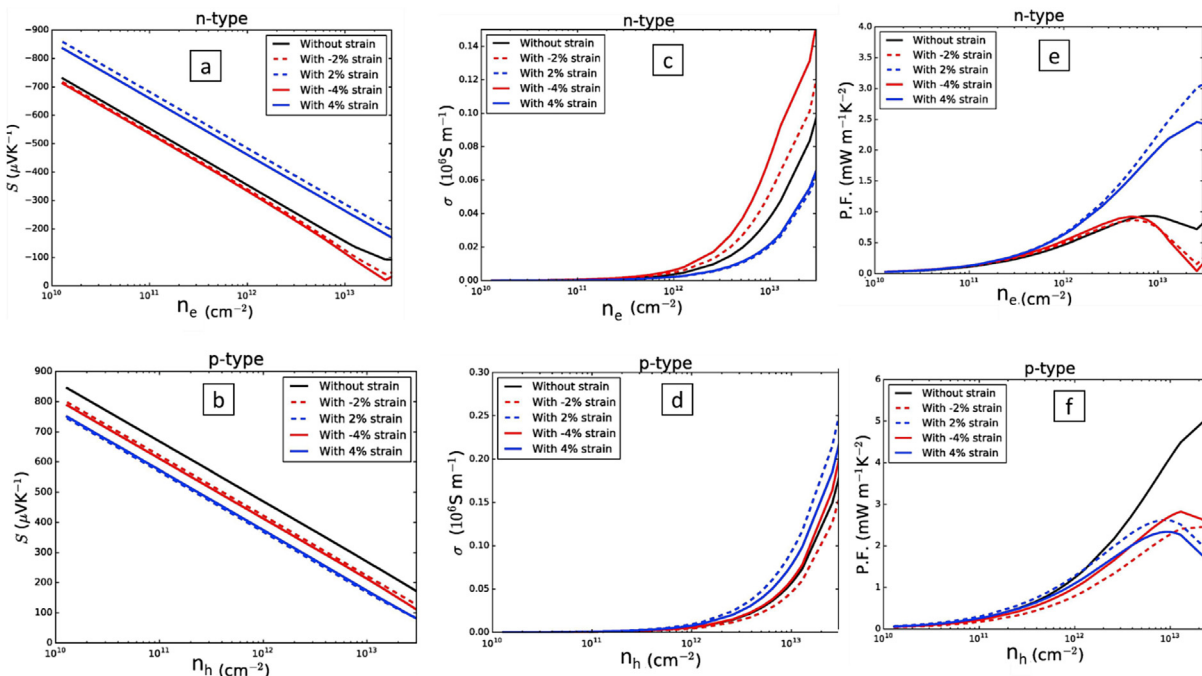


Fig. 21. (a, b) Variation of Seebeck coefficient of MoSSe with strain; (c, d) Variation of electrical conductivity of MoSSe with strain; (e, f) Variation of power factor of MoSSe with strain [75].

Table 3

The calculated values of vacancy energy, formation energy, and associated band gap values (adapted from Ref. [78]).

Configuration	Formation Energy	Energy of the vacancy	Band gap (eV)
Perfect MoSSe	–	–	1.56 eV (Direct)
V(Mo)	6.378	−499.903	–
V(S)	1.712	−508.422	–
V(Se)	1.362	−509.519	1.080 (Indirect)
V(SeSe)	1.252	−509.519	0.874 (Indirect)
V(SeSe + Se (2))	1.312	−503.708	0.765 (Indirect)
V(SeSe + Se (2) + Se (3))	1.333	−497.876	0.675 (Indirect)

energy regime; therefore, these can suit the photocatalytic water splitting application [81]. Similarly, the first principles studies have been conducted by Xu et al. [79] to analyse the influence of intrinsic defects such as S vacancy, Mo antisite, and Mo interstitial defects of MoSSe sheets for water adsorption and conversion. The water adsorption was significant with the Mo interstitial and antisite defects. In addition, these defects could considerably reduce the energy barrier for water splitting, whereas the formation of dissociated water molecules is not possible in pristine MoSSe [79]. The impact of PDs like Vs, VSe, VMoS3, and VMoSe3, on the excitonic properties of the Janus MoSSe material, was examined theoretically by Long et al. [80]. According to their results, the defect induction reduced the bandgap and, thereby, amplifying the light absorption ability in the high wavelength region. The Vs and VSe defects could improve the luminous efficiency as the first bright excitons seem to be firmly bound at these sites with a small exciton radius and greater

binding energy (Fig. 13 d-g). This is due to the fact that the charge of the Mo atom gets redistributed at the chalcogen vacancy sites, which leads to the capture and formation of bound excitons. Therefore, the MoSSe with VS and VSe defects makes it easier to develop new, highly effective quantum emitters. Whereas in the VMoS3, and VMoSe3, the exciton binding energies are equivalent to the pristine MoSSe, due to a competing mechanism between defect and Coulomb screening effect. In conclusion, defect engineering in the structure might successfully be used to modify the important features of the MoSSe.

4.4. Doping

To manufacture transistors and p-n junctions with consistent electrical properties, or to minimize the negative effects of Schottky barriers at metal-semiconductor interfaces, it is essential to achieve precise control over charge-carrier type and doping level in TMDs. However, traditional doping methods such as ion implantation and dopant diffusion can cause significant damage to the structure and electronic properties of these ultrathin crystals, making them unsuitable for such purposes. Therefore, alternative techniques must be explored to achieve this goal. Noncovalent molecular adsorption on 2D semiconductor surfaces has emerged as a promising approach due to its effectiveness and safety. Many molecular approaches based on noncovalent interactions between molecules and TMDs have been reported in recent years.

Zeng et al. [82] investigated the effect of doping tetrathiafulvalene (TTF) and tetracyanoquinodimethane (TCNQ), as these materials are well-studied in literature as carriers. The results reveal that the noncovalent molecular adsorption of TTF or TCNQ on the MoSSe monolayer can cause a typical n-type or p-type doping effect, introducing a donor state or an acceptor state into the band structure of MoSSe. The carrier doping concentration caused by molecular adsorption is found to be

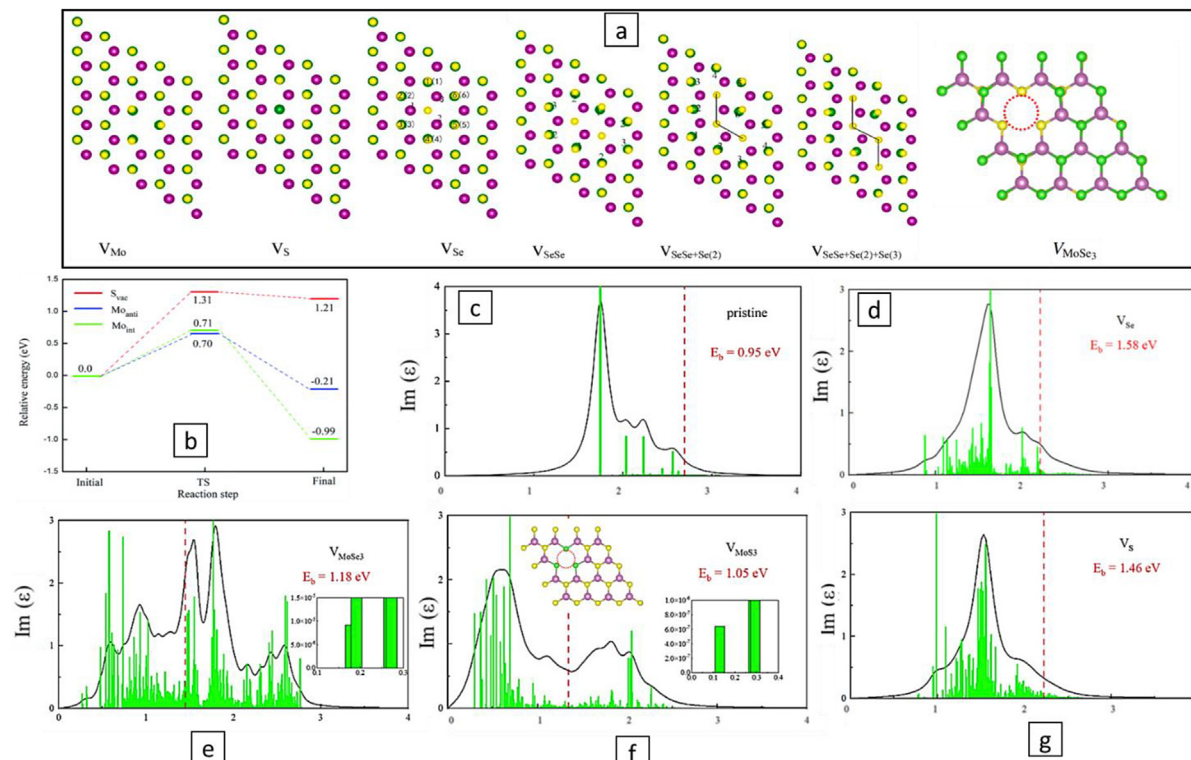


Fig. 22. (a) Structural configuration of possible vacancies [78]; (b) Reaction path of molecular H₂O splitting via transition step in different intrinsic defect configuration of MoSSe [79]; (c-g) The dielectric function of pristine MoSSe (c), V_{Se} (d), V_{MoSe3} (e), VMoS3 (f), and V_S (g) (Vertical dashed lines indicate the GW band gaps for the initial brilliant exciton. The optical oscillator strengths of the constituent excitonic and band transitions are shown by green bars. Insets depict the energy area surrounding the dark excitonic peaks.) [80].

significantly dependent on the MoSSe side (TTF prefers the S side with an adsorption energy of 0.82 eV, whereas TCNQ prefers Se side with an adsorption energy of 0.85 eV). Since the electronegativity of S (2.58) is higher than that of Se (2.55), the S atoms in MoSSe contain more electrons than the Se atoms. As a result, electron acceptors tend to interact more strongly with the S plane, while electron donors prefer the Se plane [83]. Furthermore, it is possible to flexibly control the molecular adsorption-induced n-type or p-type doping effect using biaxial strain or by applying an external electric field. These findings could pave the way for developing innovative nanodevices based on Janus MoSSe, such as FETs or sensors.

On a similar study by Cui et al. [84] suggests that p-doped Janus MoSSe can be obtained by molecular doping using TCNQ and tetracyanoethylene (TCNE), whereas n-doped Janus MoSSe can be achieved through doping with TTF. TTF acts as a potent electron contributor as each molecule contains four sulfur atoms that are rich in electrons. Conversely, TCNE and TCNQ function as powerful electron acceptors due to the presence of four cyano groups in each molecule. It's worth noting that a dipole moment is created between Janus MoSSe and the organic molecule, which can significantly alter the work function values of Janus MoSSe within the range of 3.76 eV–6.17 eV, which demonstrates the potential for organic molecules adsorption in MoSSe-based semiconductor nanoelectronic devices. Additionally, when different organic molecules are adsorbed, an impurity band appears near the Fermi level in the band structures of Janus MoSSe, indicating that the electron is more likely to transition (Fig. 23). LUMO of TCNQ and TCNE is located above the Fermi level that acts as acceptor level (p-type behaviour) and the HOMO of TTF is located just below the Fermi level that can act as donor level (n-type behaviour). According to Bader charge analysis, 0.805 and 0.117 electrons are transported from the Janus MoSSe layer to TCNQ molecules, which is less than the 0.031 and 0.172 electrons transferred from the Janus MoSSe layer to TCNE molecules adsorbed on Janus MoSSe [84]. The charge distributions for TTF adsorption are mostly between the TTF molecules and the under-coordinated S (Se) atoms. According to Bader charge analysis, 0.207 and 0.135 electrons are transported from the Janus MoSSe layer to TTF molecules, indicating a significant charge transfer from TTF molecules to the Janus MoSSe layer [84]. Moreover, organic molecule adsorption on Janus MoSSe can significantly widen its optical absorption spectrum in the visible light range. This study provides a theoretical foundation for the development of Janus MoSSe-based photovoltaic nanodevices.

Zhao et al. [85] also discussed about the benefits of cooping of heteroatoms like N + P or N + F for efficient photocatalytic splitting of water. The results show that the N + F co-doped mono layer MoSSe has relatively higher thermodynamic stability and reduced direct band gaps,

ranging from 1.28 to 1.57 eV [85]. The band edge position of the doped material satisfies the redox potential requirement of water at pH = 0 under an intrinsic polarised electric field. The doped N sites exhibit strong photocatalytic activity for the hydrogen reduction reaction (HER). Their findings suggest that N + F co-doped MoSSe has potential as a promising photocatalyst, with high catalytic activity for HER and the ability to facilitate the separation of photogenerated carriers through the intrinsic polarised electric field [85]. This study provides a way to screen for MoSSe-based photocatalysts. In detail this has been described in Section 5.

Do et al. [57] reported, doping one La and Ce element onto one S or Se side of a Janus MoSSe monolayer reduces the band gap and shifts it from direct to indirect. The Janus MoSSe monolayer transforms from a semiconductor to a metal when the La and Ce doping concentrations grow. All La and Ce-doped, Janus MoSSe systems, have lower effective masses than the pristine state, resulting in significant carrier mobility. Moreover, all La and Ce-doped MoSSe systems absorb visible and infrared light with a red shift, showing strong absorption in these ranges. Their findings imply that rare-earth La and Ce-doped MoSSe monolayers might be suitable for spintronics, nanoelectronics, and optoelectronics (discussed in detail in Section 3). Also, the effect of doping transition materials on the magnetic properties of MoSSe has already been discussed in Section 3.

In addition to the strategies mentioned above, multiple other options can tune the properties of MoSSe, like hybridisation or heterojunction of MoSSe with different other materials. Creating van der Waals (vdW) heterostructures involving Janus MoSSe and other 2D materials can yield extraordinary properties. For instance, when the Janus MoSSe/ZnO vdW heterojunction is formed, a type-II band arrangement occurs, mainly when the sulfur atoms of MoSSe interact with ZnO [86]. Similarly, band alignments are achieved in Janus MoSSe/GaN heterosystems [87]. Additionally, the formation of heterojunctions between Janus MoSSe and MoGeSiN₄ has demonstrated a notable photocatalytic conversion efficiency of 26.4 %, making it highly suitable for applications in photovoltaics and photocatalysis [88].

5. Applications of 2D Janus MoSSe and alloys

5.1. Chemical and gas sensors

Transition metal-based dichalcogenide materials have recently been considered suitable for chemical and gas sensors due to their controllable structural and tunable band gap and carrier mobility. Through adsorbed molecules that act as charge acceptors or donors, experiments have shown that layered MoS₂-based FETs are quite sensitive to various gas molecules. MoS₂ is a superior gas sensor with higher sensitivity and

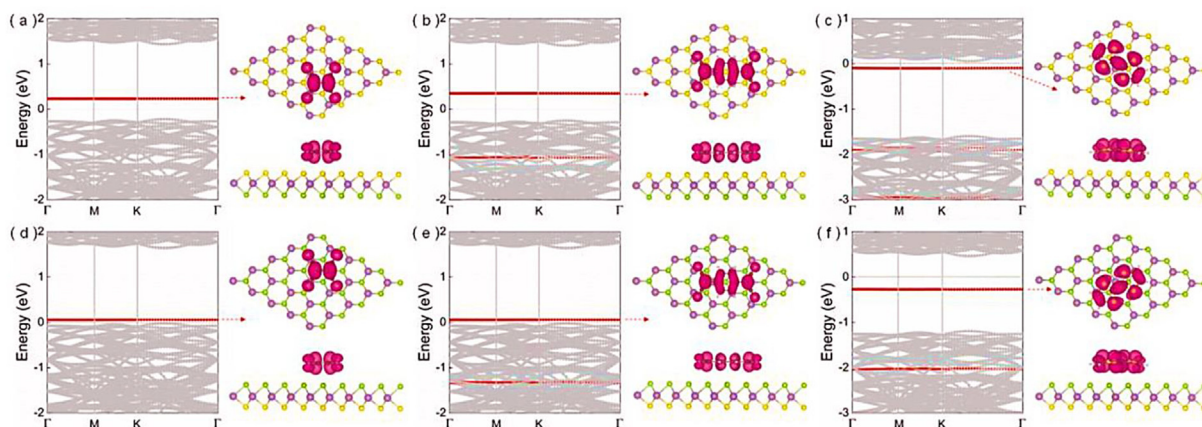


Fig. 23. TCNE, TCNQ, and TTF adsorbed on the S-layer (a–c) and Se-layer (d–f) [84].

selectivity compared to graphene and other TMD materials because of its exceptional qualities, including high surface-to-volume ratio, selective reactivity upon exposure to various analytes, rapid response, and recovery. Since the band gap and transport properties of MoS₂ are controllable with exposure to light or gate bias, the sensing performance can be greatly improved.

However, applying an external electric field and precisely controlling the adsorption behaviour at the nanoscale remain formidable challenges. A material with a controllable intrinsic electric field is highly favoured for extremely high sensing performance because it increases sensitivity. One of the promising candidates is the recently synthesised Janus monolayer MoSSe.

Jin et al. [89] reported the sensitivity of CO, CO₂, NH₃, NO and NO₂ on Janus monolayer MoSSe using first principle calculation. Their analysis shows that CO and CO₂ gases are rather bonded weakly at a larger distance compared to NH₃, NO and NO₂ gases, which are bonded more strongly at a nearby distance that initiates chemical interaction between the gas molecules and MoSSe layer [89]. Similarly, more negative adsorption energy values were obtained in N-containing gases, except NO, than C based gases indicating stronger bonding (Fig. 24a). The adsorption energy was calculated using the formula:

$$E_{\text{adsorption}} = \frac{E_{\text{host}+nM} - E_{\text{host}} - nE_M}{n} \quad (1)$$

In order to get more details, Bader charge analysis was performed where the gain in charge of the adsorbed gas molecules from (to) these layers is represented by the positive value of charge transfer, and the loss of charge of the adsorbed molecules to the layers is represented by negative values (Fig. 24 b). The charge distribution is calculated using the formula:

$$\Delta\rho = \rho_{\text{total}}(r) - \rho_{\text{substrate}}(r) - \rho_{\text{molecule}}(r) \quad (2)$$

The minor charge distribution in C-based gases confirms the weak interaction claimed previously, whereas the large charge distribution of NH₃ and NO₂ indicates better sensitivity, NO₂ being the most sensitive one with a charge transfer of 0.102e on the Se side [89]. While the NH₃

molecule behaves as a charge donor to the Se or S side of the monolayer, CO, CO₂ and NO₂ on the MoSSe act as charge acceptors. In particular, NO functions as a donor on the S side but an acceptor on the Se side; despite the extremely small number of electrons transferred, the NO gas molecule exhibits remarkable electron redistribution. As a result, NO's adsorption energy on MoSSe is also very low [89].

Taufik et al. [90] reported an improved NO detection technique at room temperature using Mo_{2-x}Se_x samples with different selenium contents ($x = 0, 0.2, 1, 1.8$, and 2) using both experimental and DFT analysis. A hydrothermal reaction (Fig. 24 c) and post-annealing modification were used to synthesise the Mo_{2-x}Se_x nanoparticles. Se addition has been used to successfully alter the morphology of MoS₂. Due to the larger atomic size after Se addition, MoS₂'s crystal lattice was expanded and the particle size of MoS₂ size has changed from a micrometre scale to a nanometer scale, keeping the crystal structure intact (Fig. 24 d). The effectiveness of NO detection is enhanced by these two changes. The highest specific surface area, small particle size, and good charge transfer ability and stability of the annealed sample, with $x = 1$, led to the best NO detection performance, which was demonstrated by DFT calculations. The addition of Se results in a decreasing band gap and increasing conductivity, which is further increased upon the addition of NO as it acts as a donor atom to the MoSSe surface. This increase in conductivity in presence of NO is measured in order to detect the presence of this gas. The sensitivity of the gas is calculated to be 48 %, and the performance is found stable even in humid conditions as an added advantage [90].

The gas sensing ability can further be improved by tailoring some properties (vacancy engineering, doping etc.) of Janus MoSSe. Chaurasiya et al. [91] reported vacancy engineered Janus type MoSSe material using DFT analysis for the application of NH₃, H₂S, NO and NO₂ sensing. In the Janus MoSSe monolayer, three different vacancy defect types—Moy, Se_y, and (S/Se)_y defects—are taken into account. All the results are tabulated in Table S2 [91].

Chen et al. [92] examined the effect of doping on MoSSe using first principle calculations for the gas sensing application, and they reported their analysis based on the sensing performance of Cl₂, H₂S and SO₂. Initial research showed C doping ($E_{\text{binding}} = -7.32$ eV on both S and Se

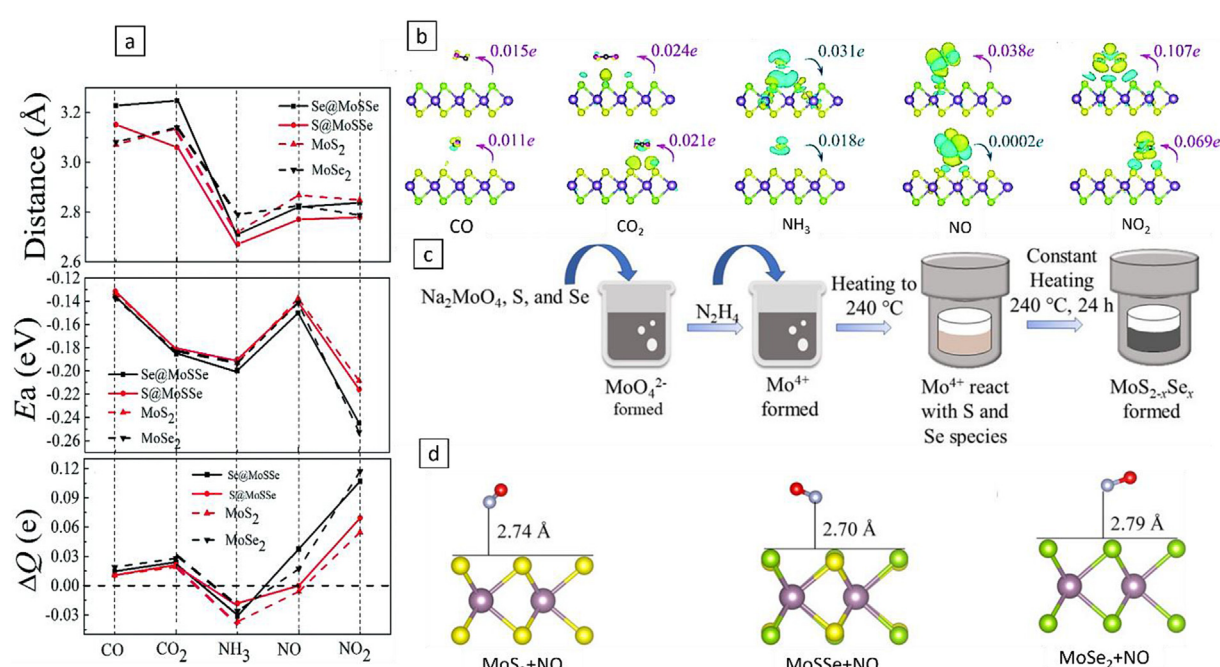


Fig. 24. (a) Performance comparison on Janus MoSSe for the application of gas (CO, CO₂, NH₃, NO, and NO₂) sensing [89]; (b) Bader charge analysis of Janus MoSSe for the application of gas (CO, CO₂, NH₃, NO, and NO₂) sensing [89]; (c) Synthesis of Mo_{2-x}Se_x for the application of NO detection [90]; (d) DFT analysis of Mo_{2-x}Se_x for the application of NO detection [90].

sites and corrected up to 2 decimal places) on MoSSe is favourable with higher negative binding energy in comparison with B doping ($E_{\text{binding}} = -5.67 \text{ eV}$ on both S and Se site and corrected up to 2 decimal places), and P doping ($E_{\text{binding}} = -4.90 \text{ eV}$ on both S and Se site and corrected up to 2 decimal places) (Fig. 25 a). The DOS analysis also favours the doping of C on MoSSe, and hence, further research has been continued by Chen et al. [87] on C-doped MoSSe. These results are reported in Table S2. From the result, we can see that the adsorption on the S site is more favourable than adsorption on the Se site; also, we see that the doped structure has better sensitivity in terms of adsorption energy calculation and charge distribution calculation. The band gap of pristine MoSSe-C is calculated as 0.86 eV, whereas the change in the band gap of different values for different adsorbed gases (Fig. 25 b). This factor is used for selective sensing of gases using MoSSe-C [92].

Recently, Yang et al. [89] reported the application of MoSSe alloys in order to sense the decomposed products of SF₆ (H₂S, SO₂, SOF₂ and SO₂F₂), which is widely used in switchgear of daily used electrical systems. Their result shows the order of sensitivity is SO₂ > SO₂F₂ > H₂S > SOF₂ [93]. As a part of their detailed investigation, they examine all possible sites for adsorption, and those are.

- top of S: T(S)
- top of Se: T (Se)
- top of Mo on S layer: T (Mo-S)
- top of Mo on Se layer: T (Mo-S)
- hollow side of hexagon ring on S layer: H(S)
- hollow side of hexagon ring on Se layer: H(Se)
- vacancy on S layer: V(S)
- vacancy on Se layer: V(Se)

Their analysis has been reported in detail in Table S3 and Fig. 25 c.

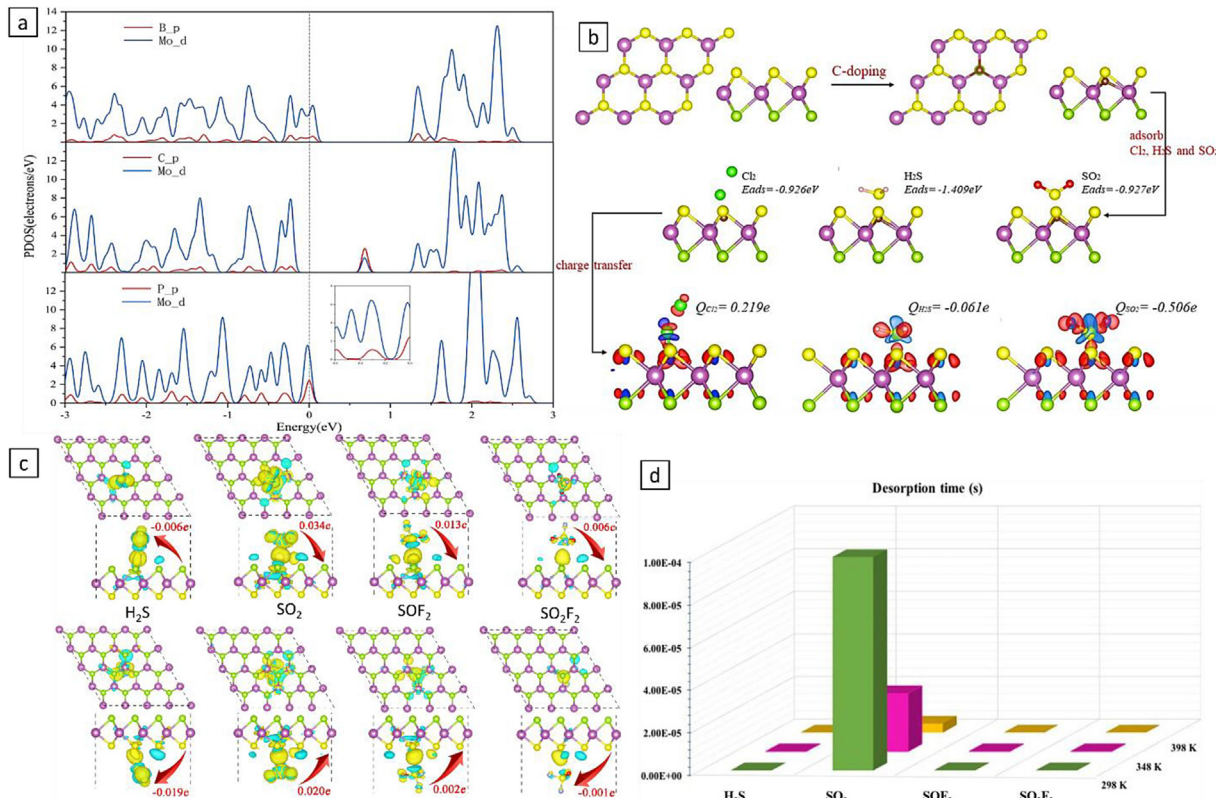


Fig. 25. (a) Suitable doping material search using DOS analysis on MoSSe surface [92]; (b) Gas sensing mechanism and parameter on C doped MoSSe for the sensing application of Cl₂, H₂S, and SO₂ [92]; (c) Bader charge analysis of decomposed products of SF₆ (H₂S, SO₂, SOF₂, and SO₂F₂) on MoSSe surface [93]; (d) Response time of decomposed products of SF₆ (H₂S, SO₂, SOF₂, and SO₂F₂) on MoSSe surface [93].

Their analysis is very much in detail and orientation specific to the adsorbed gases. P stands for parallel to the MoSSe surface, and V stands for vertical with the MoSSe surface. Bader charge analysis reveals that H₂S acts as a charge acceptor from the MoSSe surface, whereas the other gas molecules act as charge donors (Fig. 25 c). The highest charge redistribution is observed in the case of SO₂, which justifies the high sensitivity towards this gas, as we mentioned above [93]. Also, for practical feasibility, they have investigated the desorption time of each gas at various temperatures, using the equation

$$\tau = \frac{1}{A} e^{\frac{E_a}{k_B T}} \quad (3)$$

Where A , the apparent frequency factor is taken as 10E12 s⁻¹, E_a is activation energy, k_B is Boltzmann constant, T is temperature. It is found that the desorption time of SO₂ is higher compared to other gases, but at high temperatures, the desorption time is suitable for applications (Fig. 25 d). The high extent of interaction with the MoSSe layer can be the cause of the delayed desorption [93].

In this section, we have detailed the investigation of the complex interaction mechanisms between gas molecules and MoSSe surfaces using a combination of computational modeling tools, such as first-principles calculations and density functional theory, as well as experimental investigations. Structural alterations, such as doping with other elements like carbon and creating vacancies, have been investigated to improve sensitivity and adapt the material's reaction to specific gases. Furthermore, application-specific investigations have revealed the potential of MoSSe-based materials in a variety of gas sensing scenarios, including NO detection at room temperature and the detection of degraded sulfur hexafluoride (SF₆). Collectively, these efforts demonstrate MoSSe and its variations' adaptability and potential future in gas

sensing technology for a wide range of industrial and environmental monitoring applications.

5.2. Surface-enhanced Raman spectroscopy (SERS)

Over the past few decades, Surface-Enhanced Raman Scattering (SERS) has received extensive research attention for both basic studies of light-matter interactions and applications of selective and sensitive analytical methods. In order to improve the applicability of SERS it is very necessary to understand the mechanism. In literature, electromagnetic mechanisms and chemical mechanisms are renowned. The electromagnetic mechanism deals with light-matter interaction that modulates the electromagnetic field, whereas the chemical mechanism mainly manipulates the dipole interactions and charge transfer. Although the superiority of SERS is well established, the mechanisms are not, and hence, the research continues.

Recently, in 2022, Jia et al. [90] reported the enhanced Raman activity of 105 orders of Janus MoSSe molecules for the first time. Due to the asymmetric structure of the monolayer S–Mo–Se and the difference in electronegativities of the top S and bottom Se atoms, dipoles aligned along the out-of-plane direction were produced. According to the literature, the out-of-plane dipoles are extremely SERS active. In monolayer MoSSe, the out-of-plane dipole moment was as high as +0.33 e Å [94]. These oriented dipoles in Janus MoSSe extend to engage in direct interaction with the nearby dipoles in the adsorbates. Jia et al. [94] continued their further studies using glucose as the adsorbed molecule. In comparison with MoS₂ and MoSe₂, only MoSSe molecules provided strong enhanced Raman peaks depending on the level of interaction, proving its possible SERS activities upon the addition of glucose. The enhanced peaks are shown in Fig. 26 a, and a differential convolution with pristine substrate is also provided in Fig. 26 b to show the enhancement clearly.

The peak corresponding to C–C stretching at ~1360 cm⁻¹ has been found to be the strongest peak, and hence, it is used as an indicator for

further study. The SERS analysis is performed at different concentrations of glucose in order to observe its selectivity. The results are shown in (Fig. 26c and d). But at higher concentrations, the characteristic peaks of glucose adsorbed on MoSSe (772 cm⁻¹, 928 cm⁻¹, 993 cm⁻¹, 1180 cm⁻¹, 1311 cm⁻¹ and 1360 cm⁻¹) are found to deviate from their positions, and the cause is attributed to the absorption of glucose on MoSSe monolayers at high concentrations, which alters the dipole interactions [94]. DFT analysis on glucose-adsorbed MoSSe nullified the effect of charge transfer to enhance the Raman effect due to high charge barriers between the MoSSe valence band to LUMO of glucose and MoSSe conduction band to HOMO of glucose (Fig. 26 e). It also calculated the redistribution of charge and dipole moment, which showed the change in dipole moment of glucose after addition on MoSSe was -0.05 e Å to 0.23 e Å, which is significantly high (Fig. 26 f).

5.3. Photodetectors

Tunable Fermi level and band gap are the key properties that have attracted the 2-dimensional material research for the application of optoelectronic devices.

Zhang et al. [95] reported the synthesis and application of MoS_{2(1-x)Se_{2x}} monolayers using confined spaced CVD (Fig. 27 a) and analysed the effect optimized of H₂/Ar as the carrier gas concentration for its application for optoelectronic devices. Morphological analysis (Fig. 27 b) shows with increased H₂ %, the average size (Fig. 27 c) of the triangular nanoflakes increases up to a limit and then decreases, as it is also reported that excess H₂ concentration causes etching in the as formed nanoflakes. As a result, 15 % H₂ was found to be the optimum concentration with an average nanoflake size of 200 μm and a maximum of 400 μm. The photoresponse is noted at various values of 2x (2x = 1, 0.94, 1.34, 2) (Fig. 27 d) [95]. The results show at x = 1, the photoresponse time is below 30 m s which is very much suitable for practical application. This performance enhancement is mainly attributed to the reduced band gap in the Se-substituted MoS₂ compound. PL spectra

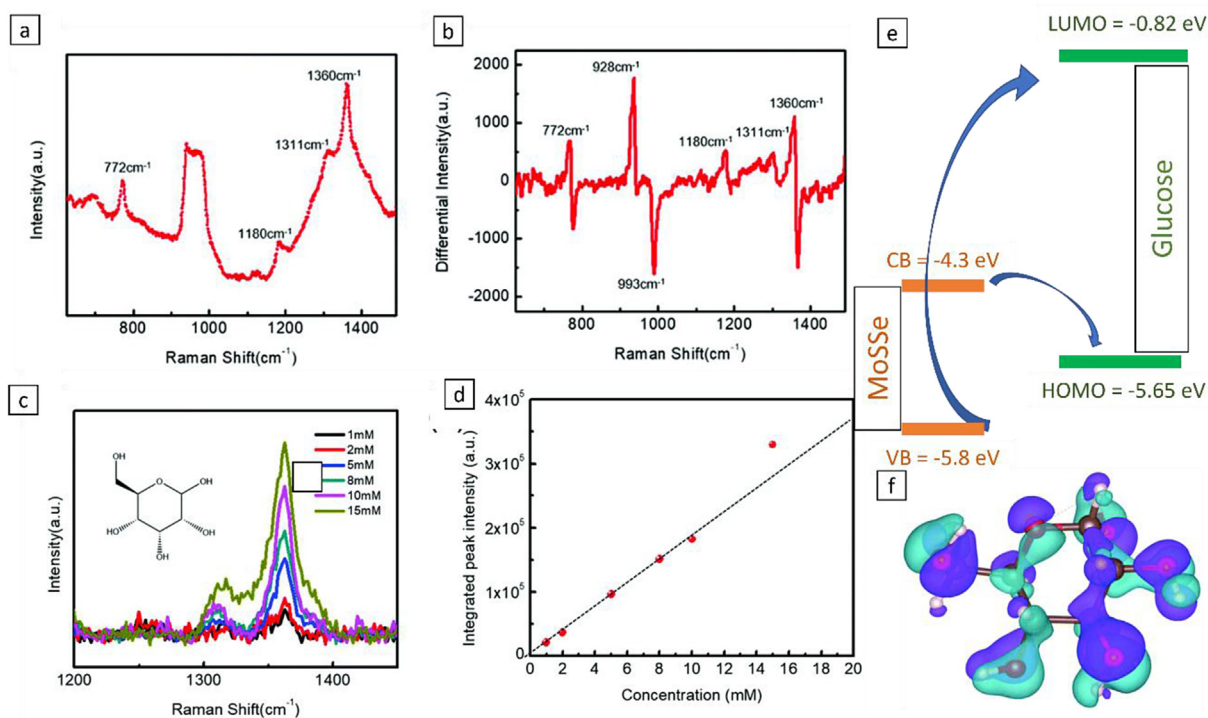


Fig. 26. (a) Enhanced Raman peaks in glucose-doped MoSSe [94]; (b) Differential Raman peak analysis of glucose-doped MoSSe with pristine glucose [94]; (c, d) Enhanced peak intensity in glucose-doped MoSSe depending on various glucose concentrations [94]; (e) Energy band diagram of glucose-doped MoSSe [94]; (f) Charge distribution curve in glucose-doped MoSSe (purple denotes electron cloud of Janus MoSSe, light blue electron density denotes charge cloud of glucose) [94].

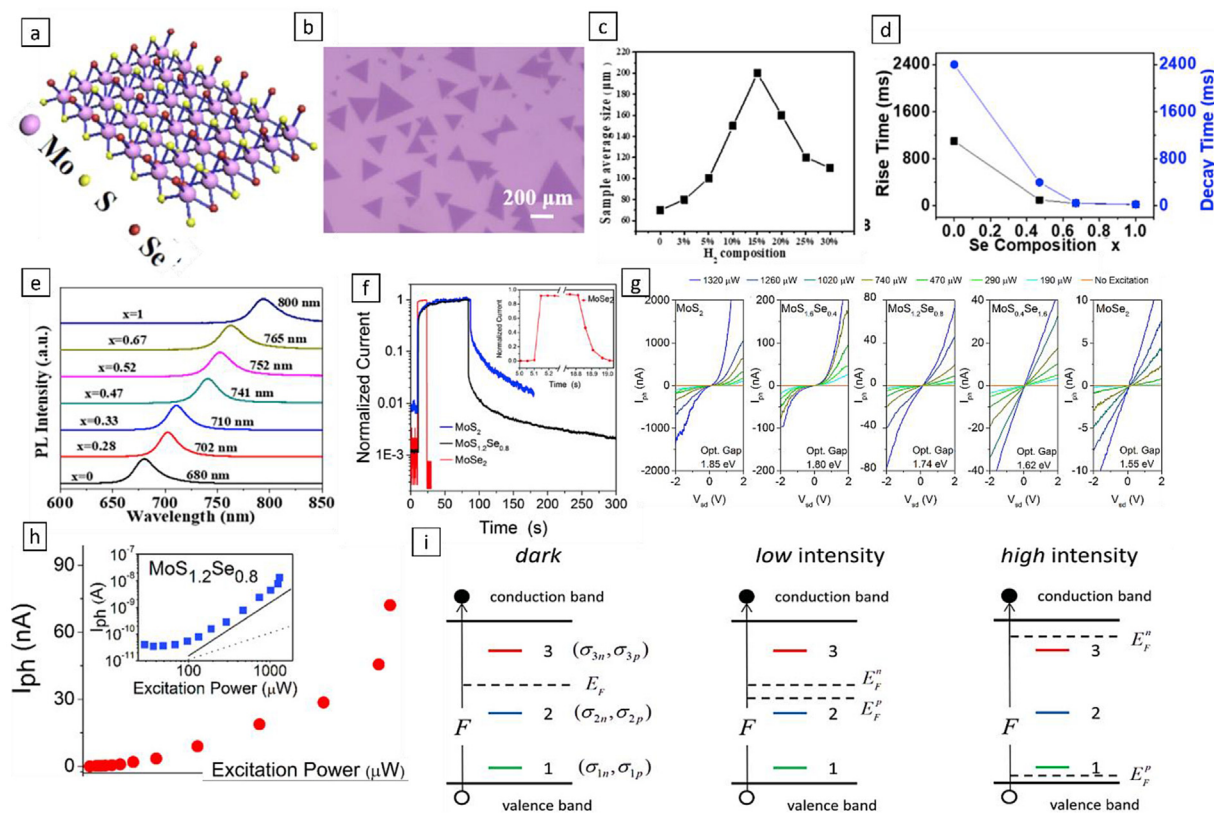


Fig. 27. (a) Structure of MoS_{2(1-x)Se_{2x}} type alloys synthesised using confined CVD synthesis method [95]; (b) SEM image of MoS_{2(1-x)Se_{2x}} type alloys synthesised using confined CVD synthesis method at 15 % H₂ content [95]; (c) Sample size distribution in MoS_{2(1-x)Se_{2x}} type alloys synthesised using confined CVD synthesis method at different H₂ concentration [95]; (d) Photo response time curves of MoS_{2(1-x)Se_{2x}} type alloys synthesised using confined CVD synthesis method at different values of x [95]; (e) PL spectra analysis of MoS_{2(1-x)Se_{2x}} type alloys synthesised using confined CVD synthesis method [95]; (f) The photoreponse curves of CVD grown MoS_{2(1-x)Se_{2x}} type alloys [96]; (g) I-V characteristic of MoS_{2(1-x)Se_{2x}} type alloys at different applied power and different values of x [96]; (h) Super linear behaviour photo current with power intensity of CVD grown MoS_{2(1-x)Se_{2x}} type alloys [96]; (i) Model to explain super linear behaviour of photo current with power intensity of CVD grown MoS_{2(1-x)Se_{2x}} type alloys [96].

analysis shows (Fig. 27 e) a continuous decrease in band gap with Se substitution at different concentrations. The lower electronegativity of Se compared to S strengthens the bonding between Mo and Se compared to Mo and S, and thus, the fully occupied d_z² band keeps broadening with an increase in Se concentration; as a result, the direct band gap is decreased in the system as reported [MoS₂ = 1.82 eV, MoSe₂ = 1.55 eV] [95].

Klee et al. [92] investigated the dependence of photocurrent on laser power, using CVD-grown MoS_{2(1-x)Se_{2x}} type alloys in order to be able to tune the existing optoelectronic devices as per requirement. Similar to the work of Zhang et al. [91], in this work also, a linear decrease in bandgap is observed with the increase in Se content. The experimental evidence shows.

- Decrease in photocurrent with a decrease in S content.
- Increase in photo response time with increase in Se content as an effect of decrease in band gap as discussed above.
- Increase in the linearity of I-V curves with an increase in Se content. The deviation from linearity at high S content can be a result of a high Schottky barrier due to the larger band gap of the system.

Klee et al. [92] reported superlinear dependence of photocurrent at 2 V bias voltage with power intensities, which is a rare find. In general, in photoconductive devices, the dependence of photo-current and power is linear at a low power range and sub-linear at a high power range (Figs. 27 f, 25 g, h). Hence, Klee et al. [96] used a model based on recombination theory in order to describe the superlinearity of the system. According to the literature, the CVD synthesis originated with some defects in the mother material that caused the creation of various internal states. With

increased power, the shift of the quasi-Fermi level modifies the occupancy of the internal states (Fig. 27 i). At high intensity, the empty intergap states are claimed to be filled partially due to available free electrons and holes hence finally reducing the recombination rate and originating superlinearity.

Hou et al. [97] synthesised MoS_{2(1-x)Se_{2x}} ($x = \frac{1}{4}, 0, 0.5, 1$) alloy using a hydrothermal synthesis method, which exhibited a high photocurrent, stable, repeatable response and considerably shorter response time of 4.7 s. This type of material is reported to be responsive in a wide range of 405 nm–808 nm. At zero bias, the photoresponsivity of this device was reported to be 311 mAW⁻¹ [97]. The high photocurrent in MoSSe-type devices reduced the recombination rate, which directly increases the lifetime of the photocarriers. We have already discussed the possible explanation with the model reported by Klee et al. [2]. Xu et al. [98] reported a similar molybdenum sulfo-selenide alloy, synthesised using a controllable chemical solution deposition method that was also responsive in the wide range of 405–808 nm, and the response time was as short as 50 ms [98]. At zero bias, the photoresponsivity of this device was reported to be 311 mAW⁻¹ [98].

5.4. Field emission

Due to their potential uses in nano- and optoelectronics, 2D semiconductors, a new class of materials with atomic thickness but no dangling bonds on their surface, have attracted a great deal of attention [99–101]. Theoretical calculations have suggested that 2D semiconductor alloys can have tunable bandgaps in a broad spectrum, and experiments in transition-metal dichalcogenide monolayer alloys have

supported this claim.

Feng et al. [35] described the application of $\text{MoS}_{2(1-x)}\text{Se}_{2x}$ as FET, which showed n-type behaviour and a high off/on ratio of 10^5 . A mobility of between 0.1 and 0.4 $\text{cm}^2\text{V}^{-1}\text{s}^{-1}$ on average for the $\text{MoS}_{2(1-x)}\text{Se}_{2x}$ monolayer FETs was estimated to have x equal to 0.15 and 0.30, respectively. The mobility has been calculated using the formula:

$$\mu = \frac{dI_{ds}}{dV_{gs}} \cdot \frac{L}{W} \cdot \frac{1}{C_g} \quad (4)$$

Where I_{ds} means source-drain current, V_{gs} is gate-source voltage, L is channel length, W is channel width, and C_g is the gate capacitance. Considerably less mobility for the MoS_2 -monolayer FETs ($0.1 \text{ cm}^2\text{V}^{-1}\text{s}^{-1}$) was obtained, which may be due to much poorer contact (Fig. 28a-f).

Yanase et al. [102] reported a high-pressure annealing technique with a S vapour pressure of 5 atm for treating S vacancies in MoS_2 . By observing the photoluminescence, the crystal quality following mechanical transfer, S annealing, and vacuum annealing was thoroughly investigated. The Raman spectrum (Fig. 28 g) reveals that only the S-Mo modes were visible prior to the Se annealing, while the Se-Mo vibrational modes (A_{1g} and E_{2g}) at 282 and 302 cm^{-1} were observed after the Se annealing. Even after the Se annealing, there were still two MoS_2 peaks at 380 cm^{-1} [E_{2g} (S-Mo)] and 405 cm^{-1} [A_{1g} (S-Mo)]. According to earlier reports, the incorporation of the heavy Se atoms would soften the S-Mo bonding, shifting the peak position of the E_{2g} (S-Mo) vibrational mode to a lower frequency. The band gap becomes narrower as a

result of the alloying with Se, which causes the emission peak from the exciton (XA) to be redshifted. The Se molar fraction was calculated from the emission peak's centre to be around 10 %. Because the introduction of Se atoms quenches the PL (Fig. 28 h), the lack of PL recovery did not imply that there were many S vacancies left (poor crystal quality). This defect modification improves mainly the tunability of the system as well as enhances the performance and decreases additional losses, which ultimately increases the efficiency of the system [102].

5.5. Energy storage applications

5.5.1. Supercapacitors

The metallic conductivity of group VI transition metal dichalcogenides and the enhanced electronic structure and physicochemical properties of mixed dichalcogenides over pristine materials are the basis of the investigation of supercapacitive behaviour of MoSSe type materials. Sellam et al. [103] reported the performance of the 1T phase of the molybdenum sulfoselenides in different ratios of S and Se [$\text{MoS}_{2x}\text{Se}_{2(1-x)}$ (where $x = 0-1$)]. They reported solid-state synthesis (Fig. 29 a) at high temperatures and characterised the synthesised crystals using SEM (Fig. 29 b), TEM and AFM. Sellam et al. [103] approached their study using the concept of strained mixed dichalcogenides structures. Due to easier access to active sites, simple electron and ion transport, and improved electrochemical performance, the strained structure is very advantageous. They reported different degrees of strain varying with the

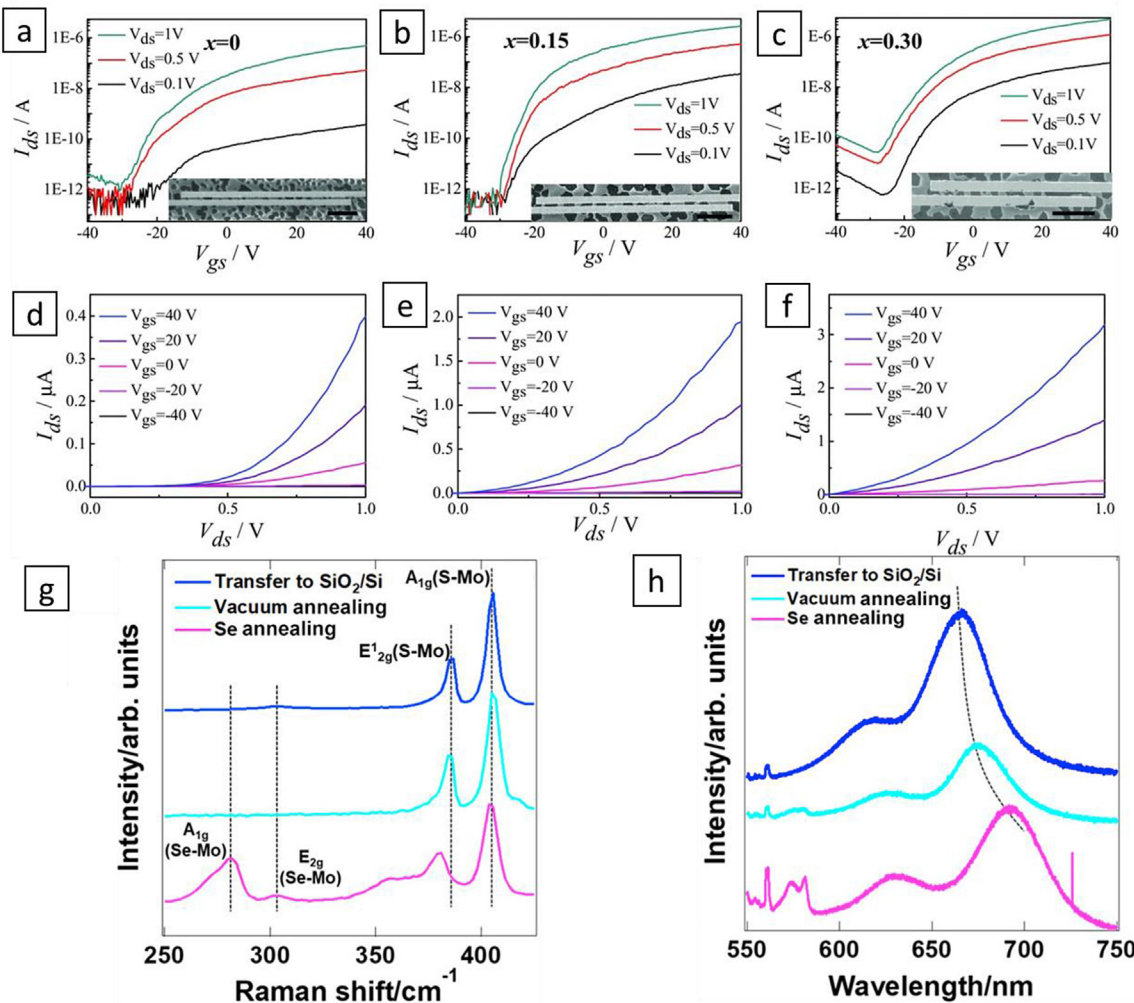


Fig. 28. (a-f) Characteristics of $\text{MoS}_{2(1-x)}\text{Se}_{2x}$ for possible applications in FETs [35]; (g) Raman spectra of modified MoS_2 with Se for possible applications in FETs [102]; (h) Photoluminescence spectra of modified MoS_2 with Se for possible applications in FETs [102].

S/Se ratio [103]. In a pristine MoX_2 type material, the transversal vibrational mode of X atoms with respect to Mo gives rise to the A_{1g} type of peaks, whereas the in-plane vibration of Mo-X bonds gives rise to the E_{2g} type of peaks. In pristine material, peaks at 407.4 and 382.7 cm^{-1} are associated with the A_{1g} (S) and E_{2g} (S) modes, respectively, while those at 239.1 and 287.8 cm^{-1} are associated with the A_{1g} (Se) and E_{2g} (Se) modes [103]. But in mixed dichalcogenides, splitting of A_{1g} and E_{2g} type peaks is observed, which is the result of strain in the material. Fig. 29c–f shows the different extents of splitting with S/Se ratio, proving the previous claim of variation of strain with a variation of S/Se ratio. Also, a shift of the low-frequency peaks (J_1 , J_2 , J_3) are observed with increased strain, and the merging of J_3 and E_{2g} peaks in Raman spectra is reported for the strained structure of 1T MoSSe. As a result of the strained structure, we see an improved conductivity in 1T MoSSe ($\sim 47 \text{ S cm}^{-1}$), compared to 1T MoX_2 (X = S or Se) [103] (Fig. 29 g).

The EIS analysis shows two different trends in high and low-frequency regions with variation of Se content [99] and resulted in different phase angles at different ranges of frequencies (Fig. 29h–j). This observation is justified with the hypothesis of different associated mechanisms of charge transport: a fast response due to the rapid adsorption of ions and a slow response due to pseudocapacitance brought on by slowly occurring redox transitions. It has been noticed that the 1T phase with a higher Se content shows a clear dip in the phase angle and a quick relaxation time in the high-frequency region. This demonstrates that the Se-rich phases exhibit a faster double-layer response than the S-rich phases. The variations in conductivities and pseudoactive characteristics of the compositions under study may be the cause of the variations in frequency response.

Along with an excellent response time of 0.68 m s in the dichalcogenides family, the 1T MoSSe phase also achieved high areal capacitances of 450 F cm^{-2} [103]. At very high scan rates of 1000 V s^{-1} , the i-v characteristics are almost rectangular compared to pristine MoX_2 , with

the presence of small peaks indicating the capacitive pseudo-behaviour of the material. After 10,000 charge-discharge cycles, capacitance retention of 90 % is reported, resulting in an energy density of 12.1 W h kg^{-1} at a specific power of 842 W kg^{-1} [103]. The sulfoselenide phase capacitors are desirable for high-power applications without sacrificing energy density due to the observed specific power of about 50 kW kg^{-1} at 1.5 W h kg^{-1} energy density [103].

5.5.2. Battery

The rapidly growing battery industry is in constant need of new materials and new methodologies in order to manage the demands of society. Recently, the layered chalcogenides gained immense attention in the application of battery electrode materials. This section will discuss the recent trend and development of MoSSe-type materials in the new-generation battery anode field.

In 2018, Shang et al. [104] theoretically predicted the application of Janus MX_Y (M = Mo, W; X or Y = S, Se, Te; X / = Y) type materials as a potential anode material for LIBs (Fig. 30 a). Shang et al. [104] investigated adsorption energy at different available sites of single-layer and double-layer MoSSe at different mass loading of Li.

In the case of the monolayer structure, the top sites are denoted as T, hollow sites as H, and the bridging sites as B (Fig. 30a and b). In the case of the double-layered structure, there are five available sites (T_S , T_{Se} , S_1 , S_2 , S_3) [104] (Fig. 30c and d). Calculation showed that hollow S_1 is the preferable site for Li adsorption in double-layered MoSSe (Fig. 30 e). The preferred adsorption site for Li also depends on the loading of Li. The calculation of adsorption energy and comparison with cohesive energy reveals that layer MoSSe can adsorb till $x = 6$, and double-layered MoSSe can adsorb $x = 7$. Hence, the calculated capacity of Li/Li + storage in single and double-layered MoSSe is 776.5 mAh g^{-1} and 452.9 mAh g^{-1} , respectively (capacity of commercial graphite anode 372 mAh g^{-1}) [104].

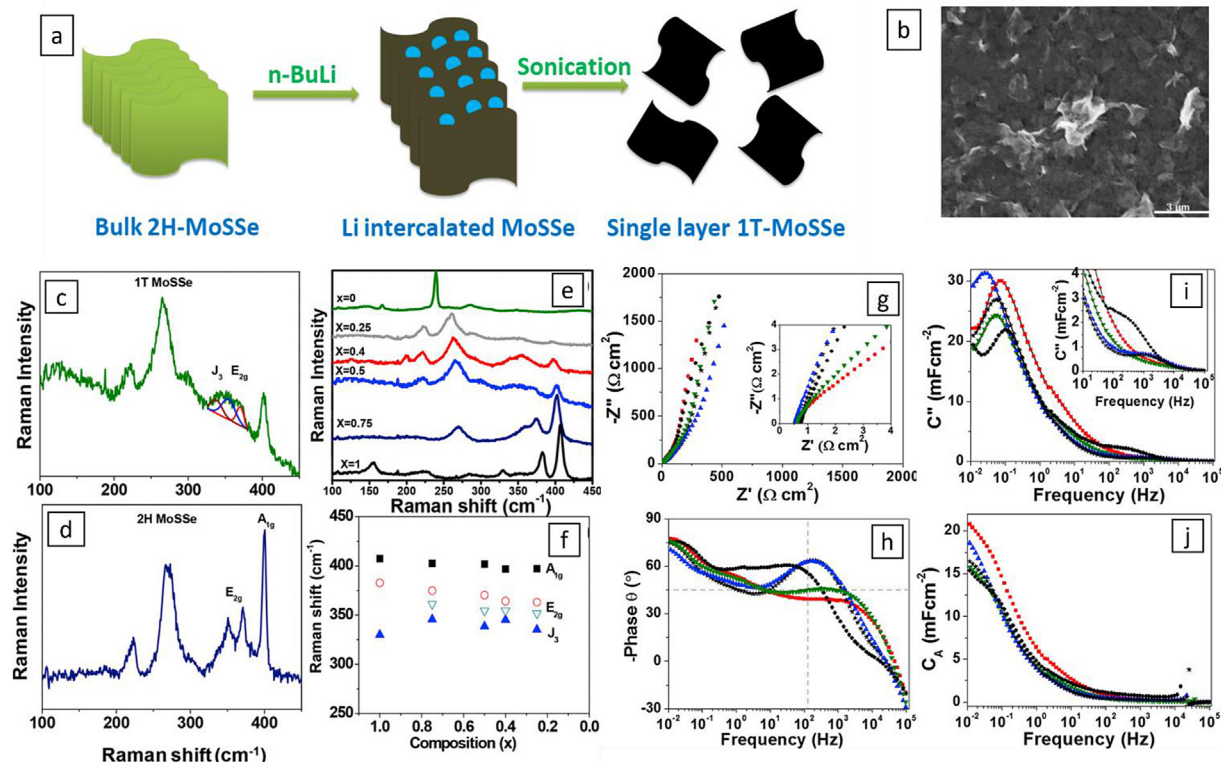


Fig. 29. Synthesis and performance of $\text{MoS}_{2x}\text{Se}_{2(1-x)}$ (where $x = 0-1$) type materials for their application in high-power supercapacitors [103]. (a) Synthesis of $\text{MoS}_{2x}\text{Se}_{2(1-x)}$ (where $x = 0-1$); (b) SEM image of nanoflakes in 1T MoSSe; (c–f) Raman analysis of $\text{MoS}_{2x}\text{Se}_{2(1-x)}$ (where $x = 0-1$) compared to 1T MoX_2 (X = S or Se); (h–j) EIS parameters analysis of $\text{MoS}_{2x}\text{Se}_{2(1-x)}$ (where $x = 0-1$).

$$\text{The OCV calculation formula [104]} : \text{OCV} = \frac{E_{\text{M}_x\text{host}} - E_{\text{M}_y\text{host}} - (x-y)\mu_{\text{M}}}{(x-y)} \quad (5)$$

The rate capability of the systems is analysed using DOS study (Fig. 30 f, g), which showed transmission of the MoSSe structures from semiconductors to metals with increasing Li content and enhancement of states in near Fermi level region that ensures availability of excess electron in the system to increase the conductivity [104]. The calculated OCV range for monolayer MoSSe is 0.16–0.6 V, and for double-layered MoSSe it is 0.17–1.01 V.

Wang et al. [105] reported a theoretical study on Janus MoSSe type material as a potential anode for the application of Na and K ion batteries and reported a high storage capacity of 510 mAh g⁻¹ and 203 mAh g⁻¹, respectively. They also reported that each layer of MoSSe could absorb 9 Na and 4 K atoms.

Lin et al. [106] conducted a similar kind of study on MoSSe/Graphene for the application of LiBs using first principle calculation, and they reported a capacity of 560.59 mA h/g, which is sufficiently higher than commercial anode materials. They carried out their study using two different configurations of the molybdenum sulfoselenide structure:

SeMoS and SMoSe. The band structure analysis (Fig. 30 h-k) of MoSSe/Graphene shows a decrease in the band gap of MoSSe upon the addition of graphene, indicating increased conductivity in the system. The DOS analysis shows (Fig. 30 l-o) the upward movement of Fermi level upon increased Li intercalation, which implies charge transfer from Li to MoSSe/Graphene and confirms the predicted enhancement in conductivity. The calculated OCV range for SMoSe/Graphene and SeMoS/Graphene is 0.17–0.41 V and 0.17–0.76 V, respectively, within the ideal electrode potential range (0.10–1.00 V) [106]. Apart from this electrochemical investigation, Lin et al. [106] also investigated the mechanical stability of MoSSe/Graphene anode in order to prevent capacity fading during a continuous charge-discharge process. The calculated Young's modulus for SMoSe/Graphene and SeMoS/Graphene is ~459 N/m, which is a huge increase from 116 N/m of pristine MoSSe, which implies better practical application possibilities [106].

Similar to Lin et al. [106], He et al. [107] conducted a study on the MoSSe/C₃N system using the two different configurations of SMoSe/C₃N and SeMoS/C₃N for the application of Li and Na ion batteries. He et al. [107] reported the calculated Young's modulus of the system ~463 N/m along the X direction. The DOS analysis (Fig. 31 a,b) shows enhanced states near the Fermi level region, proving increased conductivity of the

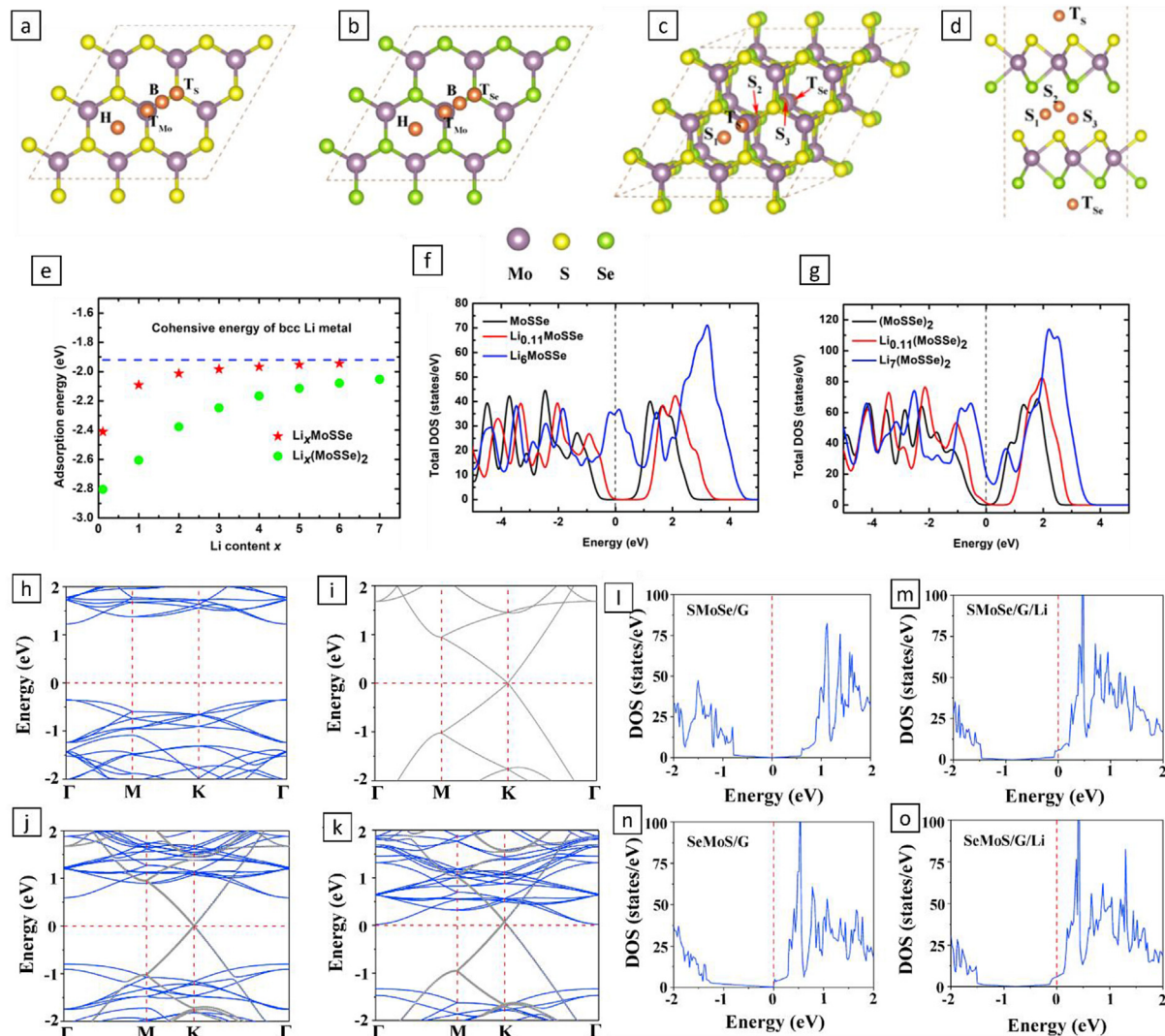


Fig. 30. (a, b) Available sites in single-layered MoSSe [104]; (c, d) Available sites in double-layered MoSSe [104]; (e) Adsorption and cohesion energy comparison at different Li loading [104]; (f) DOS analysis of single-layered MoSSe [104]; (g) DOS analysis of double-layered MoSSe [104]; (h) Band structure of MoSSe [106]; (i) Band structure of Graphene [106]; (j) Band structure of SMoSe/Graphene [106]; (k) Band structure of SeMoS/Graphene [106]; (l-o) DOS analysis of MoSSe-/Graphene [106].

system upon the addition of Li/Na. For Li, the theoretical capacity was calculated as 494.98 mAh g⁻¹; for K, the theoretical capacity was calculated to be 382.08 mAh g⁻¹. All the OCV values (Fig. 31 c,d) lie in the range of 0.1–1.0 V, ensuring no cluster is formed during cycling for both Li and Na electrodes [107].

Ersan et al. [108] reported the lithium adsorption and diffusion on hexagonal MoS_{2(1-x)}Se_{2x} monolayers with variations of x for 0.00, 0.33, 0.50, 0.66, and 1.00 on the basis of first-principles plane-wave calculations. At the same time, MoS_{2(1-x)}Se_{2x} compounds in their bare form are nonmagnetic semiconductors with an x -dependent energy band gap, and the DOS analysis (Fig. 31 e) shows the addition of Li atom enhances the $s-p$ hybridisation, which results into enhanced conductivity [108].

Zhang et al. [109] reported MoS_{2-x}Se_x/Graphene ($x = 0.4, 0.8, 1.2$) type composite with interlayer separation of 0.66 nm and verified its applicability with both experimental evidence. The synthesis process is shown in Fig. 32 a. MoS_{2-x}Se_x/Graphene ($x = 0.8$) shows better performance due to larger interlayer separation owing to better ion intercalation and 509 mA h g⁻¹ charge capacity at 0.1 A g⁻¹ after 200 cycles, and it also shows coulombic efficiency of 99.3 % at 2 A g⁻¹ (Fig. 32 b). A comparison amongst MoS_{2-x}Se_x/Graphene ($x = 0.4, 0.8, 1.2$) performance is listed in Table 4. The morphological change during cycling is the cause of increased capacitance during the reaction. The same phenomena also cause a decrease in charge transfer resistance with continuous cycling [109] (Fig. 32 c).

He et al. [110] achieved effective introduction of anion vacancies in MoS_{2(1-x)}Se_{2x} alloys through a simple alloying reaction. By adjusting the chemical composition, they optimized the vacancy concentration. These anion vacancies significantly enhanced the electronic conductivity, induced more active sites, and alleviated structural variations during potassium storage. When used as potassium ion battery anodes, the most optimized vacancy-rich MoSSe alloy delivered high reversible capacities

at different current densities, demonstrating its potential for energy storage applications. This work provides a practical approach to modify the electronic and defect properties of transition metal dichalcogenides, paving the way for advanced electrode materials in battery systems.

5.5.3. Catalysis

5.5.3.1. Electrocatalysis. HER activity on TMD is a well-established phenomenon, and its efficiency can be controlled by modifying its chemical composition [111,112]. For instance, it is known that MoS₂ performs better electrocatalytically when it is doped with a small amount of cobalt or nickel cations [113]. Additionally, other chalcogens can replace all or part of the sulfur in MoS₂, creating possibilities of compounds with potential for HER; it has been discovered that the selenium analogue MoSe₂ is also HER active. Though according to calculations, the hydrogen adsorption is slightly too weak on Mo-S edges ($\Delta G_H = 80$ meV) but slightly too strong on Mo-Se edges ($\Delta G_H = -140$ meV) [114,115].

Gong et al. [116] reported the possibility of achieving the ΔG_H (the hydrogen adsorption free energy) value close to thermodynamically feasible prediction ($\Delta G_H = 0$ meV) by tuning the Se composition in MoS_{2(1-x)}Se_{2x} ($x = 0, 1/3, 1/2, 2/3, 1$) alloys. The morphology of as-prepared MoS_{2(1-x)}Se_{2x} alloys was nanoflakes of monolayer + multilayers that have a high surface area and exposed edges, which have been thermodynamically proven to be more feasible than basal planes for electrocatalytic HERs [117]. The evolution of edge structures has also been confirmed with Raman spectra analysis, which shows a large E_{2g}/A_{2g} intensity ratio. Polarisation, overpotential, Tafel analysis, and turnover frequency (TOF) measurements show that MoSSe performs better than its other prepared analogues with different x values with lower overpotential and higher TOF. The charge transfer resistance values support the trend of TOF measurement, proving that MoSSe has a

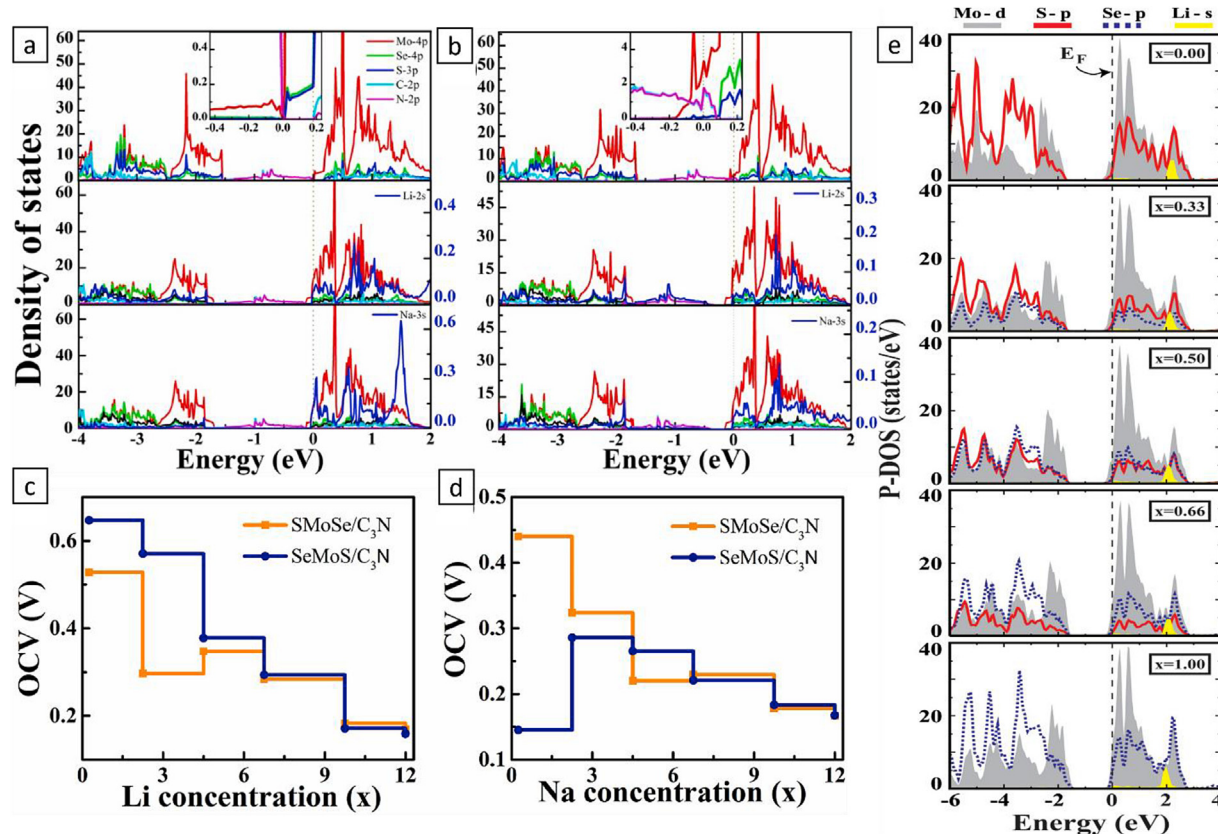


Fig. 31. (a) DOS analysis for SMoSe/C₃N [107]; (b) DOS analysis for SMoSe/C₃N [107]; (c) OCV analysis in Li electrode [107]; (d) OCV analysis in Li electrode [107]; (e) DOS analysis for MoS_{2(1-x)}Se_{2x} [108].

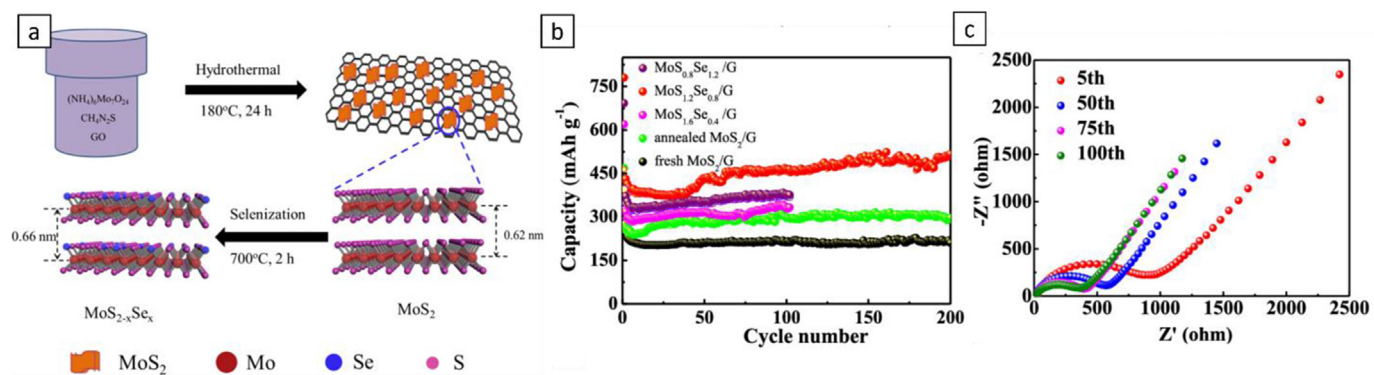
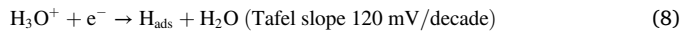


Fig. 32. (a) Synthesis schematic of $\text{MoS}_{2-x}\text{Se}_x/\text{Graphene}$ ($x = 0.4, 0.8, 1.2$) [109]; (b, c) Electrochemical performance of $\text{MoS}_{2-x}\text{Se}_x/\text{Graphene}$ ($x = 0.4, 0.8, 1.2$) [109].

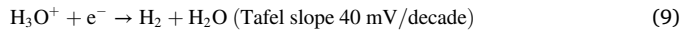
better electrochemically active surface area. The analysis is provided in detail in Fig. 33 ac [116]. Table 5 compares the catalytic performance of $\text{MoS}_{2(1-x)}\text{Se}_{2x}$ for the HER at various compositions indicated by the value of x ranging from 0 to 1 [116].

Yang et al. [118] reported $\text{MoSe}_x\text{S}_{2-x}$ grown on CNTs with enhanced performances compared to bare MoSSe alloys for the application of HER (Fig. 33 d). The electrocatalytic performance of $\text{MoSe}_x\text{S}_{2-x}$ grown on CNTs has also been tabulated in Table 7. The analysis shows that the addition of highly conductive CNTs provided higher surface area and better electrode transport, which facilitates enhanced performance by providing access to more active sites through less resistive pathways. According to the literature, there are three different pathways predicted for HER [122].

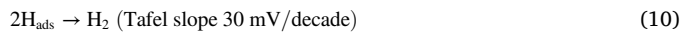
1) Volmer reaction:



2) Heyrovsky reaction:



3) Tafel reaction:



The Volmer reaction is the primary step associated with either the Heyrovsky or Tafel reaction as the final step. We can get an idea of the reaction taking place in the system from the Tafel slope value. According to the literature, if $40 \text{ mV/decade} < \text{Tafel slope} \leq 70 \text{ mV/decade}$, the reaction mechanism consists Volmer-Heyrovsky reaction, and if the Tafel slope $\leq 40 \text{ mV/decade}$, the reaction mechanism involves the Volmer-Tafel reaction [122]. Table 6 shows that CNT-MoSe_xS_{2-x} ($x = 1.06$) follows Volmer-Tafel, which is beneficial for practical applications [118].

Similarly, Qiao et al. [123] reported ultrathin MoSSe alloy nanosheets array on multiwalled carbon nanotubes (MWCNTs) to form a core-shell structure via a simple solvothermal process which exhibited a Tafel slope of 38 mV/decade and overpotential of 102 mV @ 10 mA/cm². Their 3D hierarchical structure, which can increase the intrinsic

conductivity of MoSSe and lead to a higher ECSA value and rapid electron transfer, is thought to be responsible for the improved HER performance. On the other hand, in addition to the edge sites, the alloy effects may cause defects and residual strains on the basal plane of MoSSe nanosheets, resulting in a large number of catalytically vacancy sites [123].

Wang et al. [119] reported improved HER activity due to synergistic tuning of Se and S ratio in MoSSe alloys. The analysis shows that tuning the Se and S ratio improved the performance of 2H MoSSe in terms of electrical conductivity and accessible active sites. They modulated the degree of disorderliness in $\text{MoS}_{2x}\text{Se}_{2(1-x)}$ by varying the temperature of hydrothermal synthesis. The analysis of each sample has been done based on their synthesis temperature and x values for the parameters of conductivity, Tafel slope, over potential, and charge transfer resistance. 2H-MoS_{0.2}Se_{1.8} synthesised at 160 °C is found to be peaking in performances compared to other samples with 50 mV/decade Tafel slope and overpotential of 136 mV [119]. The characteristic values of the key parameters are shown in detail in Fig. 33 f-h.

As most of the research included on the 2H phase of MoSSe, Lin et al. [120] focused on synthesising a mixed phase of 1T and 2H MoSSe for the catalytic applications using a one-step hydrothermal synthesis, which has been shown in Fig. 33 i. The ratio of the 1T and 2H phases was controlled by controlling the synthesis temperature. The content of the 1T phase gradually increased with temperature, peaked, and then began to decline, indicating that a temperature similarly high (~180 °C) could partially convert the 1T phase back into the 2H phase. Accordingly, as the temperature rises, the electrocatalytic performance of MoSSe improves, and as the temperature rises further, the performance declines, demonstrating the superiority of the 1T phase in controlling better catalytic activities [120]. The high concentration of the 1T phase, a metal phase with higher conductivity, contributes to the excellent electrocatalytic performance [120]. The coexistence of 1T and 2H phase was confirmed by Raman spectra analysis; the E_{1g} (S-Mo) and E_{2g} (S-Mo) molecular vibration modes of 2H-MoS₂ are, respectively, assigned to two vibration modes, 282 cm⁻¹ and 376 cm⁻¹ (Fig. 33 j). $\text{Mo}(\text{S}_{1-x}\text{Se}_x)_2$ nanoparticles exhibit a vibration peak at 282 cm⁻¹ that gradually shifts to a low-frequency region as x rises. Additionally, a number of vibration modes of 1T-MoS₂ (236 cm⁻¹ and 336 cm⁻¹) and of 1T-MoSe₂ (354 cm⁻¹ and 484 cm⁻¹) showed that the 2H phase and the 1T phase could coexist (Fig. 33 j) [120]. At $x = 0.5$, the reported Tafel slope is 42 mV/decade, which shows improved catalytic performance of mixed-phase MoSSe systems [120].

As mentioned previously, the basal plane of Janus MoSSe is considered less catalytically active [117]; further research has been focused on ways to improve the performance by incorporating transition metals. The stability of the material is a key requirement for SAC materials to be used repeatedly. A strong bond between the substrate and the doped atom is required to prevent the polymerisation of a single atom. Xiao et al.

Table 4
Comparison in electrochemical performance of $\text{MoS}_{2-x}\text{Se}_x/\text{Graphene}$ ($x = 0.4, 0.8, 1.2$) [109].

$\text{MoS}_{2-x}\text{Se}_x/\text{Graphene}$	1st discharge capacity (mAh g ⁻¹)	1st charge capacity (mAh g ⁻¹)
$x = 0.4$	692	395
$x = 0.8$	780	464
$x = 1.2$	419	252

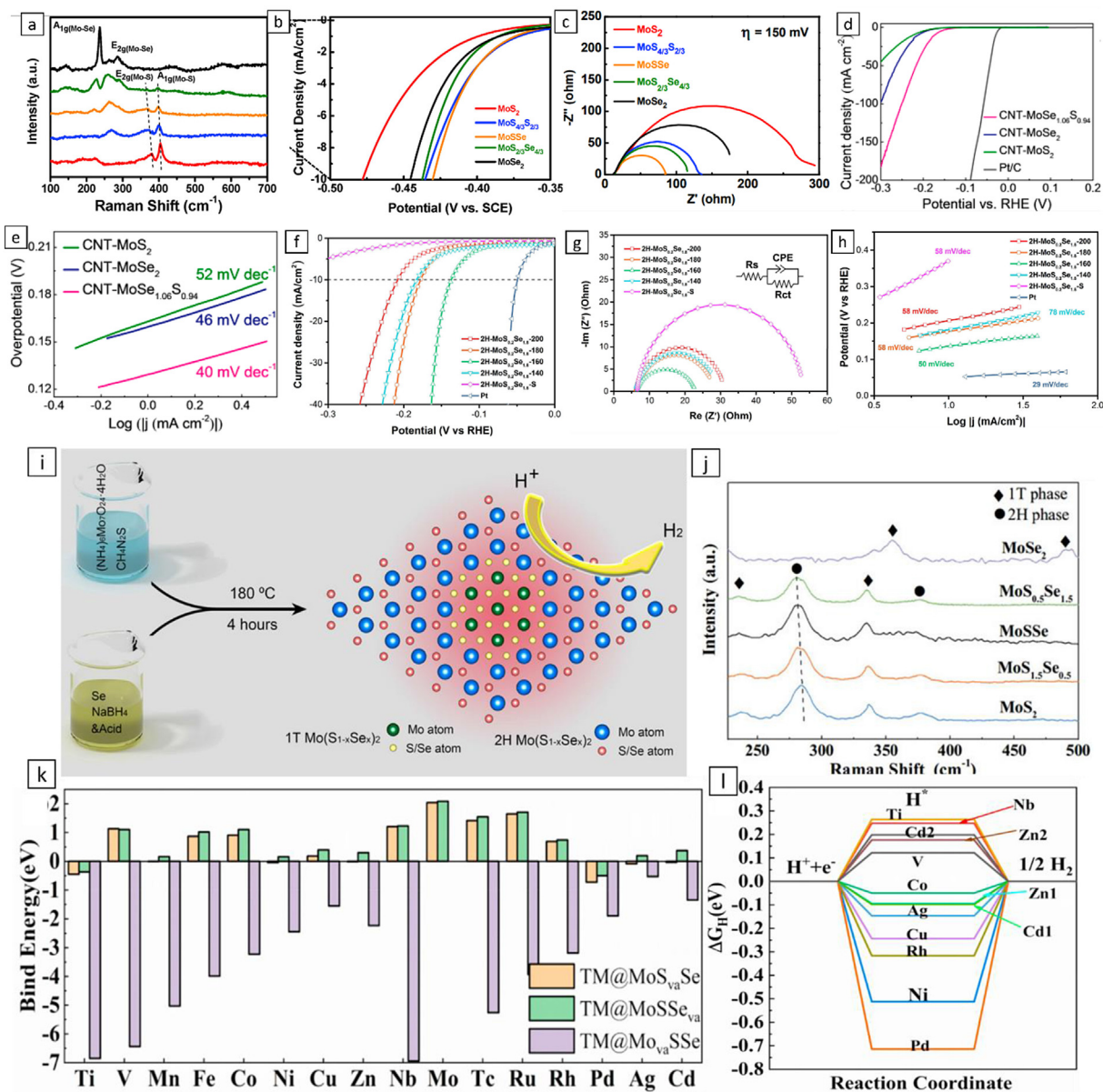


Fig. 33. (a) Raman spectra of $\text{MoS}_{2(1-x)}\text{Se}_{2x}$ ($x = 0, 1/3, 1/2, 2/3, 1$) alloys [116]; (b) Polarisation curves for catalytic activity analysis of $\text{MoS}_{2(1-x)}\text{Se}_{2x}$ ($x = 0, 1/3, 1/2, 2/3, 1$) alloys [116]; (c) EIS analysis for catalytic activity comparison of $\text{MoS}_{2(1-x)}\text{Se}_{2x}$ ($x = 0, 1/3, 1/2, 2/3, 1$) alloys [116]; (d) Polarisation curves for catalytic activity analysis of $\text{MoSe}_x\text{S}_{2-x}$ grown on CNTs [118]; (e) Tafel slope comparison in $\text{MoSe}_x\text{S}_{2-x}$ grown on CNTs [118]; (f) Polarisation curves for comparing catalytic activity of $2\text{H MoS}_{2x}\text{Se}_{2(1-x)}$ [119]; (g) EIS analysis for catalytic activity comparison of $2\text{H MoS}_{2x}\text{Se}_{2(1-x)}$ [119]; (h) Tafel slope comparison in $2\text{H MoS}_{2x}\text{Se}_{2(1-x)}$ [119]; (i) Synthesis schematic of mixed phase 1T/2H MoSSe for the application of HER [120]; (j) Raman spectra of mixed phase 1T/2H MoSSe for the application of HER [120]; (k) Binding energy calculation on TM@ $\text{Mo}_{\text{va}}\text{Se}$, TM@ $\text{MoS}_{\text{va}}\text{Se}$, and TM@ MoSSe_{va} for the application of HER [121]; (l) Gibbs free energy calculation for hydrogenation on TM@ $\text{Mo}_{\text{va}}\text{Se}$, TM@ $\text{MoS}_{\text{va}}\text{Se}$, TM@ MoSSe_{va} for the application of HER [121].

reported three common structures for TM@MoSSe, including those in which one of the Mo, S, or Se atoms was replaced by one of the TM atoms, respectively (TM@ $\text{Mo}_{\text{va}}\text{Se}$, TM@ $\text{MoS}_{\text{va}}\text{Se}$, TM@ MoSSe_{va}). They calculated binding energy using Equation (11) [121].

$$E_b = E_{\text{TM@MoSSe}} - E_{\text{d-MoSSe}} - E_{\text{single-TM}} \quad (11)$$

Negative binding energy indicates better adsorption, and positive binding energy indicates poor adsorption. The results of the calculations

Table 5

Enhanced catalytic performance of $\text{MoS}_{2(1-x)}\text{Se}_{2x}$ [116] and $\text{MoSe}_x\text{S}_{2-x}$ grown on CNTs [118] for the application of hydrogen evolution reaction at different values of x .

	MoS _{2(1-x)} Se _{2x}					CNT-MoSe _x S _{2-x}				
	$x = 0$	$x = 1/3$	$x = 1/2$	$x = 2/3$	$x = 1$	$x = 0$	$x = 0.93$	$x = 1.06$	$x = 1.20$	$x = 1$
Overpotential @ 10 mA/cm ² (mV)	~219	~172	~164	~171	~181	~213	~180	~174	~204	~224
Tafel slope (mV/decade)	~91	~66	~48	~55	~45	~46	~43	~40	~44	~52
TOF @150 mV (s ⁻¹)	~0.04	~0.05	~0.08	~0.07	~0.06					

Table 6

Calculated adsorption energy and diffusion energy barrier of each species at their favourable adsorption sites [126].

Species	Adsorption energy		Diffusion energy barrier (eV)	
	S site	Se site	S site	Se site
H	−1.75 (H1)	−1.50 (H1)	0.32 (intra hexagons)	0.10 (intra hexagons)
			0.08 (inter hexagons)	0.32 (inter hexagons)
OH	−1.29 (T) Tilt)	−1.18 (H1 Tilt)	0.65	0.26
O	−5.18 (T)	−4.28 (T)	2.48	1.52

Table 7

Feasibility of possible reactions during photocatalytic water splitting on MoSSe surfaces from an energy point of view [126].

Reactions	Relative energies (eV)	
	S site	Se site
2H → H ₂	−3.05	−3.51
2OH → O [·] + 2H ₂ O	−2.53	−1.92
H ₂ O + O [·] → + H ₂ O ₂	1.70	0.92
O [·] + O [·] → O ₂	1.70	−0.82

are shown in Fig. 33 k. The fact that all of the structures of TM@Mo_xSSe have negative E_b values shows how well-suited the Mo-defective MoSSe is as a substrate and how stable the TM atoms are anchored on the Mo-defective MoSSe. Furthermore, we discovered that the binding energy of TM@Mo_xSSe exhibits a general repeated trend in the same row of the periodic table; namely, binding energy rises as elementary metallicity falls. Further calculation of hydrogen adsorption (H_{ad}) shows that Se-defected TM@MoSSe structures are not suitable for HER reaction. H_{ad} is calculated using Equation (12) [121].

$$E_{ad}(H) = E_{H^+} - E_{(^\ast)} - \frac{1}{2}E_{(H_2)} \quad (12)$$

Further screening process was continued by calculating the Gibbs free energy (Fig. 33 l) of hydrogenation. ΔG_H is calculated using Equation 6.13 [65,121].

$$\Delta G_H = [E_{H^+} + E_{ZPE(H^+)} - T\Delta S_{(H^+)}] - \frac{1}{2}[E_{(H_2)} + E_{ZPE(H_2)} - T\Delta S_{(H_2)}] - E_{(^\ast)} \quad (13)$$

(ZPE:Zero-point energy).

After screening from 18 TMs (T, V, Cr, Mn, Fe, Co, Ni, Cu, Zn, Zr, Nb, Mo, Tc, Ru, Rh, Pd, Af, Cd), Co@Mo_xSSe, Zn@Mo_xSe and Cd@Mo_xSe were found to behave nearly ideal with ΔG_H value close to 0. The improvement due to transition metals is mainly due to the increased conductivity of the system. TM doping allows the unoccupied states near the Fermi level to lower their energy, and as a result, the transfer of electrons becomes easier. To activate the inert basal plane of the pure MoSSe for HER, Zn, Cd, and Co) doping increases the unoccupied states near the Fermi level, enhancing the hybridisation between H-s and TM@MoSSe systems and forming stable hydrogen adsorption states [121].

To achieve high current density for the hydrogen evolution reaction (HER) with Janus MoSSe, its unique properties must be utilised to enable efficient electron transfer and hydrogen evolution. The distinct electronic structure of Janus MoSSe and the numerous active sites make it an excellent candidate for HER catalysis [124]. In particular, the Janus structure provides a favourable balance between Mo and S atoms, creating an environment conducive to catalytic activity. In addition, the 2D morphology of MoSSe provides a large surface area for active catalytic sites, improving reactant accessibility. In addition, the semiconducting

nature of MoSSe enables effective charge transfer kinetics that promote rapid electron transfer during the HER process [125]. By utilizing these properties, Janus MoSSe can effectively lower the overpotential required for HER, resulting in high current density and improved overall catalytic performance. Experimental studies and theoretical modeling play a crucial role in elucidating the underlying mechanisms and optimizing Janus MoSSe catalysts for improved HER activity.

5.5.3.2. Photocatalysis. In recent years, 2D materials have been studied widely for the application of photocatalytic water splitting for the production of clean hydrogen fuel, as the reported catalysts for the same are found to be inefficient for the overall completion of the process (example: g-C₃N₄). Hence, the search for an efficient 2D photocatalyst is an important and emerging research topic. Janus MoSSe monolayer is an attractive choice for this cause due to its reduced recombination efficiency, appropriate stability with water redox potential and absorption range of visible light (Fig. 34 a).

A built-in electric field pointing from the Se-surface to the S-surface is created by the intrinsic electric dipole moment in the Janus MoSSe monolayer that drives the photoexcited electrons and holes to move quickly in the opposite directions, accumulating as electrons in the Se-surface and holes in the S-surface [126–128] (Fig. 34 b). The built-in inductive effect reduces the recombination time of electron and hole pairs, which is a much-required phenomenon in water-splitting catalysts [121]. Ma et al. demonstrated that subjecting the Janus MoSSe monolayer to isotropic and uniaxial tensile strains results in a reduction in the band gap. In addition a transition from a direct to an indirect band gap was also observed. This not only broadens the light absorption range but also further reduces the recombination of photo-generated carriers (Fig. 34 c, d). By reducing the recombination rate, the excited carriers (electrons and holes) exhibit longer lifetimes. This enhances the probability that these carriers will engage in photocatalytic reactions before recombining, thus amplifying the efficiency of the photocatalytic process [121].

Jin et al. [129] time-dependent DFT study showed the recombination time in MoSSe to be 1.31 ns. In contrast, the MoSSe nanotube configuration reported by Zhang et al. [127] has a high recombination time of 33 ns [127]. In this instance, the OER and HER both primarily take place on the S-surface and Se-surface, respectively [126]. Guan et al. [20] also investigated the strain effect on monolayer MoSSe, which shows the tunability of the electronic and optical properties, similar to the ones reported by Ma et al. [128].

Lei et al. [126] reported the suitability of H₂ production on MoSSe layer using first-principal calculations. They examined the suitable sites (Fig. 33 e) on MoSSe layer and the energy barrier of the movement of H atoms, which was found to be very low. Lei et al. [126] also calculated the relative reaction energies for each possible orientation of the adsorbed species. The calculated results are reported in Table 7. These calculations suggest that MoSSe-type materials are suitable for H₂ production on both the S and Se side when 2 H atoms are in close vicinity. The suggested mechanism is:



Or,



Similar to the direct photo reduction, one can expect direct photo oxidation in order to produce oxygen according to the reaction 16 [126].



Or,



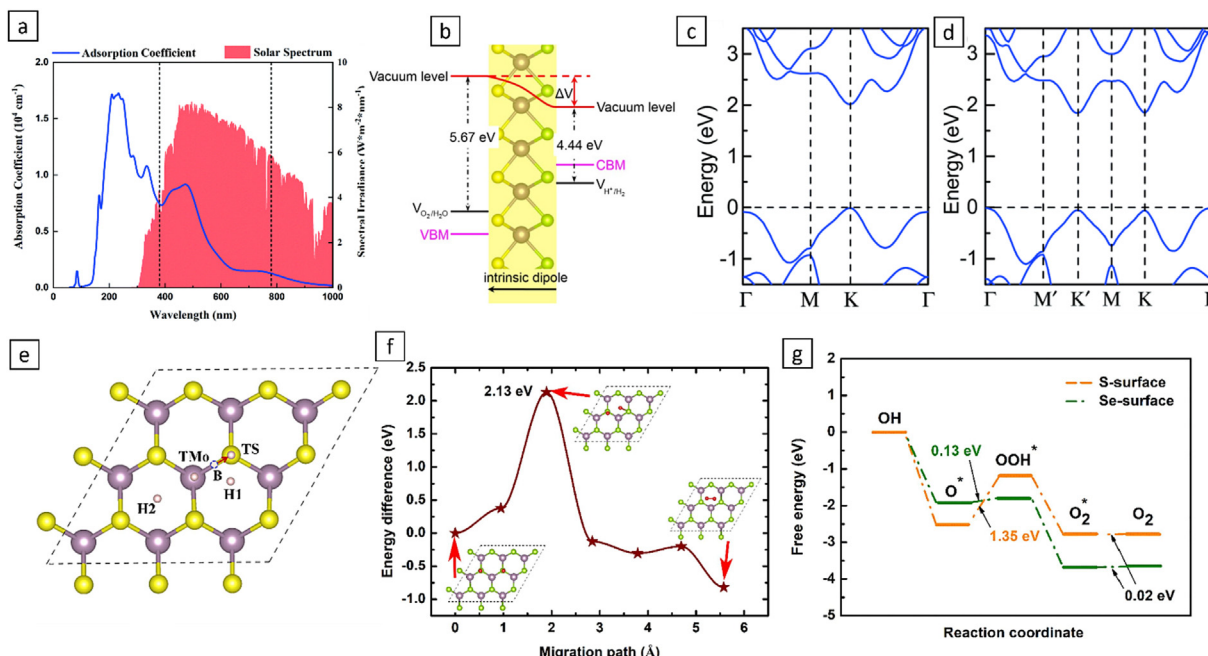


Fig. 34. (a) Light adsorption range of MoSSe [127]; (b) Band alignment and intrinsic electrical field in MoSSe [128]; (c) Direct band gap pristine MoSSe [128]; (d) Indirect band gap of strained MoSSe [128]; (e) Possible adsorption sites on MoSSe [126]; (f) OER reaction kinetics by the combination of 2 O atoms [126]; (g) Energy diagram of indirect OER reaction species [126].



In order to verify the feasibility of Equation (16), Lei et al. [126] performed a similar stability, adsorption and migration possibility calculation for OH and O^{*} atoms. The calculations for OH atoms show that Se surface prefers OH bonding less than S surface and as a consequence, the movement of OH on Se layer is much easier compare to the same on S layer. Though the relative energy calculation shows favourable adsorption of H₂O + O^{*} product on both S and Se sites [126].

In order to evaluate the practicality of the application, the excess possibility of H₂O₂ formation has been examined due to the excess presence of water in the reaction medium during the operation is considered. However, the calculated relative energy values show that the formation of H₂O₂ is not energetically favourable [126].

Further in their research, Lei et al. [126] investigated the stability and diffusion possibility of O^{*} atoms. According to their calculations, the O^{*} atoms are more suitably adsorbed on the S layer than compared to the Se layer [126]. But, the diffusion energy barrier is high on both the surface of MoSSe that, prohibits the migration of O^{*} atoms (Fig. 32 f). Reaction energy barrier calculation shows that the formation of O₂ via the reaction XX is favourable energetically but prohibited kinetically with a huge energy barrier of 2.13 eV [126]. Hence, an indirect OER mechanism via OOH* was proposed, but the energy profile diagram (Fig. 32 g) shows weak adsorption of OOH* and strong adsorption of O^{*} that slowly oxidises the MoSSe monolayer and stops the reaction. The indirect OER reaction steps are:



Xu et al. [79] analysed the effect of vacancy or defects on the MoSSe surface on the application of photocatalytic water splitting. They have considered three main types of vacancy: S vacancy (S_{vac}), Mo anti-defect (Mo_{anti}), and Mo interstitial (Mo_{int}). In order to compare the changes in

electronic properties of a defective MoSSe, a detailed PDOS analysis (Fig. 35 a) has been done. Given that the water is adsorbed at the S side, only the electronic densities of states for the Mo, S, O, and H atoms are considered for the PDOS study [79]. We can observe that the adsorbed water's PDOS remains in three intact peaks resembling a single water molecule for pristine sheets. This strongly implies that the adsorbed water has a weak adsorption energy of about -0.16 eV and hardly interacts with the pure Janus MoSSe sheet. In the structure containing tabletataS_{vac}, the three peaks are almost preserved, but their locations have a slight red shift toward lower energy levels, indicating that water adsorption is preferred and has a larger adsorption energy of about -0.23 eV. The situation is very different for Mo_{anti} and Mo_{int} defects [79]. The three peaks unexpectedly vanish, and the adsorbed water's PDOS disperses over a wide area, pointing to a strong interaction between the water's O-2p orbital and the Mo-3d orbitals of the Mo_{anti} and Mo_{int} defect [79]. Additionally, for the Mo_{anti} and Mo_{int} defect sheets, the PDOS of the adsorbed water are distributed between -6.6 eV and -5.0 eV and -6.0 eV and -5.2 eV, respectively. Therefore, in comparison to the water adsorbed at the pure Janus MoSSe sheet, the PDOS for the adsorbed water exhibits a striking redshift. As a result, the water adsorption energy at the Mo_{anti} and Mo_{int} defect Janus MoSSe sheet increases and is measured at -1.4 eV or -1.2 eV, respectively. As a result, the orbital interaction between the O-2p of the water and the Mo-3d of the defects, along with the red shift of the water-energy level, should be the cause of the enhanced adsorption energy of water at the defective S side of the sheet [79].

Ma et al. [130] examined the effects of Sc-Zn transition metal (TM) elements on single atom adsorption using first principle studies on the mechanism of interaction between the water molecule and MoSSe as well as on the other inherent characteristics of MoSSe as a water-splitting photocatalyst. According to the results, with the exception of Zn, all TMs can chemically and strongly adsorb on both the S and Se sides of MoSSe [130]. The initial weak van der Waals interaction between water and pure MoSSe is successfully changed into strong chemical interactions in the TM-modified MoSSe, where TMs act as very active sites for photo-catalysing water-splitting [130].

After analysing the adsorption characteristics, it has been found that

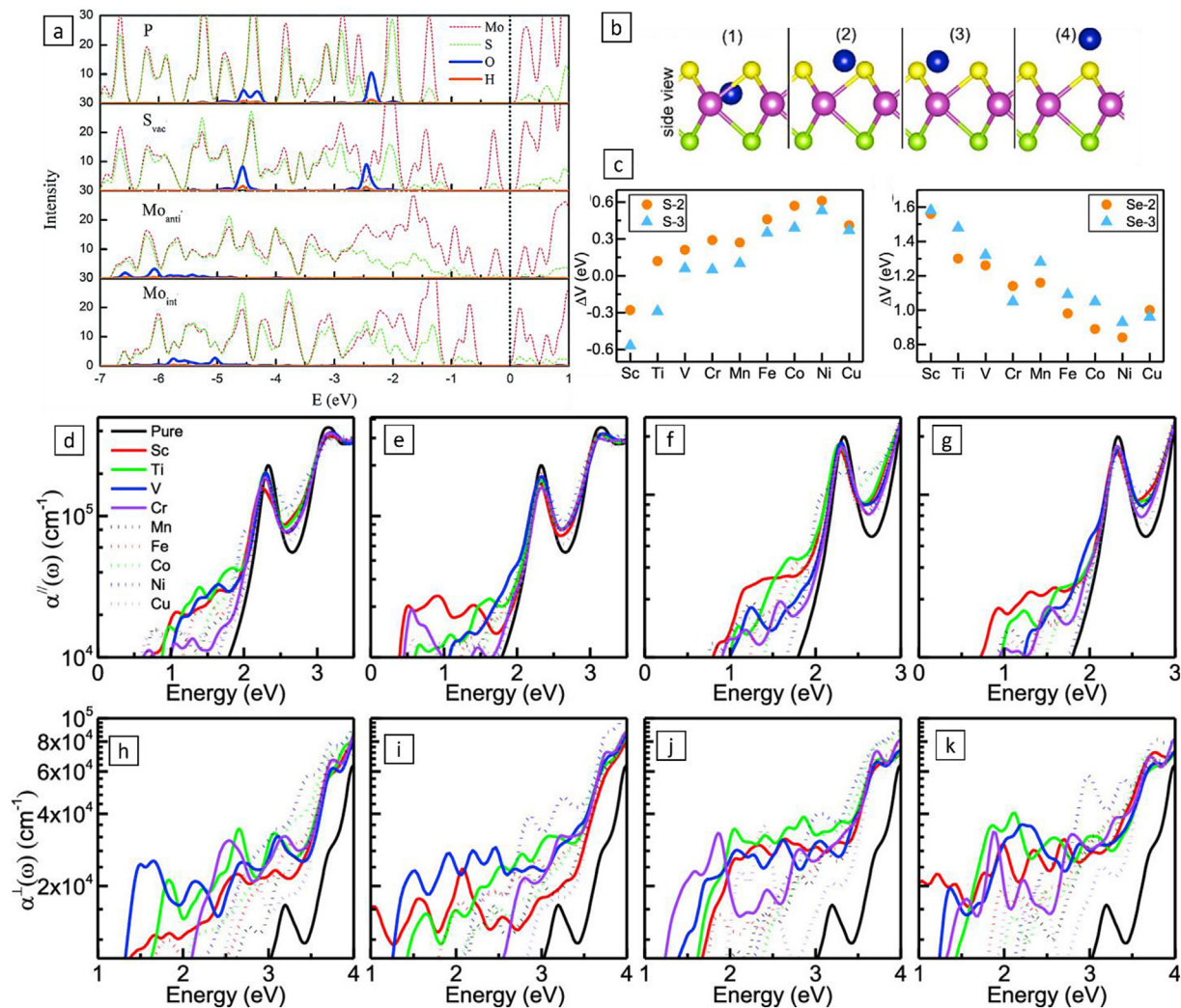


Fig. 35. (a) PDOS analysis for vacancy-engineered MoSSe for the application of photo water splitting [79]; (b) 4 possible adsorption sites on MoSSe for the adsorption of TMs (the S layer is shown in this figure, but the similar adsorption sites are present on Se layer as well) [130]; (c) The change in potential difference between S and Se site due to TM doping on MoSSe for the application of photo water splitting [130]; (d–k) The optical enhanced adsorption characteristics due to TM doping on MoSSe for the application of photo water splitting [130].

Zn gets weakly bonded to the MoSSe surface, whereas Ni gets strongly bonded. Also, among possible four adsorption sites, two sites for Ti and V and one for Cr, Mn, and Fe have been reported, indicating the stability of other TMs on the other possible sites (Fig. 35 b: 1, 2, 3, 4). The most preferred adsorption sites are S/Se-2 and S/Se-3. The investigation on the effect of the intrinsic potential field of MoSSe with the addition of TMs shows a decrease in the potential difference between S and Se sites for the S-2/3 adsorption sites, whereas it shows a significant increase for Se-2/3 adsorption sites (for pristine MoSSe the potential difference is 0.77 eV) (Fig. 35 c) [130]. This is because the electron transfer from TM to the Se side of MoSSe results in an electric dipole identical to the intrinsic one of pure MoSSe, further increasing the potential difference. The electronegativity difference between S/Se and TMs can qualitatively predict this potential difference. In S-2/3 structures, the electron transfer from TM to the S side of MoSSe introduces an electric dipole that is opposite to the intrinsic one of pure MoSSe, decreasing V . The significantly higher V is very advantageous for further boosting the photo-redox potentials and separation rates of photogenerated carriers, improving their photocatalytic performance [130]. Also, the TM addition shows enhanced optical adsorption efficiency, especially for Sc, Ti, V and Cr [130] (Fig. 35 d–k).

Guan et al. [20] analysed the stacking possibilities (Fig. 36 a) and the performance of each configuration. The different configurations and the calculated results are shown in Fig. 36 b. From all these analyses, we find that the A'B type of layer is suitable. Still, all the various stacking configurations have VB maxima lower than the photo-oxidation potential [O_2/H_2O (-5.67 eV)], whereas the CB minima are located below the photo reduction potential [$H+/H_2O$ (-4.44 eV)] [20]. For feasible production of H_2 and O_2 simultaneously by water splitting, the VB maxima should be lower than the photo-oxidation potential, and the CB minima should be higher than the photo-reduction potential [20]. So, the results suggest MoSSe bi-layers are suitable for photocatalytic oxidation but not photocatalytic reduction due to thermodynamic non-feasibility [20].

In an experiment, N + F co-doped MoS_2 was shown to be superior to mono-doping for HER [131]. Considering this idea, Zhao et al. [85] performed a similar study on MoSSe monolayer to be used as an effective photocatalyst. They reported N and F as better doping elements than N and P, which can effectively form charge-trapping states near the Fermi level due to excess empty states and can reduce the photocatalytic efficiency by increasing recombination percentage. Further studies show that N and F-doped MoSSe can harvest light in the 200–500 nm range. All N, F co-doped MoSSe structures can be seen to have CB minima that are

higher than hydrogen reduction potential and VB maxima that are lower than water oxidation potential under the condition, which shows that all of the co-doped MoSSe have sufficient thermodynamic driving forces for the photogenerated electrons and holes to be transferred from their surfaces to water [85] which makes the N, F co-doped MoSSe a suitable photocatalyst (Fig. 36 c, d) [85].

Ren et al. [132] reported the efficiency of GaN and AlN doping on MoSSe that has a band gap of 1.479 and 1.420 eV, respectively, has a VB position below the photo-oxidation potential level and has CB minima above the photo-reduction potential level. The charge distribution from the GaN and AlN layers is 0.107 e and 0.158 e, respectively, for the MoSSe layer. The Potential decrease across the MoSSe/GaN and MoSSe/AlN heterostructure interface is 7.03 and 2.23 eV, respectively, which create an electric field inside to prevent further the pairing up of electron-hole pairs produced during the catalysis, proving the addition of GaN and AlN can be beneficial for the improved and efficient application of MoSSe [132].

5.5.4. Solar cells

MoSSe has a direct bandgap, which means that it can absorb light and convert it into electrical energy very efficiently. This makes it an attractive material for use in solar cells. In addition, MoSSe has a high absorption coefficient, which means that it can absorb a large amount of sunlight even when it is very thin. It is also a stable material, which makes it a good candidate for use in long-lasting solar cells. Furthermore, MoSSe has a high charge carrier mobility, which means that the electrons and holes generated by the absorption of light can move quickly and efficiently through the material [133,134].

Tan et al. [38] reported the synthesis and performance of a thin film of single-layer $\text{Mo}_{2x}\text{Se}_{2(1-x)}$ nanosheets with about 66 % of metallic 1T phase was used as an electrocatalyst for triiodide reduction in I^-/I^3- redox electrolyte in a DSSC, which exhibited higher electrocatalytic activity than thin films of 2H-phase single-layer $\text{Mo}_{2x}\text{Se}_{2(1-x)}$ nanosheets and single-layer MoS₂ nanosheets with about 67 % of metallic 1T phase. The CE in a DSSC was an exfoliated single-layer $\text{Mo}_{2x}\text{Se}_{2(1-x)}$ nanosheet deposited on an FTO substrate, with the photoanode being an N719 dye-sensitized mesoporous TiO₂ electrode. Because of their increased electrocatalytic activity towards tri-iodide reduction, exfoliated $\text{Mo}_{2x}\text{Se}_{2(1-x)}$ and MoS₂ nanosheets with a high concentration of 1T phase demonstrated better photovoltaic performance than 2H ones after annealing. The better photovoltaic performance of exfoliated $\text{Mo}_{2x}\text{Se}_{2(1-x)}$ should be attributable to its increased electrocatalytic activity toward tri-iodide reduction when compared to annealed $\text{Mo}_{2x}\text{Se}_{2(1-x)}$. The performance of the as-prepared DSSC cell is summarised in Fig. 37 a-d and Table 8 [38].

Mohanta et al. [136] examined the physics of a combination of a boron pnictide (BP, BAs) monolayer with a MoSSe monolayer in a van der Waals heterostructure setup and explored their potential applications. The van der Waals heterostructures were reported to be robust and to create type-II p-n heterojunctions that split photogenerated electron-hole pairs. The BP monolayer functions well as a donor material for MoSSe in the van der Waals heterostructure, making it a promising option for use in excitonic solar cells with high power conversion efficiencies. Using the frequency-dependent dielectric function, $\epsilon(\omega)$, the optical absorption coefficients for each heterostructure were calculated. Individual monolayer absorbance spectra and BX/MoSSe heterostructure absorbance spectra demonstrated substantial absorbance in the visible light part of the solar spectrum, with optical absorption coefficients of around 105 cm^{-1} comparable to those of other substances [137]. The BX/MoSSe (X = P, As) heterostructure performed as a p-n junction, with MoSSe acting as an acceptor and BX acting as a donor. Using a formalism, the power conversion efficiencies (PCE) of the BX/MoSSe heterostructures were computed and found to be 22.97 % and 20.86 %, respectively, which is similar to previously reported PCEs. The high sun-to-electricity energy conversion efficiency achieved by mixing a Janus MoSSe monolayer with boron pnictide monolayers in this study

implies that this material might be beneficial in constructing enhanced excitonic solar cells. The PCE was estimated using a fill factor of 65 %, which accounts for a variety of parameters such as thermalisation, transmission, and recombination.

Liu et al. [138] calculated the optical absorption coefficients of the heterostructures and compared them to MoSSe and g-GeC monolayers. They found that MoSSe exhibits a higher visible-light absorption coefficient than g-GeC, and when stacked in a heterostructure, the absorption peaks of the MoSSe/g-GeC can still reach $6 \times 10^4 \text{ cm}^{-1}$ in the visible light region, suggesting a good response to visible and near UV lights. The researchers then calculated the power conversion efficiency (PCE) of the heterostructure as a solar cell device and found that it has a PCE of 7.6 %, which is comparable to other reported solar cell materials. Overall, the MoSSe/g-GeC heterostructure is considered a promising candidate for solar cells.

5.5.5. Other applications

5.5.5.1. N_2 fixation. Till now, we have discussed several applications of MoSSe. Due to the interesting properties of MoSSe, researchers have recently explored many other fields daily in order to verify the potential of MoSSe in those fields. We have discussed a few recently explored fields to provide our readers with an idea of those fields and ties.

First, we will discuss the application of MoSSe to nitrogen fixation. Given that nitrogen is necessary for the biosynthetic production of the fundamental building blocks of plants, animals, and other life forms, nitrogen fixation is one of the most alluring conversions in the entire world [65,139,140]. Fertilizers are frequently produced in factories using the Haber-Bosch process. It must be achieved at high reaction pressures (200–250 bar) and temperatures (400–500 °C), as well as with the aid of Fe or Ru catalysts [141,142]. Many resources have been put into finding the most practical catalytic systems for this transformation in order to overcome the inertness of N_2 molecules. To activate the N_2 molecule and convert it to ammonia at ambient temperatures, catalysts such as electrocatalysts [143–145] photocatalysts [146], and refined nitrogenases [147] can be employed. There are six protons/electrons involved in the electrocatalytic N_2 reduction reaction (NRR).



The excellent catalyst is known to have a low activation energy and a low adsorption energy for the intermediate species [148]. Tang et al. [76] recently explored the idea of using MoSSe for nitrogen fixation through DFT analysis with variable strain on the structure.

The D-band centre model has been used to explain how catalytic activity changes with strain. The early transition metals with less than half-filled d-band electrons cause weak bonding with the tensile strain, whereas compression strain strengthens the interactions, according to the D-band model [76]. Contrarily, compression strain downshifts the d-band centre for the late transition metals, weakening the interaction, while tensile strain upshifts the d-band centre for improved interaction with adsorbates. Tensile strain reduces the d-band length due to less wave function overlap, as shown in Fig. 38 a-c. The population of the d-band decreases for an early transition metal. The d-band downshifts to keep the charge distribution constant while preserving the d-band filling [76]. Instead, as the band narrows, the population of the late transition metal's d-band increases, and the d-band shifts upwards to preserve its degree of d-band filling. As a result, the interface between the Mo metal and adsorbates exhibits strong interfacial interaction when subjected to tensile strain. Using this theory, strain-induced MoSSe has been used by Tang et al. to adsorb N_2 on the catalyst surface, which is considered the most energy-requiring step for an N_2 fixation reaction. A steady decrease can be observed with % of N_2 coverage. Hence, this study provides us with the idea that d-band modulation can be used in future to tune the N_2 fixation possibilities, and the strain effect can be a useful parameter [76] (see Fig. 39).

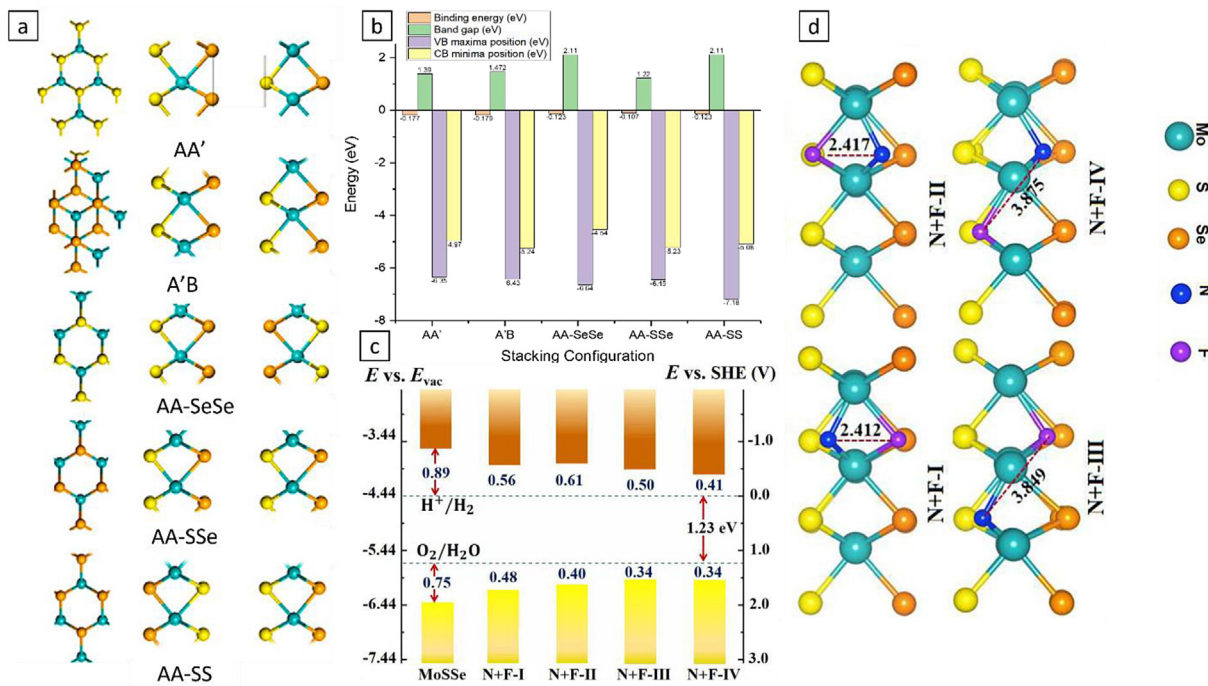


Fig. 36. (a) Different types of stacking possibilities in MoSSe [20]; (b) Various parameters for suitable photocatalytic behaviour in MoSSe stacking [20]; (c) The energy band diagram for suitable photocatalytic behaviour at the different possible doping configurations in N, F co-doped MoSSe [85]; (d) Different possible doping configuration in N, F co-doped MoSSe [85].

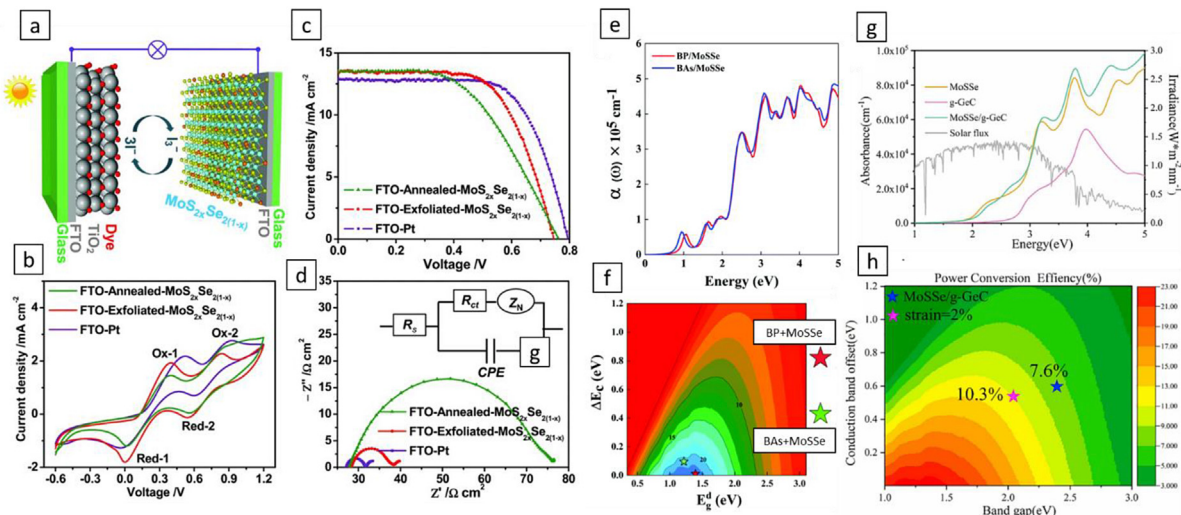


Fig. 37. (a) A schematic illustration of a typical DSSC [38]; (b) Measurement of cyclic voltammetry (CV) curves of different types of counter electrodes [38]; (c) Measurement of the current-voltage (J-V) curves of DSSCs with different types of counter electrodes [38]; (d) Measurement of Nyquist plots of symmetric dummy cells with two identical counter electrodes (FTO-exfoliated- $\text{MoS}_{2x}\text{Se}_{2(1-x)}$, FTO-Annealed- $\text{MoS}_{2x}\text{Se}_{2(1-x)}$, or FTO-Pt), and fitting equivalent circuit to the data [38]; (e) The absorption coefficient of BP/MoSSe and BAAs/MoSSe [136]; (f) PCE contour of BP/MoSSe and BAAs/MoSSe [136]; (g) The absorption coefficient MoSSe, g-GeC, MoSSe/g-GeC [138]; (h) PCE contour of MoSSe/g-GeC [138].

Li et al. [65] investigated several MoSSe nanosheets with embedded transition metals on S or Se vacancies for the application of N_2 fixation. According to their findings, the best catalytic performance is displayed by Mo-embedded MoSSe with S vacancy. The initial hydrogenation of adsorbed N_2 is the potential-limiting step, with a barrier of 0.49 eV (Fig. 38 d-e). The DOS analysis (Fig. 38 f) demonstrates that doping a single Mo atom introduces impurity energy levels at the Fermi level,

resulting in an increase in conductivity during the NRR process. The comparatively low ΔG of 0.58 eV of NH_3 desorption allows for fast removal of the products from the catalyst. The analysis of selectivity towards competitive HER reaction also revealed that Mo-doped MoSSe has considerably greater selectivity for nitrogen reduction reaction as compared to the strength of adsorption of a single H atom and an N_2 molecule on the active site, ensuring improved NRR selectivity. Li et al.

Table 8

The characteristics of the MoSSe hybrids used in solar cell.

System	V _{OC} (V)	I _{SC} (ma/cm ²)	FF (%)	PCE (%)	Rct (Ω/cm^2)	R _s (Ω/cm^2)	Ref
FTO-Pt	0.80	12.82	0.69	7	2.28	27.07	[38]
FTO-exfoliated MoS _{2-x} Se _{2(1-x)}	0.75	13.40	0.65	6.5	4.60	28.40	[38]
FTO-annealed MoS _{2-x} Se _{2(1-x)}	0.76	13.52	0.52	5.4	23.25	27.92	[38]
MoSSe–WSSe				17.90			[135]

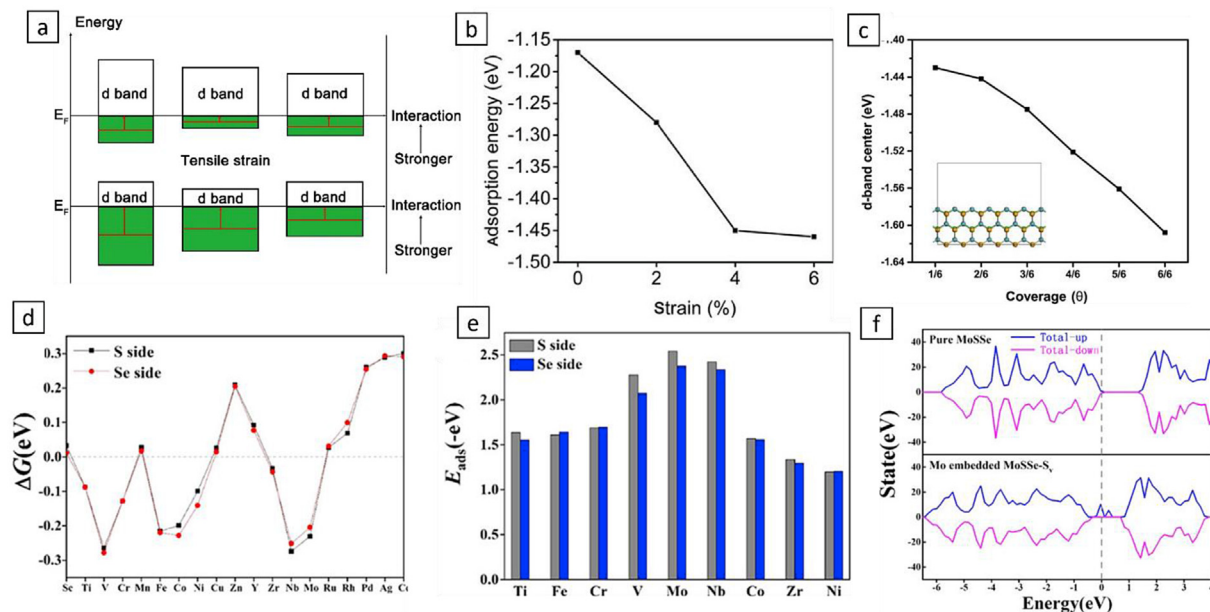


Fig. 38. (a) D band Model [76]; (b) Effect of strain on adsorption energy of N₂ adsorption on MoSSe [76]; (c) Effect of N₂ % coverage on d band centre [76]; (d) ΔG calculations for N₂ adsorption on S and Se vacancy of TM@MoSSe [65]; (e) Adsorption energy calculations for TM@MoSSe [65]; (f) DOS analysis of Mo dope MoSSe for the application of N₂ fixation [65].

[65] also verified the clustering possibility of Mo on MoSSe, as it is a pre-existing problem for single-atom catalysts [65]. According to calculations, a strong link between the metal atom and the catalyst effectively reduces the chance of metal polymerisation. Our DFT calculates the binding energies of the single-Mo-atom-embedded MoSSe with S and Se vacancies to be -3.74 and -3.73 eV, respectively. Because the binding energies are lower than the cohesive energy of Mo (6.82 eV/atom), the clustering of Mo atoms appears to be thermodynamically unavoidable [65].

A unique strategy of synthesising MoSSe was recently reported by Chen et al. [149] with extremely controllable pore size between 50 and 150 nm. This method involves presents a novel synthetic approach utilizing nanoporous gold (NPG) as a template for the scalable production of nanoporous metal compounds. This method involves the formation of few-atom-thick layers of surface alloys on NPG followed by exposure to vapour-phase precursors, resulting in the formation of large-scale nanoporous metal compounds. Through this process, the researchers synthesised various binary and alloyed compounds, including sulfides, selenides, tellurides, carbides, and nitrides. Specifically, they produced nanoporous MoSSe, demonstrating a 3D bicontinuous and interconnected structure with tunable pore sizes. Characterization techniques such as Raman spectroscopy and electron microscopy confirmed the structural integrity and composition of the synthesised compounds. Notably, the nanoporous MoSSe exhibited promising catalytic activity for nitrogen reduction, with a Faradaic efficiency of 7.51 % and a yield rate of 12.2 $\mu\text{g h}^{-1} \text{mg}^{-1}$ cat under ambient conditions. The study underscores the versatility and potential of the proposed synthetic protocol in fabricating diverse nanoporous metal compounds with tailored properties for various applications, including catalysis and energy storage.

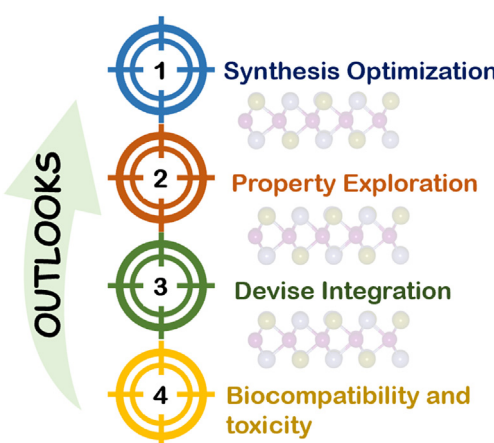


Fig. 39. Schematic representing the future perspective of 2D Janus MoSSe and MoSe_xS_(1-x) monolayers.

5.5.5.2. Z-scheme photocatalysis. Photocatalysts with a visible light absorption range, high catalytic efficiency, strong redox capability, and long-lasting durability are typically needed for commercial applications [150]. However, current single semiconductors or traditional type II heterostructures are unable to meet all of the aforementioned requirements because improving redox ability requires a wide band gap, which reduces light-harvesting range while improving photo-absorption

requires a narrow band gap, which invariably results in subpar redox ability [151,152]. To obtain high photocatalytic efficiency without the use of mediators, the interlayer electron-hole recombination rate in direct Z-scheme photocatalysts must be significantly larger than the intralayer electron-hole recombination rate. Two separate 2D surfaces can offer unique surfaces to the HER and OER reactions, increasing the efficiency of the present Z-scheme process [153]. This necessitates a significantly lower interlayer band gap than an intralayer band gap. Furthermore, in order for the heterostructure to completely realise water splitting, the CB minima (lower VB maxima) of the semiconductor 2 (semiconductor 1) layer must be more positive (negative) than the reduction (oxidation) potential of H⁺/H₂ (O₂/H₂O). As a solution to this problem, Z-scheme photocatalytic devices with two-step photoexcitation have been developed, inspired by natural photosynthesis. Since photo-generated electrons (holes) tend to stay at the semiconductor layer with a higher CB minima (lower VB maxima) energy level, Z-scheme photocatalysts have better redox abilities than conventional semiconductor photocatalysts. This enables a broader spectrum of solar light collecting. As a result, the photocatalytic effectiveness is considerably enhanced [154,155].

The three general categories for Z-scheme photocatalysts are all-solid-state Z-scheme photocatalysts with electron conductors, direct Z-scheme photocatalysts without any charge carrier transfer mediator, and traditional Z-scheme photocatalysts with redox ion pairs, depending on whether the carrier transfer mediator is introduced or not [156,157]. Direct Z-scheme photocatalysts, in particular, are capable of reducing the backward reactions and light shielding effect caused by charge carrier mediators. Additionally, because the majority of redox mediators are unstable and frequently deactivate in solution, most direct Z-scheme photocatalysts have exceptional corrosion resistance [158,159]. Direct Z-scheme photocatalysts are exceptionally promising for photocatalytic water splitting because of these unique characteristics.

Yet, logically designing direct Z-scheme photocatalysts remains exceedingly challenging. The challenge is to use theory and experiment to directly characterise direct Z-scheme photocatalysts. The charge transfer route may be used to qualitatively evaluate whether the heterostructure is a straight Z-scheme or type II configuration based on calculations using density functional theory (DFT). Charge transport, in particular, exhibits Z-scheme behaviour when the built-in electric field inhibits charge separation and favours interlayer electron-hole (e-h) recombination [160–163]. Otherwise, the standard type II mode should be employed. According to current study, the built-in electric field technique and charge transfer dynamics such as e-h recombination and charge separation in heterostructures should both be considered when building direct Z-scheme photocatalysts [160–163].

As we already know about the existing in-built electric field of MoSSe, several researchers tried to discover the possibilities of the application of MoSSe type Janus materials as one of the 2D surface of 2 required surfaces for the modified Z-scheme catalytic activities. As a potential Z-scheme catalysts, Zhou et al. [164] reported MoSSe/WSeTe; Bao et al. [165] reported Sc₂CF₂/MoSSe; Singh et al. [166] reported MoSSe/HfS₂, MoSSe/TiS₂, MoS₂/T-SnO₂, MoSSe/T-SnO₂ and MoSSe/ZrS₂.

6. Conclusion and outlooks

The review presents a thorough examination of Janus-MoSSe and MoSe_xS_(1-x) alloy materials, highlighting their unique properties and potential applications in nanotechnology. However, a closer look reveals several critical issues that call into question the widespread adoption and optimization of these materials.

Firstly, the scalability of the synthesis process is a significant obstacle. While techniques such as chemical vapour deposition (CVD) have proven successful in producing high-quality 2D materials, they often suffer from time and cost issues that hinder large-scale production. Alternative methods such as solution-based approaches need to be explored to overcome this limitation and enable cost-effective mass production.

In addition, the stability of Janus-MoSSe and MoSe_xS_(1-x) alloys under various environmental conditions is of great concern. Their susceptibility to degradation at high temperatures and high humidity jeopardizes their reliability and long-term performance in practical applications. Efforts to improve material stability through modified synthesis parameters or novel processing techniques are essential to overcome this challenge.

The limited understanding of the fundamental properties of MoSSe materials raises doubts about their optimization for specific applications. Critical aspects such as the band structure and charge carrier dynamics are still insufficiently researched, which makes it difficult to precisely adapt these materials to the desired functions. Concerted experimental and theoretical investigations are needed to close these knowledge gaps.

Integration with other materials and devices is also proving to be a formidable obstacle. To achieve an effective connection between MoSSe materials and different substrates or devices, compatibility problems must be overcome and innovative integration strategies developed. This challenge requires interdisciplinary collaboration and innovative approaches to material synthesis and device fabrication.

Concerns about the toxicity of MoSSe materials, especially in biomedical applications, also require urgent attention. Comprehensive toxicity studies and the development of safe handling protocols are essential to minimize potential risks associated with their use. Understanding the biocompatibility and environmental impact of these materials is crucial for their responsible use in various fields.

In summary, while Janus-MoSSe and MoSe_xS_(1-x) alloys show great promise for various applications, their widespread use faces significant hurdles. Scalability, stability, understanding of fundamental properties, integration challenges and toxicity concerns require concerted efforts and innovative research efforts. Overcoming these obstacles is crucial to unlock the full potential of these materials and drive innovation in various fields.

Declaration of competing interest

The authors declare that they have no known competing financial interests or personal relationships that could have appeared to influence the work reported in this paper.

Acknowledgment

The authors gratefully acknowledge financial assistance from the SERB Core Research Grant (Grant No. CRG/2022/000897), Department of Science and Technology (DST/NM/NT/2019/205(G)), and Minor Research Project Grant, Jain University (JU/MRP/CNMS/29/2023). CSR acknowledges National Research Foundation of Korea for the Brain Pool program funded by the Ministry of Science and ICT, South Korea (Grant No. RS-2023-00222186).

Appendix A. Supplementary data

Supplementary data to this article can be found online at <https://doi.org/10.1016/j.apmate.2024.100204>.

References

- [1] Z. Lei, J. Zhan, L. Tang, Y. Zhang, Y. Wang, Recent development of metallic (1T) phase of molybdenum disulfide for energy conversion and storage, *Adv. Energy Mater.* 8 (2018) 1703482.
- [2] S. Balendran, J. Deng, J.Z. Ou, S. Walia, J. Scott, J. Tang, K.L. Wang, M.R. Field, S. Russo, S. Zhuiykov, M.S. Strano, N. Medhekar, S. Sriram, M. Bhaskaran, K. Kalantar-zadeh, Enhanced charge carrier mobility in two-dimensional high dielectric molybdenum oxide, *Adv. Mater.* 25 (2013) 109–114.
- [3] P. Shinde, C.S. Rout, Advances in synthesis, properties and emerging applications of tin sulfides and its heterostructures, *Mater. Chem. Front.* 5 (2021) 516–556.
- [4] R. Samal, C.S. Rout, Recent developments on emerging properties, growth approaches, and advanced applications of metallic 2D layered vanadium dichalcogenides, *Adv. Mater. Interfac.* 7 (2020) 1901682.

- [5] H. Li, X. Zhou, W. Zhai, S. Lu, J. Liang, Z. He, H. Long, T. Xiong, H. Sun, Q. He, Z. Fan, H. Phase engineering of nanomaterials for clean energy and catalytic applications, *Adv. Energy Mater.* 10 (2020) 2002019.
- [6] Y. Li, H. Yan, B. Xu, L. Zhen, C.Y. Xu, Electrochemical intercalation in atomically thin van der Waals materials for structural phase transition and device applications, *Adv. Mater.* 33 (2021) 2000581.
- [7] Y. Cheng, H. Song, H. Wu, P. Zhang, Z. Tang, S. Lu, Defects enhance the electrocatalytic hydrogen evolution properties of MoS₂-based materials, *Chem. Asian J.* 15 (2020) 3123–3134.
- [8] Q. Li, Y.C. Wang, J. Zeng, X. Zhao, C. Chen, Q.M. Wu, L.M. Chen, Z.Y. Chen, Y.P. Lei, Bimetallic chalcogenides for electrocatalytic CO₂ reduction, *Rare Met.* 40 (2021) 3442–3453.
- [9] H. Li, X. Duan, X. Wu, X. Zhuang, H. Zhou, Q. Zhang, X. Zhu, W. Hu, P. Ren, P. Guo, L. Ma, X. Fan, X. Wang, J. Xu, A. Pan, X. Duan, Growth of alloy MoS₂xSe_{2(1-x)} nanosheets with fully tunable chemical compositions and optical properties, *JJ. Am. Chem. Soc.* 136 (2014) 3756–3759.
- [10] Y. Gong, Z. Liu, A.R. Lupini, G. Shi, J. Lin, S. Najmaei, Z. Lin, A. Laura Elías, A. Berkdemir, G. You, H. Terrones, M. Terrones, R. Vajtai, S.T. Pantelides, S.J. Pennycook, J. Lou, W. Zhou, P.M. Ajayan, Band gap engineering and layer-by-layer mapping of selenium-doped molybdenum disulfide, *Nano Lett.* 14 (2014) 442–449.
- [11] D.B. Trivedi, G. Turgut, Y. Qin, M.Y. Sayyad, D. Hajra, M. Howell, L. Liu, S. Yang, N.H. Patoary, H. Li, M.M. Petrić, M. Meyer, M. Kremser, M. Barbone, G. Soavi, A.V. Stier, K. Müller, S. Yang, I.S. Esqueda, H. Zhuang, J.J. Finley, S. Tongay, Room-temperature synthesis of 2D Janus crystals and their heterostructures, *Adv. Mater.* 32 (2020) 2006320.
- [12] A.Y. Lu, H. Zhu, J. Xiao, C.P. Chuu, Y. Han, M.H. Chiu, C.C. Cheng, C.W. Yang, K.H. Wei, Y. Yang, Y. Wang, D. Sokaras, D. Nordlund, P. Yang, D.A. Muller, M.Y. Chou, X. Zhang, L.J. Li, Janus monolayers of transition metal dichalcogenides, *Nat. Nanotechnol.* 12 (2017) 744–749.
- [13] J. Liang, W. Wang, H. Du, A. Hallal, K. Garcia, M. Chshiev, A. Fert, H. Yang, Very large Dzyaloshinskii-Moriya interaction in two-dimensional Janus manganese dichalcogenides and its application to realize skyrmion states, *Phys. Rev. B* 101 (2020) 184401.
- [14] C. Zhang, Y. Nie, S. Sanvito, A. Du, First-principles prediction of a room-temperature ferromagnetic Janus WS₂ monolayer with piezoelectricity, ferroelasticity, and large valley polarization, *Nano Lett.* 19 (2019) 1366–1370.
- [15] J. Yuan, Y. Yang, Y. Cai, Y. Wu, Y. Chen, X. Yan, L. Shen, Intrinsic skyrmions in monolayer Janus magnets, *Phys. Rev. B* 101 (2020) 94420.
- [16] A. Kandemir, H. Sahin, Bilayers of Janus WS₂: monitoring the stacking type via the vibrational spectrum, *Phys. Chem. Chem. Phys.* 20 (2018) 17380–17386.
- [17] R. Chaurasiya, G.K. Gupta, A. Dixit, Heterostructure AZO/WSe₂/WS(Se)₂ as an efficient single junction solar cell with ultrathin Janus WSe₂ buffer layer, *J. Phys. Chem. C* 125 (2021) 4355–4362.
- [18] J. Zhang, S. Jia, I. Kholmanov, L. Dong, D. Er, W. Chen, H. Guo, Z. Jin, V.B. Shenoy, L. Shi, J. Lou, Janus monolayer transition-metal dichalcogenides, *ACS Nano* 11 (2017) 8192–8198.
- [19] A. Bera, A. Singh, Y.A. Sorb, R.N. Jenjeti, D.V.S. Muthu, S. Sampath, C. Narayana, U. V Waghray, A.K. Sood, Chemical ordering and pressure-induced isostructural and electronic transitions in MoS₂ crystal, *Phys. Rev. B* 102 (2020) 14103.
- [20] Z. Guan, S. Ni, S. Hu, Tunable electronic and optical properties of monolayer and multilayer Janus MoS₂ as a photocatalyst for solar water splitting: a first-principles study, *JPC C* 122 (2018) 6209–6216.
- [21] S. Tongay, D.S. Narang, J. Kang, W. Fan, C. Ko, A. V Luce, K.X. Wang, J. Suh, K.D. Patel, V.M. Pathak, J. Li, J. Wu, Two-dimensional semiconductor alloys: monolayer Mo_{1-x}W_xSe₂, *Appl. Phys. Lett.* 104 (2014) 12101.
- [22] V. Kiran, D. Mukherjee, R.N. Jenjeti, S. Sampath, Active guests in the MoS₂/MoSe₂ host lattice: efficient hydrogen evolution using few-layer alloys of MoS_{2(1-x)}Se_{2x}, *Nanoscale* 6 (2014) 12856–12863.
- [23] Mamta, Y. Singh, K.K. Maurya, V.N. Singh, Transition metal dichalcogenide MXY (M = Mo, W; X, Y = S, Se) monolayer: structure, fabrication, properties, and applications, *JMR (J. Mol. Recognit.)* 37 (2022) 3403–3417.
- [24] Y. Qin, M. Sayyad, A.R.P. Montblanch, M.S.G. Feuer, D. Dey, M. Blei, R. Sailus, D.M. Kara, Y. Shen, S. Yang, A.S. Botana, M. Atature, S. Tongay, Reaching the excitonic limit in 2D Janus monolayers by in-situ deterministic growth, *Adv. Mater.* 34 (2022) 2106222.
- [25] Q. Ma, M. Isararraga, C.S. Wang, E. Preciado, V. Klee, S. Bobek, K. Yamaguchi, E. Li, P. Michael Odenthal, A. Nguyen, D. Barroso, D. Sun, G. von Son Palacio, M. Gomez, A. Nguyen, D. Le, G. Pawin, J. Mann, T.F. Heinz, T. Shahnaz Rahman, L. Bartels, Postgrowth tuning of the bandgap of single-layer molybdenum disulfide films by sulfur/selenium exchange, *ACS Nano* 8 (2014) 4672–4677.
- [26] L. Yang, Q. Fu, W. Wang, J. Huang, J. Huang, J. Zhang, B. Xiang, Large-area synthesis of monolayered MoS_{2(1-x)}Se_{2x} with a tunable band gap and its enhanced electrochemical catalytic activity, *Nanoscale* 7 (2015) 10490–10497.
- [27] Q. Wang, Y. Lei, Y. Wang, Y. Liu, C. Song, J. Zeng, Y. Song, X. Duan, D. Wang, Y. Li, Atomic-scale engineering of chemical-vapor-deposition-grown 2D transition metal dichalcogenides for electrocatalysis, *Energy Environ. Sci.* 13 (2020) 1593–1616.
- [28] C.W. Jang, W.J. Lee, J.K. Kim, S.M. Park, S. Kim, S.H. Choi, Growth of two-dimensional Janus MoS₂ by a single in situ process without initial or follow-up treatments, *NPG Asia Mater.* 14 (2022).
- [29] P. Albert L. Sino, T.C. Lin, S. Wani, L. Lee, C.T. Chen, M.J. Liu, Y.Z. Kuo, B. Rehman, K. Tuyen Le, J.M. Wu, F.C. Chuang, Y.L. Chueh, Controllable structure-engineered Janus and alloy polymorphic monolayer transition metal dichalcogenides by plasma-assisted selenization process toward high-yield and wafer-scale production, *Mater. Today* 69 (2023) 97–106.
- [30] J. Meng, T. Wang, Z. He, Q. Li, H. Zhu, L. Ji, L. Chen, Q. Sun, D.W. Zhang, A high-speed 2D optoelectronic in-memory computing device with 6-bit storage and pattern recognition capabilities, *Nano Res.* 15 (2022) 2472–2478.
- [31] C. Bian, J. Shi, X. Liu, Y. Yang, H. Yang, G. Gao, Optical second-harmonic generation of Janus MoS₂ monolayer, *Chin. Phys. B* 31 (2022) 97304.
- [32] W. Zhang, X. Li, T. Jiang, J. Song, Y. Lin, L. Zhu, X. Xu, CVD synthesis of Mo_(1-x)W_xS₂ and MoS_{2(1-x)}Se_{2x} alloy monolayers aimed at tuning the bandgap of molybdenum disulfide, *Nanoscale* 7 (2015) 13554–13560.
- [33] S. Umrao, J. Jeon, S.M. Jeon, Y.J. Choi, S. Lee, A homogeneous atomic layer MoS_{2(1-x)}Se_{2x} alloy prepared by low-pressure chemical vapor deposition, and its properties, *Nanoscale* 9 (2017) 594–603.
- [34] Y.R. Lin, W.H. Cheng, M.H. Richter, J.S. DuChene, E.A. Peterson, C.M. Went, Z.Y. Al Bushi, D. Jariwala, J.B. Neaton, L.C. Chen, H.A. Atwater, Band edge tailoring in few-layer two-dimensional molybdenum sulfide/selenide alloys, *JPC C* 124 (2020) 22893–22902.
- [35] Q. Feng, Y. Zhu, J. Hong, M. Zhang, W. Duan, N. Mao, J. Wu, H. Xu, F. Dong, F. Lin, C. Jin, C. Wang, J. Zhang, L. Xie, Growth of large-area 2D MoS_{2(1-x)}Se_{2x} semiconductor alloys, *Adv. Math.* 26 (2014) 2648–2653.
- [36] Q. Feng, N. Mao, J. Wu, H. Xu, C. Wang, J. Zhang, L. Xie, Growth of MoS_{2(1-x)}Se_{2x} ($\chi = 0.41\text{--}1.00$) monolayer alloys with controlled morphology by physical vapor Deposition, *ACS Nano* 9 (2015) 7450–7455.
- [37] S. Mukherjee, D. Bhattacharya, S.K. Ray, A.N. Pal, High-performance broad-band photodetection based on graphene–MoS₂Se_{2(1-x)} alloy engineered phototransistors, *ACS Appl. Mater. Interfaces* 14 (2022) 34875–34883.
- [38] C. Tan, W. Zhao, A. Chaturvedi, Z. Fei, Z. Zeng, J. Chen, Y. Huang, P. Ercius, Z. Luo, X. Qi, B. Chen, Z. Lai, B. Li, X. Zhang, J. Yang, Y. Zong, C. Jin, H. Zheng, C. Kloc, H. Zhang, Preparation of single-layer MoS₂Se_{2(1-x)} and Mo_xW_{1-x}S₂ nanosheets with high-concentration metallic 1T Phase, *Small* 12 (2016) 1866–1874.
- [39] L. Zhang, Y. Xia, X. Li, L. Li, X. Fu, J. Cheng, R. Pan, Janus two-dimensional transition metal dichalcogenides, *J. Appl. Phys.* 131 (2022) 230902.
- [40] A. Singh, S. Soon Jo, Y. Li, C. Wu, M. Li, R. Jaramillo, Refractive uses of layered and two-dimensional materials for integrated photonics, *ACS Photonics* 7 (2020) 3270–3285.
- [41] Z. Gan, I. Paradiso, A. Estrada-Real, J. Picker, E. Najafidehaghani, F. Davies, C. Neumann, C. Robert, P. Wiecha, K. Watanabe, T. Taniguchi, X. Marie, J. Biskupek, M. Mundszinger, R. Leiter, U. Kaiser, A. V Krasheninnikov, B. Urbaszek, A. George, A. Turchanin, Chemical vapor deposition of high-optical-quality large-area monolayer Janus transition metal dichalcogenides, *Adv. Math.* 34 (2022) 2205226.
- [42] S.B. Harris, Y.C. Lin, A.A. Puretzky, L. Liang, O. Dyck, T. Berlijn, G. Eres, C.M. Rouleau, K. Xiao, D.B. Geoghegan, Real-time diagnostics of 2D crystal transformations by pulsed laser deposition: controlled synthesis of Janus WS₂ monolayers and alloys, *ACS Nano* 17 (2023) 2472–2486.
- [43] M. Yagmurcukardes, Y. Qin, S. Ozen, M. Sayyad, F.M. Peeters, S. Tongay, H. Sahin, Quantum properties and applications of 2D Janus crystals and their superlattices, *Appl. Phys. Rev.* 7 (2020) 11311.
- [44] T. Hu, F. Jia, G.D. Zhao, J. Wu, A. Stroppa, W. Ren, Intrinsic and anisotropic Rashba spin splitting in Janus transition-metal dichalcogenide monolayers, *Phys. Rev. B* 97 (2018).
- [45] W. Shi, Z. Wang, Mechanical and electronic properties of Janus monolayer transition metal dichalcogenides, *J. Condens. Matter Phys.* 30 (2018).
- [46] W.J. Yin, Y. Liu, B. Wen, X.B. Li, Y.F. Chai, X.L. Wei, S. Ma, G. Teobaldi, The unique carrier mobility of monolayer Janus MoS₂ nanoribbons: a first-principles study, *Dalton Trans.* 50 (2021) 10252–10260.
- [47] H.S. Waheed, M. Asghar, H.S. Ahmad, H. Abbas, H. Ullah, R. Ali, M.J.I. Khan, M.W. Iqbal, Y.H. Shin, M.S. Khan, R. Neffati, Janus MoSO and MoS₂ monolayers: a promising material for solar cells and photocatalytic applications, *Phys. Status Solidi B* 260 (2023) 2200267.
- [48] L.D. Pan, L.Z. Zhang, B.Q. Song, S.X. Du, H.J. Gao, Graphyne- and graphdiyne-based nanoribbons: density functional theory calculations of electronic structures, *Appl. Phys. Lett.* 98 (2011) 173102.
- [49] W.J. Yin, H.J. Tan, P.J. Ding, B. Wen, X.B. Li, G. Teobaldi, L.M. Liu, Recent advances in low-dimensional Janus materials: theoretical and simulation perspectives, *Mater. Adv.* 2 (2021) 7543–7558.
- [50] Z. Wang, 2H → 1T' phase transformation in Janus monolayer MoS₂ and MoS₂: an efficient hole injection contact for 2H-MoS₂, *J. Mater. Chem. C* 6 (2018) 13000–13005.
- [51] Y. Wei, X. Xu, S. Wang, W. Li, Y. Jiang, Second harmonic generation in Janus MoS₂ a monolayer and stacked bulk with vertical asymmetry, *Phys. Chem. Chem. Phys.* 21 (2019) 21022–21029.
- [52] X. Zhang, R. Pang, X. Hou, S. Wang, Stacking-tailoring quasiparticle energies and interlayer excitons in bilayer Janus MoS₂, *New J. Phys.* 23 (2021) 013003.
- [53] C.Y. Wang, G.Y. Guo, Nonlinear optical properties of transition-metal dichalcogenide MX₂ (M = Mo, W; X = S, Se) monolayers and trilayers from first-principles calculations, *J. Phys. Chem. C* 119 (2015) 13268–13276.
- [54] C. Versara, J.E. Sipe, Nonlinear optical susceptibilities of semiconductors: results with a length-gauge analysis, *Phys. Rev. B* 52 (1995) 14636–14645.
- [55] G. Wang, C. Robert, M.M. Glazov, F. Cadiz, E. Courtade, T. Amand, D. Lagarde, T. Taniguchi, K. Watanabe, B. Urbaszek, X. Marie, In-plane propagation of light in

- transition metal dichalcogenide monolayers: optical selection rules, *Phys. Rev. Lett.* **119** (2017) 47401.
- [56] F. Barakat, A. Laref, M.S. AlSalhi, S. Faraji, The impact of anion elements on the engineering of the electronic and optical characteristics of the two dimensional monolayer Janus MoSSe for nanoelectronic device applications, *Results Phys.* **18** (2020) 103284.
- [57] T.N. Do, C.V. Nguyen, L.V. Tan, M. Idrees, B. Amin, N.V. Hieu, N.T.X. Hoai, L.T. Hoa, N.N. Hieu, H.V. Phuc, Effects of La and Ce doping on electronic structure and optical properties of janus MoSSe monolayer, *Superlattice. Microst.* **151** (2021) 106841.
- [58] H.-P. Komsa, A. V Krasheninnikov, Two-dimensional transition metal dichalcogenide alloys: stability and electronic properties, *J. Phys. Chem. Lett.* **3** (2012) 3652–3656.
- [59] M.M. Petrić, M. Kremser, M. Barbone, Y. Qin, Y. Sayyad, Y. Shen, S. Tongay, J.J. Finley, A.R. Botello-Méndez, K. Müller, Raman spectrum of Janus transition metal dichalcogenide monolayers WSSe and MoSSe, *Phys. Rev. B* **103** (2021) 35414.
- [60] A.S. Oreshonkov, E. V Sukhanova, Z.I. Popov, Raman spectroscopy of Janus MoSSe monolayer polymorph modifications using density functional theory, *Materials* **15** (2022) 3988.
- [61] S.S. Guan, S.S. Ke, F.F. Yu, H.X. Deng, Y. Guo, H.F. Lü, Controlling magnetism of monolayer Janus MoSSe by embedding transition-metal atoms, *Appl. Surf. Sci.* **496** (2019) 143692.
- [62] J.W. Li, S.S. Ke, H.X. Deng, X. Sun, Y. Guo, H.F. Lü, Defect modulated electronic structure and magnetism in the 1T' phase of Janus MoSSe, *Chem. Phys.* **555** (2022) 111440.
- [63] W. Shi, G. Li, Z. Wang, Triggering catalytic active sites for hydrogen evolution reaction by intrinsic defects in Janus monolayer MoSSe, *J. Phys. Chem. C* **123** (2019) 12261–12267.
- [64] M. Wang, X. Wang, M. Zheng, X. Zhou, Improving catalytic activity of “Janus” MoSSe based on surface interface regulation, *Molecules* **27** (2022) 6038.
- [65] L. Li, B.B. Li, Q. Guo, B.B.B. Li, Heoretical screening of single-atom-embedded MoSSe nanosheets for electrocatalytic N₂ fixation, *J. Phys. Chem. C* **123** (2019) 123–14501.
- [66] X. Lai, Y. Zhang, Y. Zheng, X. Xiang, H. Ye, W. Liu, Low-dimensional systems and nanostructures catalytic activity for hydrogen evolution reaction in square phase Janus MoSSe monolayer : a first-principles study, *Phys. E: Low-Dimens. Nanostructures* **126** (2021) 114485.
- [67] A.R. Rezk, B. Carey, A.F. Chrimes, D.W.M. Lau, B.C. Gibson, C. Zheng, M.S. Fuhrer, L.Y. Yeo, K. Kalantar-zadeh, Acoustically-driven trion and exciton modulation in piezoelectric two-dimensional MoS₂, *Nano Lett.* **16** (2016) 849–855.
- [68] B. Rajbanshi, S. Sarkar, P. Sarkar, The electronic and optical properties of MoS_{2(1-x)}Se_{2x} and MoS_{2(1-x)}Te_{2x} monolayers, *Phys. Chem. Chem. Phys.* **17** (2015) 26166–26174.
- [69] J. Gusakova, V. Gusakov, B.K. Tay, DFT study of structural and electronic properties of MoS_{2(1-x)}Se_{2x} alloy (x = 0.25), *J. Appl. Phys.* **123** (2018) 161594.
- [70] C. Tan, Z. Luo, A. Chaturvedi, Y. Cai, Y. Du, Y. Gong, Y. Huang, Z. Lai, X. Zhang, L. Zheng, X. Qi, M.H. Goh, J. Wang, S. Han, X. Wu, L. Gu, C. Kloc, H. Zhang, Preparation of high-percentage 1T-phase transition metal dichalcogenide nanodots for electrochemical hydrogen evolution, *Adv. Mater.* **30** (9) (2018) 1705509.
- [71] J. Yuan, Y. Shan, T. Li, Electronic structure and hydrogen evolution reaction in Janus monolayer MoSSe regulated by strain engineering, *J. Phys. D* **53** (12) (2020) 125502.
- [72] C. Yu, Z. Wang, Strain engineering and electric field tunable electronic properties of Janus MoSSe/WX₂ (X = S, Se) van der Waals heterostructures, *Phys. Status Solidi B* **256** (2019) 1900261.
- [73] M. Farkous, M. El-Yadri, H. Erguig, L.M. Pérez, D. Laroze, C.V. Nguyen, N.T.T. Binh, N.N. Hieu, H.V. Phuc, M. Sadoqi, G. Long, E. Feddi, Anisotropy of effective masses induced by strain in Janus MoSSe and WSSe monolayers, *Phys. E: Low-Dimens. Syst. Nanostructures* **134** (2021) 114826.
- [74] C.H. Chang, X. Fan, S.H. Lin, J.L. Kuo, Orbital analysis of electronic structure and phonon dispersion in MoS₂, MoSe₂, WS₂, and WSe₂ monolayers under strain, *Phys. Rev. B* **88** (2013) 195420.
- [75] G.S. Khosa, R. Kumar, S. Gupta, Engineering the electronic structure and transport coefficients of Janus MoSSe monolayer by applying z-axial strain, *Mater. Today: Proc.* **45** (2021) 5597–5601.
- [76] X. Tang, Z. Wei, Q. Liu, J. Ma, Strain engineering the D-band center for Janus MoSSe edge: nitrogen fixation, *J. Energy Chem.* **33** (2019) 155–159.
- [77] S. Zhang, X. Wang, Y. Wang, H. Zhang, B. Huang, Y. Dai, W. Wei, Electronic properties of defective Janus MoSSe monolayer, *J. Phys. Chem. Lett.* **13** (2022) 4807–4814.
- [78] Y.N. Wen, M.G. Xia, S.L. Zhang, Bandgap engineering of Janus MoSSe monolayer implemented by Se vacancy, *Comput. Mater. Sci.* **152** (2018) 20–27.
- [79] Y. Xu, Y. Yao, W. Yin, J. Cao, M. Chen, X. Wei, Intrinsic defect engineered Janus MoSSe sheet as a promising photocatalyst for water splitting, *RSC Adv.* **10** (2020) 10816–10825.
- [80] C. Long, Y. Dai, H. Jin, Effect of point defects on electronic and excitonic properties in Janus-MoSSe monolayer, *Phys. Rev. B* **104** (2021) 125306.
- [81] Y.M. Zhao, P. Ren, X.Y. Ma, J.P. Lewis, Q.B. Yan, G. Su, Effects of vacancy and Ti doping in 2D Janus MoSSe on photocatalysis, *J. Phys. Chem. C* **125** (2021) 11939–11949.
- [82] J. Zeng, G. Liu, Y. Han, W. Luo, M. Wu, B. Xu, C. Ouyang, Effects of vacancy and Ti doping in 2D Janus MoSSe on photocatalysis, *J. Phys. Chem. C* **125** (2021) 11939–11949.
- [83] C. Kittel, *Introduction to Solid State Physics*, eighth ed., John Wiley & Sons, inc, 2021.
- [84] Z. Cui, N. Lyu, Y. Ding, K. Bai, Noncovalently functionalization of Janus MoSSe monolayer with organic molecules, *Phys. E: Low-Dimens. Syst. Nanostructures* **127** (2021) 114503.
- [85] F. Zhao, J. Li, Y. Chen, M. Zhang, H. Zhang, Photocatalytic activity of co-doped Janus monolayer MoSSe for solar water splitting: a computational investigation, *Appl. Surf. Sci.* **544** (2021) 148741.
- [86] Z. Cui, K. Bai, Y. Ding, X. Wang, E. Li, J. Zheng, S. Wang, Electronic and optical properties of janus MoSSe and ZnO vdWs heterostructures, *Superlattice. Microst.* **140** (2020) 106445.
- [87] D. Xu, B. Zhai, Q. Gao, T. Wang, J. Li, C. Xia, Interface-controlled band alignment transition and optical properties of Janus MoSSe/GaN vdW heterobilayers, *J. Phys. D Appl. Phys.* **53** (2020) 55104.
- [88] Q.K. Zhang, W.H. Zhao, Z.P. Zhou, L.M. Cao, W.J. Yin, X.L. Wei, Z.K. Tang, H. Zhang, 2D Janus MoSSe/MoGeSiN₄ vdW heterostructures for photovoltaic and photocatalysis applications, *J. Alloys Compd.* **938** (2023) 168708.
- [89] C. Jin, X. Tang, X. Tan, S.C. Smith, Y. Dai, L. Kou, A Janus MoSSe monolayer: a superior and strain-sensitive gas sensing material, *J. Mater. Chem. A* **7** (2019) 10999–1106.
- [90] A. Taufik, Y. Asakura, T. Hasegawa, S. Yin, MoS_{2-x}Se_x nanoparticles for NO detection at room temperature, *ACS Appl. Nano Mater.* **4** (2021) 6861–6871.
- [91] R. Chaurasiya, A. Dixit, Defect engineered MoSSe Janus monolayer as a promising two dimensional material for NO₂ and NO gas sensing, *Appl. Surf. Sci.* **490** (2019) 204–219.
- [92] H. Chen, J. Pang, J. Zhang, G. Wei, S. Wei, J. Yan, S. Jin, Exploring Janus MoSSe monolayer as a workable media for SOF₆ decompositions sensing based on DFT calculations, *Comput. Mater. Sci.* **186** (2021) 109976.
- [93] X.Y. Yang, T. Hussain, J.P.A. Wärnå, Z. Xu, R. Ahuja, Exploring Janus MoSSe monolayer as a workable media for SOF₆ decompositions sensing based on DFT calculations, *Comput. Mater. Sci.* **186** (2021) 109976.
- [94] S. Jia, A. Bandyopadhyay, H. Kumar, J. Zhang, W. Wang, T. Zhai, V.B. Shenoy, J. Lou, Biomolecular sensing by surface-enhanced Raman scattering of monolayer Janus transition metal dichalcogenide, *Nanoscale* **12** (2020) 10723–10729.
- [95] J. Zhang, Y. Qian, H. Nan, X. Gu, Large-scale MoS_{2(1-x)}Se_{2x} monolayers synthesized by confined-space CVD, *Nanotechnology* **2** (2021) 355601.
- [96] V. Klee, E. Preciado, D. Barroso, A.E. Nguyen, C. Lee, K.J. Erickson, M. Triplett, B. Davis, I. Lu, S. Bobek, J. McKinley, J.P. Martinez, J. Mann, A.A. Talin, L. Bartels, Superlinear composition-dependent photocurrent in CVD-grown monolayer MoS_{2(1-x)}Se_{2x} Alloy Devices, *Nano Lett.* **2** (2015) 2612–2619.
- [97] K. Hou, Z. Huang, S. Liu, G. Liao, H. Qiao, A hydrothermally synthesized MoS_{2(1-x)}Se_{2x} alloy with deep-shallow level conversion for enhanced performance of photodetectors Kaiqiang, *Nanoscale Adv.* **2** (2020) 2185–2191.
- [98] H. Xu, J. Zhu, G. Zou, W. Liu, X. Li, C. Li, Spatially bandgap - graded M homojunctions for self - powered visible - near - infrared phototransistors, *Nano-Micro Lett.* **12** (2020) 1–14.
- [99] S.Z. Butler, S.M. Hollen, L. Cao, Y. Cui, J.A. Gupta, H.R. Gutierrez, T.F. Heinz, S. Sae Hong, J. Huang, A.F. Ismach, E. Johnston-Halperin, M. Kuno, V. V. Plashnitsa, R.D. Robinson, R.S. Ruoff, S. Salahuddin, J. Shan, L. Shi, O.G. Michael Spencer, M. Terrones, W. Windl, J.E. Goldberger, Progress, challenges, and opportunities in two-dimensional materials beyond graphene, *ACS Nano* **7** (4) (2013) 2898–2926.
- [100] Q.H. Wang, K. Kalantar-Zadeh, A. Kis, J.N. Coleman, M.S. Strano, Electronics and optoelectronics of two-dimensional transition metal dichalcogenides, *Nat. Nanotechnol.* **7** (11) (2012) 6999–712.
- [101] M. Xu, T. Liang, M. Shi, H. Chen, Graphene-like two-dimensional materials, *Chem. Rev.* **113** (5) (2013) 3766–3798.
- [102] T. Yanase, F. Uehara, I. Naito, T. Nagahama, T. Shimada, Healing sulfur vacancies in monolayer MoS₂ by high-pressure sulfur and selenium annealing: implication for high-performance transistors, *ACS Appl. Nano Mater.* **3** (2020) 10462–10469.
- [103] A. Sellam, R.N. Jenjeti, S. Sampath, Ultrahigh-rate supercapacitors based on 2-dimensional, 1T MoS₂Se_{2(1-x)} for AC line-filtering applications, *J. Phys. Chem. C* **122** (2018) 14186–14194.
- [104] C. Shang, X. Lei, B. Hou, M. Wu, B. Xu, G. Liu, C. Ouyang, Heoretical prediction of Janus MoSSe as a potential anode material for lithium-ion batteries, *J. Phys. Chem. C* **122** (2018) 23899–23909.
- [105] H. Wang, Q. Chen, H. Li, Q. Duan, D. Jiang, J. Hou, Two-dimensional Janus MoSSe as a potential anode material for Na/K-ion batteries : a theoretical study, *Chem. Phys. Lett.* **735** (2019) 136777.
- [106] H. Lin, N. Lou, D. Yang, R. Jin, Y. Huang, Janus MoSSe/graphene heterostructures: potential anodes for lithium-ion batteries, *J. Alloys Compd.* **854** (2021) 157215.
- [107] J. He, J. Chen, S. Ma, Z. Jiao, Janus MoSSe/C₃N heterostructures: a flexible anode for lithium/sodium-ion batteries, *Phys. E: Low-Dimens. Syst. Nanostructures* **144** (2022) 115402.
- [108] F. Ersan, G. Gökolcu, E. Aktürk, Adsorption and diffusion of lithium on monolayer transition metal dichalcogenides (MoS_{2(1-x)}Se_{2x}) alloys, *J. Phys. Chem. C* **119** (2015) 28648–28653.
- [109] Y. Zhang, H. Tao, S. Du, X. Yang, Conversion of MoS₂ to a ternary MoS_{2-x}Se_x alloy for high-performance sodium-ion batteries, *ACS Appl. Mater. Interfaces* **11** (2019) 11327–11337.

- [110] H. He, D. Huang, Q. Gan, J. Hao, S. Liu, Z. Wu, W.K. Pang, B. Johannessen, Y. Tang, J.L. Luo, H. Wang, Z. Guo, Anion vacancies regulating endows MoSSe with fast and stable potassium ion storage, *ACS Nano* 13 (2019) 11843–11852.
- [111] J. Yang, H.S. Shin, Recent advances in layered transition metal dichalcogenides for hydrogen evolution reaction, *J. Mater. Chem. A* 2 (17) (2013) 5974–5985.
- [112] C.G. Morales-guio, L. Stern, X. Hu, L. Stern, Nanostructured hydrotreating catalysts for electrochemical hydrogen evolution, *Chem. Soc. Rev.* 43 (2014) 6555–6569.
- [113] J. Bonde, P.G. Moses, T.F. Jaramillo, J.K. Nørskov, I. Chorkendorff, Hydrogen evolution on nano-particulate transition metal sulfides, *Faraday Discuss* 140 (2009) 219–231.
- [114] B. Hinnemann, P.G. Moses, J. Bonde, K.P. Jørgensen, J.H. Nielsen, S. Horch, I. Chorkendorff, J.K. Nørskov, Biomimetic hydrogen evolution: MoS₂ nanoparticles as catalyst for hydrogen evolution, *J. Am. Chem. Soc.* 127 (2005) 5308–5309.
- [115] H. Tang, K. Dou, C.C. Kaun, Q. Kuang, S. Yang, MoSe₂ nanosheets and their graphene hybrids: synthesis, characterization and hydrogen evolution reaction studies, *J. Mater. Chem. A* 2 (2014) 360–364.
- [116] Q. Gong, L. Cheng, C. Liu, M. Zhang, Q. Feng, H. Ye, M. Zeng, L. Xie, Z. Liu, Y. Li, Ultrathin MoS_{2(1-x)Se₂} alloy nanoflakes for electrocatalytic hydrogen evolution reaction, *ACS Catal.* 5 (4) (2015) 2213–2219.
- [117] J. Kibsgaard, Z. Chen, B.N. Reinecke, T.F. Jaramillo, Engineering the surface structure of MoS₂ to preferentially expose active edge sites for electrocatalysis, *Nat. Mater.* 11 (2012) 963–969.
- [118] J. Yang, Y. Liu, C. Shi, J. Zhu, X. Yang, S. Liu, L. Li, Z. Xu, C. Zhang, T. Liu, Carbon nanotube with vertical 2D molybdenum sulphoselenide nanosheet arrays for boosting electrocatalytic hydrogen evolution, *ACS Appl. Energy Mater.* 1 (2018) 7035–7045.
- [119] R. Wang, X. Li, T. Gao, T. Yao, S. Liu, X. Wang, Beyond 1T-phase synergistic electronic structure and defects engineering in 2H-MoS_{2x}Se_{2(1-x)} nanosheets for enhanced hydrogen evolution reaction and sodium storage, *ChemCatChem* 518055 (2019) 3200–3211.
- [120] Z. Lin, B. Lin, Z. Wang, S. Chen, C. Wang, M. Dong, Q. Gao, Q. Shao, T. Ding, H. Liu, S. Wu, Z. Guo, Facile preparation of 1T/2H-Mo(S_{1-x}Se_x)₂ nanoparticles for boosting hydrogen evolution reaction, *ChemCatChem* 11 (2019) 2217–2222.
- [121] C. Xiao, R. Sa, Z. Ma, Z. Cui, W. Du, High-throughput screening of transition metal single-atom catalyst anchored on Janus MoSSe basal plane for hydrogen evolution reaction, *Int. J. Hydrogen Energy* 46 (2020) 10337–10345.
- [122] J. Xie, J. Zhang, S. Li, F. Grote, X. Zhang, H. Zhang, R. Wang, Y. Lei, B. Pan, Y. Xie, Controllable disorder engineering in oxygen-incorporated MoS₂ ultrathin nanosheets for efficient hydrogen evolution, *J. Am. Chem. Soc.* 47 (2013) 17881–17888.
- [123] J. Qiao, F. Song, J. Hu, D. Huo, J. Yuan, Ultrathin MoSSe alloy nanosheets anchored on carbon nanotubes as advanced catalysts for hydrogen evolution, *Int. J. Hydrogen Energy* 44 (2019) 16110–16119.
- [124] Y.H. Li, P.F. Liu, L.F. Pan, H.F. Wang, Z.Z. Yang, L.R. Zheng, P. Hu, H.J. Zhao, L. Gu, H.G. Yang, Local atomic structure modulations activate metal oxide as electrocatalyst for hydrogen evolution in acidic water, *Nat. Commun.* 6 (2015) 8064.
- [125] D. V Esposito, S.T. Hunt, A.L. Stottlemyer, K.D. Dobson, B.E. McCandless, R.W. Birkmire, J.G. Chen, Low-cost hydrogen-evolution catalysts based on monolayer platinum on tungsten monocarbide substrates, *Angew. Chem. Int. Ed.* 49 (2010) 9859–9862.
- [126] X. Lei, C. Ouyang, K. Huang, A first-principles investigation of Janus MoSSe as a catalyst for photocatalytic water-splitting, *Appl. Surf. Sci.* 537 (2021) 147919.
- [127] S. Zhang, H. Jin, C. Long, T. Wang, R. Peng, B. Huang, Y. Dai, MoSSe nanotube: a promising photocatalyst with an extremely long carrier lifetime, *J. Mater. Chem. A* 7 (2019) 7885–7890.
- [128] X. Ma, X. Wu, H. Wang, Y. Wang, A Janus MoSSe monolayer: a potential wide solar-spectrum water-splitting photocatalyst with a low carrier recombination rate, *J. Mater. Chem. A* 6 (2018) 2295–2301.
- [129] H. Jin, T. Wang, Z.R. Gong, C. Long, Y. Dai, Prediction of an extremely long exciton lifetime in a Janus-MoTe monolayer, *Nanoscale* 10 (41) (2018) 19310–19315.
- [130] X. Ma, X. Yong, C.C. Jian, J. Zhang, Transition metal-functionalized Janus MoSSe monolayer: a magnetic and efficient single-atom photocatalyst for water-splitting Applications, *J. Phys. Chem. C* 123 (30) (2019) 18347–18354.
- [131] Y. Wang, S. Liu, X. Hao, J. Zhou, D. Song, D. Wang, L. Hou, F. Gao, Fluorine-and nitrogen-codoped MoS₂ with a catalytically active basal plane, *ACS Appl. Mater. Interfaces* 9 (2017) 21.
- [132] K. Ren, S. Wang, Y. Luo, J.P. Chou, J. Yu, W. Tang, M. Sun, High-efficiency photocatalyst for water splitting: a Janus MoSSe/XN (X = Ga, Al) van der Waals heterostructure, *J. Phys. D* 53 (2020) 185504.
- [133] T.J.S. Anand, S. Shariza, Z.M. Rosli, A. Shaaban, Sivarao, M.R. Said, K. Jusoff, S. Thiru, Optical and Mott-Schottky studies of ternary MoSSe thin films synthesized by electrochemical route, *World Appl. Sci. J.* 21 (2013) 60–67.
- [134] R.M. dos Santos, M.L. Pereira, L.F. Roncaratti, L.A. Ribeiro, Predicting the energetic stabilization of Janus-MoSSe/AlN heterostructures: a DFT study, *Chem. Phys. Lett.* 771 (2021) 138465.
- [135] M. Bikerouin, M. Balli, Janus transition-metal dichalcogenides heterostructures for highly efficient excitonic solar cells, *Appl. Surf. Sci.* 598 (2022) 153835.
- [136] M.K. Mohanta, A. De Sarkar, Interfacial hybridization of Janus MoSSe and BX (X = P, As) monolayers for ultrathin excitonic solar cells, nanopiezotronics and low-power memory devices, *Nanoscale* 12 (2020) 22645–22657.
- [137] K.D. Pham, T.D. Nguyen, H.V. Phuc, N.N. Hieu, H.D. Bui, B. Amin, C.V. Nguyen, Strain and electric field engineering of band alignment in InSe/Ca(OH)₂ heterostructure, *Chem. Phys. Lett.* 732 (2019) 136649.
- [138] Y.L. Liu, Y. Shi, C.L. Yang, Two-dimensional MoSSe/g-GeC van der waals heterostructure as promising multifunctional system for solar energy conversion, *Appl. Surf. Sci.* 545 (2021) 148952.
- [139] S.J. Ferguson, Nitrogen cycle enzymology, *Curr. Opin. Chem. Biol.* 2 (1998) 182–193.
- [140] J. Rittle, J.C. Peters, An Fe-N₂ Complex that generates hydrazine and ammonia via Fe=NNH₂: demonstrating a hybrid distal-to-alternating pathway for N₂ Reduction, *J. Am. Chem. Soc.* 138 (2016) 30.
- [141] I.A. Amar, R. Lan, C.T.G. Petit, S. Tao, Solid-state electrochemical synthesis of ammonia: a review, *J. Solid State Electrochem.* 15 (2011) 1845–1860.
- [142] S. Giddey, S.P.S. Badwal, A. Kulkarni, Review of electrochemical ammonia production technologies and materials, *Int. J. Hydrogen Energy* 38 (2013) 14576–14594.
- [143] J.S. Anderson, J. Rittle, J.C. Peters, Catalytic conversion of nitrogen to ammonia by an iron model complex, *Nature* 501 (2013) 84–87.
- [144] Y. Tanabe, Y. Nishibayashi, Developing more sustainable processes for ammonia synthesis, *Coord. Chem. Rev.* 257 (2013) 2551–2564.
- [145] J.S. Anderson, M.E. Moret, J.C. Peters, Conversion of Fe-NH₂ to Fe-N₂ with release of NH₃, *J. Am. Chem. Soc.* 135 (2) (2012) 534–537.
- [146] P. Huang, W. Liu, Z. He, C. Xiao, T. Yao, Y. Zou, C. Wang, Z. Qi, W. Tong, B. Pan, S. Wei, Y. Xie, Single atom accelerates ammonia photosynthesis, *Sci. China Chem.* 61 (2018) 1187–1196.
- [147] B.M. Hoffman, D.R. Dean, L.C. Seefeldt, Climbing nitrogenase: toward a mechanism of enzymatic nitrogen fixation, *Acc. Chem. Res.* 42 (5) (2009) 609–619.
- [148] X. Han, X. Tong, G. Wu, N. Yang, X.Y. Guo, Carbon fibers supported NiSe nanowire arrays as efficient and flexible electrocatalysts for the oxygen evolution reaction, *Carbon* 129 (2018) 245–251.
- [149] D. Chen, S. Ning, J. Lan, M. Peng, H. Duan, A. Pan, Y. Tan, General synthesis of nanoporous 2D metal compounds with 3D bicontinuous structure, *Adv. Mater.* 32 (2020) 1–8.
- [150] P. Zhou, J. Yu, M. Jaroniec, All-solid-state Z-scheme photocatalytic systems, *Adv. Mater.* 26 (29) (2014) 4920–4935.
- [151] Y.P. Yuan, L.W. Ruan, J. Barber, S. Chye, J. Loo, C. Xue, Hetero-nanostructured suspended photocatalysts for solar-to-fuel conversion, *Energy Environ. Sci.* 7 (12) (2014) 3934–3951.
- [152] X. Li, J. Yu, M. Jaroniec, Hierarchical photocatalysts, *Chem. Soc. Rev.* 45 (2016) 2603.
- [153] R. Kumar, D. Das, A.K. Singh, C₂N/WS₂ van der Waals type-II heterostructure as a promising water splitting photocatalyst, *J. Catal.* 359 (2018) 143–150.
- [154] Q. Yuan, D. Liu, N. Zhang, W. Ye, H. Ju, L. Shi, R. Long, J. Zhu, Y. Xiong, Q. Yuan, D. Liu, N. Zhang, L. Shi, J. Zhu, Y. Xiong, Noble-metal-free Janus-like structures by cation exchange for Z-scheme photocatalytic water splitting under broadband light irradiation, *Angew. Chem.* 129 (15) (2017) 4270–4274.
- [155] H. Li, Y. Zhou, W. Tu, J. Ye, Z. Zou, State-of-the-art progress in diverse heterostructured photocatalysts toward promoting photocatalytic performance, *Adv. Funct. Mater.* 25 (7) (2015) 998–1013.
- [156] K. Maeda, Z-Scheme wssater splitting using two different semiconductor photocatalysts, *ACS Catal.* 3 (7) (2010) 1486–1503.
- [157] Q. Xu, L. Zhang, J. Yu, S. Wageh, A.A. Al-Ghamdi, M. Jaroniec, Direct Z-scheme photocatalysts: principles, synthesis, and applications, *Mater. Today* 21 (2018) 1042–1063.
- [158] R. Abe, K. Shinmei, N. Koumura, K. Hara, B. Ohtani, Visible-light-induced water splitting based on two-step photoexcitation between dye-sensitized layered niobate and tungsten oxide photocatalysts in the presence of a triiodide/iodide shuttle redox mediator, *J. Am. Chem. Soc.* 135 (45) (2013) 16872–16884.
- [159] L. Wang, X. usheng Zheng, L. iang Chen, Y. Xiong, H. Xu, L. Wang, L. Chen, Y. Xiong, H. Xu, D. Zheng, Van der Waals heterostructures comprised of ultrathin polymer nanosheets for efficient Z-scheme overall water splitting, *Angew. Chem.* 57 (2018) 3454–3458.
- [160] Y. Chen, T. Shi, P. Liu, X. Ma, L. Shui, C. Shang, Z. Chen, X. Wang, K. Kempa, G. Zhou, Insights into the mechanism of the enhanced visible-light photocatalytic activity of black phosphorus/BiVO₄ heterostructure: a first-principles study, *J. Mater. Chem. A* 6 (39) (2018) 19167–19175.
- [161] M. Zhu, Z. Sun, M. Fujitsuka, T. Majima, Z. Sun, Z-scheme photocatalytic water splitting on a 2D heterostructure of black phosphorus/bismuth vanadate using visible light, *Angew. Chem.* 57 (8) (2018) 2160–2164.
- [162] J. Zhang, H. Hong, J. Zhang, H. Fu, P. You, J. Lischner, K. Liu, E. Kaxiras, S. Meng, New pathway for hot electron relaxation in two-dimensional heterostructures, *Nano Lett.* 18 (2018) 6063.
- [163] R. Long, O. V Prezhdo, Quantum coherence facilitates efficient charge separation at a MoS₂/MoSe₂ van der Waals junction, *Nano Lett.* 16 (2016) 1996–2003.
- [164] Z. Zhou, X. Niu, Y. Zhang, J. Wang, Janus MoSSe/WSe₂ heterostructures: a direct Z-scheme photocatalyst for hydrogen evolution, *J. Mater. Chem. A* 7 (38) (2019) 21835–21842.
- [165] J. Bao, B. Zhu, F. Zhang, X. Chen, H. Guo, J. Qiu, X. Liu, J. Yu, Sc₂CF₂/Janus MoSSe heterostructure: a potential Z-scheme photocatalyst with ultra-high solar-to-hydrogen efficiency, *Int. J. Hydrogen Energy* 46 (2021) 39830–39843.
- [166] A. Singh, M. Jain, S. Bhattacharya, MoS₂ and Janus (MoSSe) based 2D van der Waals heterostructures: emerging direct Z-scheme photocatalysts, *Nanoscale Adv.* 3 (10) (2021) 2837–2845.



Dr. Brahmananda Chakraborty is a scientist in the High Pressure & Synchrotron Radiation Physics Division of Bhabha Atomic Research Centre, Mumbai, and an Associate Professor at Homi Bhabha National Institute. His current research interest includes Density Functional Theory (DFT) & Molecular Dynamics (MD) simulations of materials for energy materials, bio-Sensors, reactor fuel, structural materials, nanomaterials, and the behaviour of materials under high pressure. Dr. Chakraborty got his Ph.D. from IIT Bombay for his research topic on 'Irradiation Effects and Hydrogen Storage on Carbon Nanotubes'. He did two years of Post-doctoral research at North Carolina State University, USA. He received the International Association of Advanced Material (IAAM) Scientist Medal in 2017. He has published more than 180 papers in reputed international journals. Based on single-year performance (2022), he was selected among the top 2 % of researchers by Elsevier. He has developed several software packages for material simulations using Molecular Dynamics and Reactor Simulations using Monte Carlo Techniques. He has very good experience of teaching while teaching Density Functional Theory at North Carolina State University, USA, and Computational Physics at Homi Bhabha National Institute, Mumbai. Dr. Chakraborty is also a regular reviewer in reputed international journals like the Journal of Physical Chemistry, CARBON, Physical Chemistry Chemical Physics, etc.



Prof. Chandra Sekhar Rout is a full Professor at the Centre for Nano & Material Sciences (CNMS), Jain University. Before joining CNMS, He was a DST Ramanujan Fellow at IIT Bhubaneswar, India (2013–2017). He received his B.Sc. (2001) and M.Sc. (2003) degrees from Utkal University and his Ph.D. from JNCASR, Bangalore (2008). He did his postdoctoral research at the National University of Singapore (2008–2009), Purdue University, USA (2010–2012), and UNIST, South Korea (2012–2013). He was awarded the prestigious Ramanujan Fellowship and Young Scientist award of the Department of Science and Technology, Govt. of India in 2013, the emerging investigator award 2017 from Elsevier, the IAAM medal 2017 from the International Association of Advanced Materials 2017, the Young researcher award from Venus International Foundation in 2015. His research interests include the preparation and characterization of 2D layered materials and their hybrids for chemical sensors and biosensors, supercapacitors and energy storage devices, field emitters, and electronic devices. He has authored more than 200 research papers in international journals and edited 3 books. His current h-index is 58 with total citations >14,000. He was ranked top 2 % of scientists in India by the Stanford study in 2020–2023.